Numerical modeling and simulation of cavitating flows in different regimes

A DISSERTATION
SUBMITTED TO THE FACULTY OF THE GRADUATE SCHOOL
OF THE UNIVERSITY OF MINNESOTA
BY

Filipe Leite Brandao

IN PARTIAL FULFILLMENT OF THE REQUIREMENTS
FOR THE DEGREE OF
DOCTOR OF PHILOSOPHY

Krishnan Mahesh, Adviser

March, 2023

Acknowledgements

First and foremost, I would like to thank God. He has given me strength and encouragement throughout all the challenging moments of completing this thesis. I would like to extend my deepest gratitude to my adviser Prof. Krishnan Mahesh for allowing me to work in his research group. His knowledge, experience, guidance, and motivation have been instrumental in aiding the completion of my research work. He is very approachable and always keen to discuss research progress. I admire his teaching and presentation skills. I have learned a lot by rehearsing conference presentations with him and through his feedback on scientific writings.

I would like to extend my gratitude to Prof. Ellen Longmire, Prof. Joseph Nichols, and Prof. Ilja Siepmann for being in my examination committee and reviewing my thesis. I also benefited greatly from the teachings of various faculty members through the coursework. The work in this dissertation was supported by the United States Office of Naval Research under Grant ONR N00014–17–1–2676 with Dr. Ki–Han Kim and Dr. Yin Lu Young as the program managers. The computations were made possible through the computing resources provided by the High–Performance Computing Modernization Program (HPCMP), Texas Advanced Computing Center (TACC), and the Minnesota Supercomputing Institute (MSI). I also acknowledge Dr. Karuna Agarwal and Prof. Joseph Katz at the Johns Hopkins University for providing the experimental data for the backward–facing step.

Many thanks to all my colleagues at the University of Minnesota. Special thanks to Dr. Thomas Kroll, Dr. Rong Ma and Mr. Aditya Madabhushi who started this journey alongside me. Special thanks to Dr. Mrugank Bhatt and Dr. Praveen Kumar

for mentoring me during the initial stages of my Ph.D. and answering innumerable silly questions. I have also benefited from my interactions with Dr. Karim Alame, Dr. Wyatt Horne, Mr. Ali Fakhreddine, Dr. Sreevatsa Anantharamu, and Mr. Nick Morse. I also extend the gratitute to my friend Dr. Eduardo Vitral who helped me adapt to the life in the USA, and particularly in Minnesota.

Finally, this work would not have been possible without the limitless love, support, and care of my parents Ricardo and Marcia. Thank you for encouraging me in all of my pursuits. Big thanks to my beloved wife Vilma, whose constant encouragement has gone a long way in helping me complete my thesis. I could not have asked for a more supportive wife, a better friend and a wiser partner.

To my parents, Ricardo and Marcia, and my beloved wife Vilma.

Abstract

The objective of this dissertation is to develop numerical methodologies for large eddy simulation (LES) of multiphase cavitating flows over different cavitation regimes. Unstructured grids are considered to enable complex geometries to be considered. The dissertation has the following major components: (i) a compressible homogeneous approach for a mixture of water–vapor–gas is developed to study the effect of non–condensable gas on bluff–body cavitation. (ii) Incipient cavitation in the shear layer of a backstep is studied using incompressible simulations of the flow field coupled with a continuum equation for vapor volume fraction. (iii) The inception model is extended to account for multiple groups of bubbles of different sizes and used to investigate the effects of water quality on tip vortex inception.

A numerical method based on the homogeneous mixture model, fully compressible formulation and finite rate mass transfer developed by Gnanaskandan and Mahesh [1] is extended to include the effects of non–condensable gas (NCG). We then investigate cavitation over a circular cylinder at two different Reynolds numbers ($Re = 200$ and 3900 based on cylinder diameter and free–stream velocity) and different cavitation numbers. Two different cavitation regimes are observed depending on free–stream pressure: cyclic and transitional. In the cyclic regime, the cavitated shear layer rolls up into vortices, which are then shed from the cylinder, forming the Kármán vortex street, similar to a single phase flow. In the transitional regime, a cavity is formed behind the cylinder, and is only detached after the passage of a condensation shock. As a consequence, there is a drastic drop in shedding frequency. Dynamic mode decomposition (DMD) is performed to explain this change in behavior. DMD reveals that cavitation delays the

first transition of the Kármán vortex street. The effects of the non–condensable gases on this flow is discussed for both regimes, and it is found that the gas decreases the strength of the condensation shock. It is observed that vapor and gas uniformly introduced in the free–stream, distributed themselves differently in the wake of cylinder depending upon local flow conditions, particularly at lower cavitation numbers as the pressure in the wake dropped below vapor pressure. Vapor and NCG distribution in the boundary layer suggest that cavitation as a mass transfer process only occurs inside a fine layer in the near–wall region, while the remaining boundary layer only undergoes expansion of both vapor and gas. The levels of free–stream void fraction are found to have an impact on the boundary–layer separation point. Vortex stretching and baroclinic torque are greatly reduced in the transitional regime compared to the cyclic regime.

Next, the development of a method to simulate cavitation in the incipient regime is presented. The main idea is that since inception is a stochastic process that generates small amounts of vapor for short periods of time, the effects of these small regions of vapor on the liquid density and dynamics can be neglected. Therefore, vapor is treated as a passive scalar in an incompressible liquid. Thus, the equations solved are the incompressible Navier–Stokes equation along with a advection–diffusion equation with source terms for the transport of vapor. The scalar field, however, is advanced in time with a different time step than the one used to advance the velocity field. The model is used to investigate inception in the shear layer of a backward–facing step at $Re_\tau = 1500$ (based on skin friction velocity and boundary layer thickness). Statistics are computed for both pressure and vapor volume fraction, and the likelihood of inception is determined. The locations of the preferred sites for cavitation are compared to experimental results and good agreement is achieved. The effects of finite rate evaporation and condensation are revealed by the probability density functions of pressure and volume fraction. The flow topology is investigated and inception is found to occur in the core of the stretched tubular vortical structures with a rotation rate four times higher than the stretching rate. These cavitating tubular structures are elongated two to three times more in their most extensive principal direction than in their intermediate principal direction, and are most likely aligned with the streamwise direction.

The model developed for cavitation inception is extended to account for multiple groups of bubbles of different sizes, effectively making it a polydisperse model. This allows us to investigate the effects of water quality on inception. The model is used to simulate inception in a tip vortex of an elliptic hydrofoil at 12 degrees angle of attack and Reynolds numbers of 9×10^5 and 1.4×10^6 based on root chord length and free–stream velocity. It was found that inception is strongly dependent on the amounts of nuclei in the freestream. When the flow is depleted of nuclei, inception is an intermittent event confined to a position very close to the hydrofoils tip. However, when the flow is rich in nuclei, a larger portion of the tip vortex cavitates, as well as part of the suction side very close to the leading edge of the hydrofoil. Probability density functions reveal that cavitation occurs in any region experiencing a pressure field lower than vapor pressure when the flow is rich in nuclei, while extremely low values of pressure (usually kPa of tension) are required to make a flow deplete of nuclei cavitate. The topology of a flow poor in nuclei was investigated and inception was found to occur in regions dominated by irrotational straining with high stretching rates. Particles were released from the hydrofoil tip and tracked. It is seen that at the higher Reynolds number, the particles are more likely to experience low pressures. However, the amount of time they are subject to very low pressures is shorter at the higher Reynolds number.

Contents

List of Tables

List of Figures

Chapter 1

Introduction

1.1 Cavitation

Cavitation refers to the phase change of liquid into vapor when pressure drops below the liquid vapor pressure (p_v). The vapor pressure is an important fluid property and is defined as the pressure exerted by the vapor in thermodynamic equilibrium with its condensed phase at a given temperature. The vapor pressure of water at 298 K is 2700 Pa, while the vapor pressure at 373 K (boiling point of water) is 1 atmosphere. The difference between the ambient pressure and the vapor pressure is an indicator of whether cavitation can occur or not. Thus, a non–dimensional parameter termed cavitation number, $\sigma = \frac{p_\infty - p_v}{0.5\rho_\infty u_\infty^2}$, is used to characterize cavitating flows. Here, p_∞, ρ_∞ and u_∞ are free–stream pressure, density and velocity respectively. Cavitation can be classified as hydrodynamic, acoustic, optic or particle cavitation. Hydrodynamic cavitation is caused by pressure variations induced due to the geometry, it is often encountered in hydrodynamic applications (e.g., marine propulsors, turbomachinery) and it is a major source of noise and material damage. Acoustic cavitation is caused by pressure variations due to a traveling acoustic wave and it is more common in the medical field (e.g. the use of ultrasound to break kidney stones). Optic and particle cavitation are caused due to local energy deposition using high intensity photons and charged particles respectively. The focus of this dissertation is the hydrodynamic cavitation,

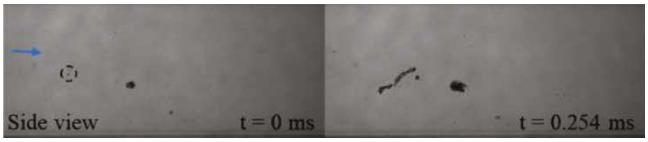

Figure 1.1: Inception in a shear layer [4].

however the methodology and physical insights obtained can be extended to other types of cavitation.

1.1.1 Regimes of cavitation

Cavitation in marine applications (e.g. propellers, hydrofoils) exists over different regimes - ranging from inception to massive regions of vapor. The various regimes can be observed as the cavitation number (σ) in the decreases, thereby generating more and more vapor. As the cavitation number decreases, the cavitation regime changes from inception to developed cavitation and finally to supercavitation.

Cavitation inception

Inception is the first stage of cavitation defined by low amounts of vapor produced for short periods of time. This process is possible due to a decrease of the liquid tensile strength by the presence of micro particles or micro bubbles (called nuclei) that are the starting point of its breakdown. This process is stochastic by nature. For example, in certain problems where the ambient pressure is relatively high and no cavitation is expected, some random and intermittent cavitation events can be observed. This usually occurs in problems where the pressure fluctuations can be extreme, such as in a shear layer or during a vortex pair interaction. Interestingly, in such flows, inception is observed to occur in the weaker vortices [2, 3]. A visual example is given in figure 1.1.

Developed cavitation

With a reduction in σ, vapor bubbles grow into large cavities forming sheet–like structures attached to the body. The sheet cavity intermittently sheds into the cloud, referred

Figure 1.2: Sheet to cloud cavitation over a hydrofoil with a detached cloud cavity [8].

to as "sheet to cloud transition" as can be seen in figure 1.2. It has been observed in past works that the formation of a re–entrant jet triggers the sheet to cloud transition [5]. More recently studies, such as Ganesh et al. [6] and Bhatt and Mahesh [7], observed that if the σ is sufficiently low, the sheet to cloud transition can happen due to the propagation of bubbly shock waves (also called "condensation shock waves"). Once the shed cavity reaches a region of high pressure, it collapses fiercely releasing shock waves that contribute to material damage and erosion.

Supercavitation

With yet further reduction in σ, the cavity can becomes large enough to encompass the object traveling through the liquid. This is known as "supercavitation". Sometimes this can be artificially generated by injecting non–condensable gas around the body. This is called "ventilated supercavitation", and it has potential applications in drag and noise reduction in high–speed underwater transportation. An example is given in figure 1.3.

In this dissertation, we focus on the inception and the developed cavitation regimes.

Figure 1.3: Example of supercavitation [9].

1.2 Motivation

Cavitation is usually undesirable. In marine applications, the vapor pockets produced by cavitation can collapse near a solid surface generating high impact loads on the surface. This leads to adverse performance and also reduce the overall structural integrity. In addition, erosion due to cavitation can cause undesirable noise. Figure 1.4 shows a propeller blade damaged due to cavitation. In the biomedical field, however, cavitation can have beneficial applications. Cavitation bubbles are now used in a remarkable range of surgical and medical procedures, for example to emulsify tissue (most commonly in cataract surgery or in lithotripsy procedures for the reduction of kidney and gall stones) or to manipulate the DNA in individual cells [10]. The importance of studying cavitation lies in its occurrence in these wide array of applications. A deep understanding of cavitation is therefore necessary, if we are to reduce the detrimental effects it causes while also exploiting its beneficial effects.

A study of cavitation can be realized both experimentally and through numerical simulations. Although experimental measurements have extended our understanding of the phenomenon [11, 12], each cavitation regime poses unique challenges. Numerical simulations can therefore potentially fill critical gaps in our understanding, which can lower costs. The numerical simulation of cavitating flows, however, has its own set of challenges. Cavitating flows pose the inherent challenge of ranging over a wide array of length and time scales. Additionally, the formation of vapor is often followed by growth of vapor cavities which not only vary in size but also form and collapse at different rates, making their prediction difficult. Inception is commonly simulated using an Euler–Lagrange framework, where the liquid follows the incompressible Navier–Stokes

equations and each bubble is tracked individually with the equations of motion coupled with the Rayleigh–Plesset equation for their size [13–16]. For a more developed cavitation, usually a compressible formulation using the homogeneous mixture approach is preferred [1, 7, 17–19]. The difference in approaches lies on the distinct characteristics of both regimes. For developed cavitation, the presence of regions with large amounts of vapor can make the flow locally supersonic. This can lead to the formation of shock waves and the use of a compressible formulation for the equations becomes more appropriate. For inception however, the use of the compressible equations can be very expensive. This is because numerically capturing inception requires very low values of free–stream volume fraction [20]. This increases the speed of sound in the mixture and the stiffness of the system of equations.

Traditionally, time averaged methods like Reynolds Averaged Navier–Stokes (RANS) method have been used to simulate cavitation [21–23]. However, standard RANS models require modifications to eddy viscosity for predicting sheet to cloud cavitation [24]. Direct Numerical Simulation (DNS) is a methodology where all relevant scales of turbulence are directly resolved on the computational grid. However, practical flows have high Reynolds number (defined as $Re = \frac{\rho_r u_r L_r}{\mu_r}$, where ρ_r, u_r, L_r and μ_r are a reference density, velocity, lenght and dynamic viscosity respectively) and a large range of length and time scales which makes DNS prohibitively expensive. In recent years, there has been a growing interest in performing LES (Large Eddy Simulation) for cavitating flows [25–27]. LES resolves larger length scales and models the small unresolved scales to account for the inter–scale interaction between the resolved and unresolved scales. This is attractive because many important characteristics of the flow are retained by resolving the largest turbulence scales. As a result, LES is computationally cheaper than DNS, and hence viable for such complex flows.

It is clear that the numerical modeling of cavitating flows is a challenging task. It requires the uniqueness of each regime to be carefully addressed. An overall objective of this dissertation is to develop LES methods to simulate cavitating flows in the inception and developed cavitation regimes.

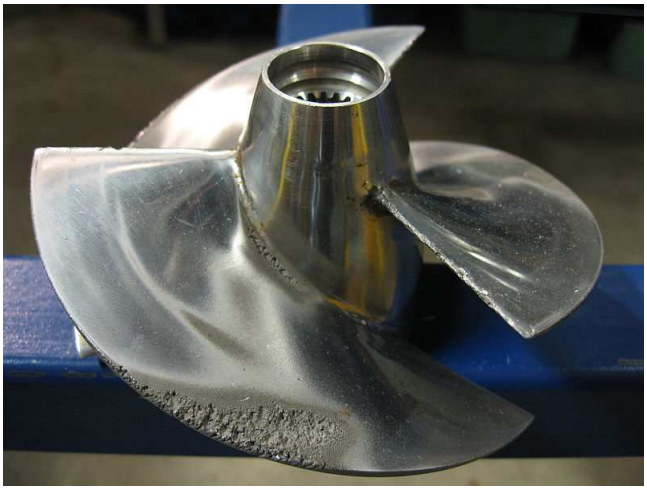

Figure 1.4: Example of material erosion due to cavitation [8].

1.3 Overview

The objective of this dissertation is to develop numerical methodologies for LES of multiphase cavitating flows over different cavitation regimes. The dissertation has three major components: (i) a compressible homogeneous approach for a mixture of water–vapor–gas is developed to study the effect of non–condensable gas on bluff–body cavitation. (ii) Incipient cavitation in the shear layer of a backstep is studied with an approach that treats vapor as a passive scalar in an incompressible liquid. (iii) The inception model is extended to account for multiple groups of bubbles of different sizes and used to investigate the effects of water quality on tip vortex inception.

1.3.1 Effect of NCG on cavitation behind a circular cylinder

Fry [28] characterizes the developed cavitation over a circular cylinder as belonging to cyclic and transitional regimes. As the cavitation number in the free–stream decreases, cavities develop inside the core of the vortices shed from either side of the cylinder, which is referred to as cyclic cavitation. Further reduction in σ, leads to the transitional regime. In this case, the cavities grow larger in size and begin to interact with each other, causing the cavity shedding to become irregular, until they coalesce to form a single

cavity fixed to the cylinder. The noise and erosion rates peak at the transition from the cyclic to the transitional regime as the cavities begin to interact [28]. In the present investigation, we study cavitation over a circular cylinder over a range of σ spanning non–cavitating, cyclic and transitional cavitation regimes. We observe that cavitation inside the Kármán vortices in the cyclic regime, is significantly altered at the onset of "condensation shock" propagation in the transitional regime. At the transition, an order of magnitude jump in shedding Strouhal number, a peak in pressure fluctuations and a maximum in St versus σ based on a cavity length are observed, in agreement with experimental results from Fry [28]. Hence, changes in shedding characteristics in these regimes and condensation shock propagation are studied. It is also known that, NCG can change acoustic properties such as sound speed, acoustic impedance and consequently the shock propagation. This motivates the study of NCG effects on cavity shedding and condensation shock propagation.

It is known that the sound speed of the two–phase water–vapor mixture is orders of magnitude smaller than the speed of sound of its constituent phases [29]. If the sound speed becomes comparable to the magnitude of the velocities in the flow, it can lead to the formation of shock waves. Observation of shock waves in bubbly mixtures have been made as early as 1964 in the head breakdown process in cavitating inducers [30], although, "condensation shock" propagation as a mechanism for partial cavity shedding has been shown only recently [6]. Note that "condensation shocks" refer to shock waves associated with a retracting partial cavity, typically have a weak discontinuity in pressure (order of few kpa) and involve phase change [18]. Subsequent to Ganesh et al. [6], various computational and experimental studies have considered condensation shock propagation as a mechanism in context of sheet to cloud cavitation [7, 18, 31–33]. In these studies, at sufficiently small σ, the sheet to cloud transition is observed by the propagation of condensation shocks, instead of the classically observed re–entrant jet mechanism [34]. Similarly, in the present work involving bluff body cavitation, with a significant reduction in σ (moving from the cyclic to the transitional regime), we observe that the condensation shock propagation rather than a periodic cavitation inside Kármán vortices dominate the cavity shedding.

Presence of NCG can influence cavitating flows in various ways [35–40]. Influence of dissolved and injected NCG in partial cavitation over a wedge has been considered by Makiharju et al. [38]. They found that injection of NCG into the cavity suppressed vapor formation altering the dynamics of condensation shock formation. Vennig et al. [39] in the experimental investigation on a flow over a hydrofoil observed that for the flow rich in vapor/NCG nuclei, multiple shock waves are necessary for complete condensation and detachment of the cavity. Trummler et al. [40] concluded that gas present in vapor bubbles would lead to stronger rebound and dampen the emitted shockwaves. In such flows it is also important to note the influence of nuclei content of vapor/NCG. At a pressure lower than the vapor pressure, cavitation is triggered by imperfections in water, that are mostly small NCG or vapor bubbles (known as cavitation nuclei) that initiates the liquid breakdown [29]. In addition, NCG can behave differently from vapor in response to pressure variations; gas can only experience volume change due to expansion/compression, while vapor can in addition, undergo phase change due to evaporation/condensation. Since the NCG does not undergo phase change, the flow is more sensitive to the nuclei content of initially present NCG in the system than vapor. Numerical studies involving fully compressible formulation and a homogeneous mixture approach often use relatively high values of free–stream nuclei [7, 41–44], to avoid extremely small time steps due to low Mach numbers in water. The studies have shown that good agreement with experiment is observed for large regions of vapor and developed cavitation regimes [7, 41, 43]. Although, cavitation inception and incipient cavitation are known to be highly sensitive to the nuclei size and their distribution [15]. Hence, in the present work, we also consider the effect of free–stream nuclei of vapor/NCG on the cylinder wake.

Single phase flow over circular cylinders have been studied extensively in the past. Limited studies exist on the cavitating flow over a cylinder [28, 42, 44–48]. Fry [28] investigated cavity dynamics in the cylinder wake by measuring noise spectra. The author observes a peak in pressure fluctuations as the cyclic cavitation inside the periodic vortex shedding, transitions (with the reduction in σ) to irregular–regular vortex shedding, and eventually to a fixed cavity. Seo et al. [42] studied cavitating flow at

$Re = 200$ and observed that the shock waves generated by the coherent collapse of the vapor cloud significantly change the aerodynamic noise characteristics. Kumar et al. [48] studied the cavitating structures of the near–wake of a circular cylinder for a subcritical Reynolds number and concluded that the cavities originate primarily in the free shear layer, not in the wake or in the attached boundary–layer. For the cyclic cavitation, Gnanaskandan and Mahesh [44] explained the reduction in Kármán shedding frequency with the reduction in free–stream σ, using the increase in the vorticity dilatation term due to cavitation. At lower σ, they observe condensation front propagation for the transitional regime, but do not discuss the nature of the front or the alteration in shedding characteristics. Effects of NCG are not discussed in any of these works.

1.3.2 Cavitation inception in shear layers

As previously mentioned in subsection 1.1.1, inception is defined by small amounts of vapor production for brief periods at a relative high σ. It is commonly observed in flows where the pressure fluctuations can be extreme. Consequently, shear flows are often more prone to cavitation than streamlined bodies, resulting in considerably higher inception σ. Cavitating shear flows have been investigated in the past. Katz and O'Hern [49] observed that the first traces of cavitation appear as a series of narrow and long axial structures located between spanwise eddies. This was later confirmed in O'Hern [2], where the incipient streamwise vortices showed a strength less than 10% of that of the spanwise vortices. Interestingly, Iyer and Ceccio [50] noticed that cavitation does not significantly alter the overall formation, growth and convection of the primary and secondary vortices. The same behavior was observed later by Aeschlimann and Barre [51], but the reattachment point was found to depend on σ. Studies conducted by Agarwal et al. [4] revealed that regions most likely to cavitate move upstream with decreasing σ and increasing velocity. The work of Agarwal et al. [52] showed that the Reynolds number has a strong influence on the time the pressure remains below vapor pressure inside the streamwise vortices. In a similar experiment as the one from Agarwal et al. [52], but at a higher Re, Barbaca et al. [53] observed that the collapse of the initial incipient cavity results in a remnant micro–bubble population that gets

dispersed into the shear layer and re–circulation zone in the wake of the step, triggering the formation of developed cavitation. Later in the same experiment, Allan et al. [54] injected a population of large monodisperse nuclei and found that the inception event rate follows a power law with cavitation number and vary linearly with the injection rate.

Experimentally, inception can be determined through visual or acoustical techniques where the measurements detect events per unit time above a certain threshold [55]. Numerous factors can affect the conditions for inception. As observed by Katz and O'Hern [49], Arndt et al. [56] and Khoo et al. [57], the cavitation number associated with the appearance of inception has a strong dependence on the air content of the fluid and the population of bubbles in the free–stream. Arndt and Keller [58], through visual detection, observed that inception in tip vortices would start at higher σ for "weak" water (water where the tensile strength was reduced by the presence of bubbles) and that it was highly intermittent, as opposed to the sudden appearance of a well defined cavitating structure for the "strong" water. The decrease in the inception σ can be approximately 60% with increasing water tension for tip vortex cavitation [59]. Besides, Peterson [60] found a disagreement between the determination of inception using visual and acoustical measurements in a water tunnel with large nuclei concentration. Interestingly, Khoo et al. [57] found that the desinence of cavitation (disappearance of cavitation by slowly increasing σ) is largely independent of the nuclei population.

It was previously observed by Katz [61], Katz and O'Hern [49] and O'Hern [2] that the inception σ typically increases with Reynolds number in shear layers. A larger Re produces a wider frequency spectrum, increasing the likelihood of instantaneous pressure reaching values below vapor pressure [55]. Due to this unsteady and statistical nature of inception, LES is preferred over RANS for numerical simulations. Early studies compared the performances between LES and RANS [62, 63] for cavitation and concluded that small–scale and transient behaviors are better captured by LES. In flow over propeller blades, for instance, Lu et al. [64] observed that RANS is not capable of capturing the tip vortical structures, which is detrimental for predicting inception. In a similar problem, Bappy et al. [65] showed that the inception σ predicted by LES

matches the experimental value, while it is underpredicted by RANS. The use of RANS was also found to predict the low–pressure region farther away from the blade.

1.3.3 Tip vortex cavitation

The transverse flow caused by the pressure difference between the pressure and suction sides of a finite–span wing/blade, winds around its tip to form the so–called tip vortex, which is attached to the vortex sheet formed by the vortex shedding along the span of the wing/blade. Moore [66] suggested that a finite vortex sheet with a tip vortex at its end undergoes a spiral roll–up as it evolves downstream. This in turn entrains some vorticity in the tip vortex, causing an instantaneous change in the velocity field at the locations of other vortices. These perturbations lead to the Kelvin–Helmholtz instability in the region between the tip vortex and the unstretched part of the vortex sheet. Once the roll–up is complete, the tip vortex evolves further downstream in a complex manner depending on the physical conditions and geometry of the problem.

Depending on the roll–up process in the near field, the pressure in the tip vortex core can drop below vapor pressure making it susceptible to cavitation. Followed by the pioneering work of McCormick Jr [67], tip vortex cavitation (TVC) has been widely studied in the past as reviewed by Arndt [12]. With the goal of understanding tip vortex cavitation in marine propellers, many past studies simplified the problem and studied the tip vortices generated by fixed hydrofoils [68–72]. Arndt et al. [56] observed that the cavitation number associated with the inception of the tip vortex has a complex dependence on the Reynolds number and on the water quality (population of bubbles in the freestream). Arndt and Keller [58], through visual detection, observed that inception in tip vortices would start at higher σ for "weak" water (water where the tensile strength was reduced by the presence of a large number of bubbles). Interestingly, Khoo et al. [57] found that the desinence of cavitation (disappearance of cavitation by slowly increasing σ) is largely independent of the nuclei population. Boulon et al. [70] studied confined flow over a three–dimensional elliptical hydrofoil NACA 16–020. The flow was confined by the presence of fixed side–walls in their water tunnel as well as by an adjustable flat bottom wall, which could be moved in their experiments

to achieve a desirable tip gap (e). They found that as e becomes smaller, the tip vortex becomes more susceptible to cavitation up to a certain value of e due to increase in the peak of swirl velocity. Beyond that, decreasing e does not cavitate the flow. Asnaghi et al. [73] performed numerical simulations of a NACA 66(2)–415 and found that cavitation increases the tip vortex diameter. Xie et al. [74] investigated cavitation of the tip vortex from a NACA 16–020 elliptic hydrofoil and found that cavitation promotes the production of vorticity and increases the boundary–layer thickness. Shin et al. [75] compared cavitation characteristics over two different hydrofoils: NACA 16–020 and NACA 66(2)–415. They found that the development process of TVC, including inception, is shown to occur in six different stages, with decreasing σ.

Simulating tip vortex behind hydrofoils has two major challenges: (i) flow over the hydrofoil surface and (ii) the tip vortex interactions with walls. Flow over the hydrofoil is computationally challenging due to high Re which demands fine resolution near wall to capture boundary–layers. Depending on the physical conditions such as Re and angle of attack, the flow on the hydrofoil can be laminar or transitional, and it can separate on the suction side of the hydrofoil causing large unsteadiness. The unsteadiness can be enhanced further if the flow is confined. The tip vortex has a tiny core which needs to be resolved throughout the length of the simulation domain. Maintaining grid quality becomes challenging at small tip gaps. The turbulence in the wake decays moving downstream. Thus, this problem demands an accurate and robust numerical method to capture the essential flow features. Direct numerical simulation (DNS) of the flow is not feasible for this problem. Therefore, large eddy simulation (LES) is commonly used to simulate this problem due to its predictive capability, which has been demonstrated in literature for a variety of complex marine flow problems [76]. LES has been also used in past to study the effect of tip–gap on the flow field in a turbomachinery cascade [77]. Mahesh et al. [78] developed a non–dissipative and robust finite volume method suitable for LES of turbulent flows on unstructured grids, which has been used to accurately simulate a variety of marine flows including flow over hull [79] and propellers [80–83].

LES is performed for flow over the three–dimensional elliptical hydrofoil NACA 16–020, which has been used in numerous past studies [68–72]. Most LES of cavitation has

been applied to attached or sheet–to–cloud regimes using compressible formulations of the homogeneous mixture equations. The inception regime has received less attention in numerical simulations, despite being important for practical applications. Inception occurs in the regime of low void fractions where the compressible governing equations can be argued to reduce to the zero–Mach equations which imply the use of the incompressible governing equations along with the same vapor volume fraction transport equation as the compressible equations. Most numerical studies of tip vortex at the incipient regime employ a Euler–Lagrange framework, where the liquid follows the incompressible Navier–Stokes equations and each bubble is tracked individually with the equations of motion coupled with the Rayleigh–Plesset equation for their size [14, 15, 84, 85]. This approach can bring more details on the interactions of the nuclei and tip vortex, however the extra cost of modeling the nuclei dynamics can be sometimes prohibitively. As a remedy, here we use a polydisperse model which is presented in section 5.1. A polydisperse model uses a population balance equation, which is an equation that accounts for the spatial and temporal evolution of the number density function in a single control volume, and it is often solved with the discrete method or with the method of moments. In the discrete method (also called the multigroup method), the disperse population is discretized into a finite number of size intervals or bins. For the method of moments, the population balance equation is transformed into a set of transport equations for moments of the distribution. The model developed in section 5.1 is based on the discrete method.

1.4 Principal Contributions

The principal contributions of this work are as follows:

1.4.1 Effect of non–condensible gas

- The compressible homogeneous mixture model is extended to consider a water–vapor–gas mixture.

- The method is used to study the developed cavitation regime in flow over a circular cylinder at different σ, Re, and with different amounts of free–stream vapor and gas volume fraction. The developed cavitation regime in bluff bodies can be divided into two sub–regimes with decreasing σ: cyclic and transitional. It was found that the shedding frequency changes by $O(1)$ when σ is reduced from the cyclic to the transitional regime.

- Dynamic Mode Decomposition of the flow was performed. The results revealed that cavitation delays the transition of the Kármán vortex street, which is related to the difference in shedding frequency between regimes.

- The effects of non–condensable gas (NCG) in the flow were investigated in detail. As σ is dropped, the NCG can delay the transition from the cyclic to the transitional regime. In the transitional regime, the NCG lowers the strength of the condensation shock, which is responsible for the cavity shedding in the transitional regime.

- The effects of the amounts of free–stream vapor/gas volume fraction on the flow were studied. It was found that the boundary–layer separation point moves downstream as the free–stream volume fraction is increased.

1.4.2 Shear layer inception

- A method to simulate cavitation under incipient conditions is developed. The method treats vapor as a passive scalar in a incompressible liquid. The scalar field is advanced in time with a different time step than the one used for the velocity field, to lower computational cost.

- The method was used to study the inception regime in a flow over a backward–facing step at two values of σ and at $Re_\tau = 1500$, based on boundary–layer thickness and skin friction velocity.

- The mean and RMS velocity profiles obtained are compared to experiments and

good agreement is observed, suggesting that the pressure field is accurately predicted.

- Probability density functions of pressure and vapor void fraction were computed, and the regions most likely to experience inception were obtained and shown to be in good agreement with experiments.

- The flow topology was investigated using the invariants of the velocity gradient, strain rate and rotation rate tensors. It was found that inception is more likely to occur in the cores of elongated quasi–streamwise vortices, whose rotation rate is around four times larger than their stretching rate.

1.4.3 Polydisperse model and tip vortex cavitation

- A polydisperse approach is used to study tip vortex cavitation under inception conditions. This model allows the study of water quality effects on the flow.

- Water quality was found to have a larger impact on inception characteristics than the Re. It is observed that when the flow is depleted of nuclei, inception is less susceptible to small changes in the Reynolds number.

- When the flow is depleted of nuclei, inception was found to occur in regions with extremely low values of pressure (usually kPa of tension). In contrast, when the flow is rich in nuclei, inception occurs anywhere that experiences pressure lower than vapor pressure.

- The flow topology of the incipient structures were investigated for the 'natural case', and it was found that inception has a higher likelihood of occuring in focal regions dominated by irrotational straining with high stretching rates.

1.5 Outline

The dissertation is organized as follows. Chapter 2 explains the physical model used in the simulations. It also outlines the governing equations being solved for both the

developed and the inception regimes, and the numerical methods used to solve them. An investigation of the developed cavitation behind a circular cylinder at two Reynolds numbers and multiple cavitation numbers is presented in Chapter 3. A study of inception in the shear layer of a backward–facing step is described in Chapter 4. A polydisperse extension to the inception model and a study of inception in the tip vortex of an elliptic hydrofoil is presented in Chapter 5. Finally, Chapter 6 provides a brief summary of the dissertation.

Chapter 2

Physical Models and Numerical Methods

This chapter is organized as follows. Section 2.1 discusses the governing equations and the physical model used for the developed cavitation regime, including the extension to add non–condensable gas in the mixture, as well as the numerical method used. Section 2.2 presents the governing equations and numerical method to be employed in the inception regime.

2.1 Developed cavitation regime

Numerical methods for the developed cavitation which include the effects of NCG were often based on incompressible Navier–Stokes equations [21, 86, 87]. More recently, fully compressible formulations have been employed [37, 88]. In the present work, the numerical method of Gnanaskandan and Mahesh [1] based on fully compressible formulation for the vapor–water mixture is extended to account for NCG. The ideal gas equation of state is used for NCG and is coupled with the stiffened equation of state for water and ideal gas equation for vapor, to derive the mixture equation of state. The mixture sound speed is obtained from the mixture equation of state and Gibbs equation. Transport equations for the non–condensable gas and the vapor mass fraction are solved along with

the compressible Navier–Stokes equations for the mixture quantities. Both vapor and NCG are uniformly introduced in the free–stream in terms of volume fraction. However, separate transport equations for vapor and gas allow both to evolve in a different manner depending upon the local flow conditions.

2.1.1 Physical model and governing equations

We use the homogeneous mixture approach where the mixture of water, vapor and non–condensable gas (NCG) is considered as a single compressible medium. We assume mechanical equilibrium (i.e. each phase shares the same velocity and pressure) and thermal equilibrium (i.e. each phase shares the same temperature). Surface tension effects are assumed small and hence neglected. The governing equations are the compressible Navier–Stokes equations for the mixture quantities along with transport equations for vapor and NCG. Different from the works of Orley et al. [37] and Mithun et al. [88], where the homogeneous equilibrium barotropic model is employed, here we assume a finite mass transfer rate between vapor and water, which is explicitly modeled through source terms. These equations are Favre averaged and spatially filtered to perform large–eddy simulation. The subgrid terms are modeled with the dynamic Smagorinsky model. The unfiltered equations are:

$$\begin{aligned}
\frac{\partial \rho}{\partial t} &= -\frac{\partial}{\partial x_k}\left(\rho u_k\right), \\
\frac{\partial \rho u_i}{\partial t} &= -\frac{\partial}{\partial x_k}\left(\rho u_i u_k + p\delta_{ik} - \sigma_{ik}\right), \\
\frac{\partial \rho e_s}{\partial t} &= -\frac{\partial}{\partial x_k}\left(\rho e_s u_k - Q_k\right) - p\frac{\partial u_k}{\partial x_k} + \sigma_{ik}\frac{\partial u_i}{\partial x_k}, \\
\frac{\partial \rho Y_v}{\partial t} &= -\frac{\partial}{\partial x_k}\left(\rho Y_v u_k\right) + S_e - S_c, \\
\frac{\partial \rho Y_g}{\partial t} &= -\frac{\partial}{\partial x_k}\left(\rho Y_g u_k\right).
\end{aligned} \tag{2.1}$$

Here ρ, u_i, e_s and p are density, velocity, internal energy and pressure of the mixture respectively. Y_v is the vapor mass fraction and Y_g is the NCG mass fraction. The

mixture density is defined as

$$\rho = \rho_l(1 - \alpha_v - \alpha_g) + \rho_v\alpha_v + \rho_g\alpha_g, \tag{2.2}$$

where ρ_l, ρ_v and ρ_g are densities of liquid, vapor and gas respectively. α_v and α_g are the volume fractions of vapor and NCG respectively. Volume fractions of each constituent phase are related to their respective mass fractions as

$$\rho_l(1 - \alpha_v - \alpha_g) = \rho(1 - Y_v - Y_g), \quad \rho_v\alpha_v = \rho Y_v \quad \text{and} \quad \rho_g\alpha_g = \rho Y_g. \tag{2.3}$$

The internal energy of the mixture is obtained by mass weighted average of its constituent phases:

$$\begin{aligned} \rho e_s &= \rho(1 - Y_v - Y_g)e_l + \rho Y_v e_v + \rho Y_g e_g, \quad \text{where} \\ e_l &= C_{vl}T + \frac{P_c}{\rho_l}, \\ e_v &= C_{vv}T \quad \text{and} \\ e_g &= C_{vg}T. \end{aligned} \tag{2.4}$$

Here, e_l, e_v and e_g are the internal energies of liquid, vapor and NCG respectively and C_{vl}, C_{vv} and C_{vg} are their specific heats at constant volume respectively. The system is closed using a mixture equation of state obtained using stiffened equation of state for the liquid and ideal gas equation of state for both vapor and NCG:

$$p = Y_v\rho R_v T + Y_g\rho R_g T + (1 - Y_v - Y_g)\rho K_l T\frac{p}{p + P_c}, \tag{2.5}$$

where $R_v = 461.6J/(KgK)$, $R_g = 286.9J/(KgK)$, $K_l = 2684.075J/(KgK)$ and $P_c = 786.333 \times 10^6 Pa$ are the constants associated with equation of state of the mixture. Parameters for the stiffened equation of state used for water are derived by Gnanaskandan and Mahesh [1] to match speed of sound in liquid at a given density. Parameters for the gas and vapor equations of state are taken from White [89] and Saito et al. [41] respectively. Hence, the current approach accurately predicts the liquid speed of sound and

density variation as shown in Gnanaskandan and Mahesh [1], although the specific heat at constant volume is under predicted ($1500 J/Kgk$ as compared to the NIST value of $4157.4. J/Kgk$). This however, is not considered as a serious drawback, considering the isothermal nature of cavitation [19]. In addition, numerical studies of Gnanaskandan and Mahesh [1] have demonstrated validation of the numerical method using stiffened equation of state for variety of flow problems for the study of hydrodynamic cavitation.

The viscous stress tensor (σ_{ij}) and heat flux vector (Q_j) are given by

$$\sigma_{ij} = \mu(\frac{\partial u_i}{\partial x_j} + \frac{\partial u_j}{\partial u_i} - \frac{2}{3}\frac{\partial u_k}{\partial x_k}\delta_{ij}) \quad \text{and} \quad Q_j = k\frac{\partial T}{\partial x_j}, \tag{2.6}$$

where the mixture thermal conductivity is defined as a volume average between the conductivities of the individual constituent phases. For the mixture viscosity, we follow Beattie and Whalley [90] and assume that the effective dynamic viscosity of the liquid–vapor–gas mixture satisfies a quadratic law with a maximum in the two–phase region. The mixture thermal conductivity and viscosity are given in equation (2.7) as

$$\begin{aligned} &\mu = \mu_l(1-\alpha_v-\alpha_g)(1+2.5(\alpha_v+\alpha_g)) + \mu_v\alpha_v + \mu_g\alpha_g \quad \text{and} \\ &k = k_l(1-\alpha_v-\alpha_g) + k_v\alpha_v + k_g\alpha_g. \end{aligned} \tag{2.7}$$

In equation (2.7), k_l, k_v, and k_g are thermal conductivities of water, vapor and NCG respectively while μ_l, μ_v and μ_g are the dynamic viscosities of water, vapor and NCG respectively. Note that $\mu_l >> \mu_v, \mu_g$. A simple volume average would give maximum in the liquid region for $\alpha_v + \alpha_g = 0$ (i.e. in liquid), while a quadratic dependence from Beattie and Whalley [90] yields an initial increase in the mixture viscosity, moving from liquid to the mixture. The mixture viscosity is maximum in the two–phase region near liquid. Molecular dynamics simulations confirm this behavior [91]. They are related to the temperature of the mixture as

$$\mu_l = C_{0l} \times 10^{\frac{C_{1l}}{T-C_{2l}}}, \quad \mu_v = C_{0v}\left(\frac{T}{T_{0v}}\right)^{n_v}, \quad \mu_g = C_{0g}\left(\frac{T}{T_{0g}}\right)^{n_g}, \tag{2.8}$$

where the constants in equation (2.8) and their references are given in table 2.1. Thermal

Water	**Vapor**	**NCG**
$\mu_l = C_{0l} \times 10^{\frac{C_{1l}}{T - C_{2l}}}$	$\mu_v = C_{0v}\left(\frac{T}{T_{0v}}\right)^{n_v}$	$\mu_g = C_{0g}\left(\frac{T}{T_{0g}}\right)^{n_g}$
$C_{0l} = 2.414 \times 10^{-5} Pa \cdot s$	$C_{0v} = 1.78 \times 10^{-5} Pa \cdot s$	$C_{0g} = 1.71 \times 10^{-5} Pa \cdot s$
$C_{1l} = 247.8K$	$T_{0v} = 288K$	$T_{0g} = 273K$
$C_{2l} = 140K$	$n_v = 0.76$	$n_g = 0.7$
[44]	[44]	[92]

Table 2.1: Constants for species viscosity.

conductivity in a constituent phase (k_l, k_v and k_g respectively in liquid, vapor and NCG) is obtained from Prandtl number (Pr) in each phase. Since the maximum observed values of vapor mass fractions in the cases considered are orders of magnitude smaller than unity, latent heat of vaporization can be neglected [1] and it was not considered in the present work. S_e and S_c are the source terms due to evaporation of water and condensation of vapor and are given by

$$\begin{aligned} S_e &= C_e(\alpha_v + \alpha_g)^2(1 - \alpha_v - \alpha_g)^2 \frac{\rho_l}{\rho_v} \frac{max((p_v - p), 0)}{\sqrt{2\pi R_v T_s}} \quad \text{and} \\ S_c &= C_c(\alpha_v + \alpha_g)^2(1 - \alpha_v - \alpha_g)^2 \frac{max((p - p_v), 0)}{\sqrt{2\pi R_v T_s}}. \end{aligned} \tag{2.9}$$

Here T_s is a reference temperature. C_e and C_c are empirical constants based on the interfacial area per unit volume and their values are taken to be equal to 0.1 m^{-1} as described by Saito et al. [41]. They have shown that the solution is not sensitive to the value of empirical constants using cavitating flow over hemispherical/cylindrical bodies. The vapor pressure (p_v) is related to temperature as

$$p_v = p_k exp((1 - \frac{T_k}{T})(a + (b - cT)(T - d)^2)), \tag{2.10}$$

where $p_k = 22.130MPa$, $T_k = 647.31K$, $a = 7.21$, $b = 1.152 \times 10^{-5}$, $c = -4.787 \times 10^{-9}$ and $d = 483.16$ [41]. Vapor pressure variation with temperature obtained from equation (2.10) is compared to the National Institute of Standards and Technology (NIST) data in figure 2.1 showing excellent agreement.

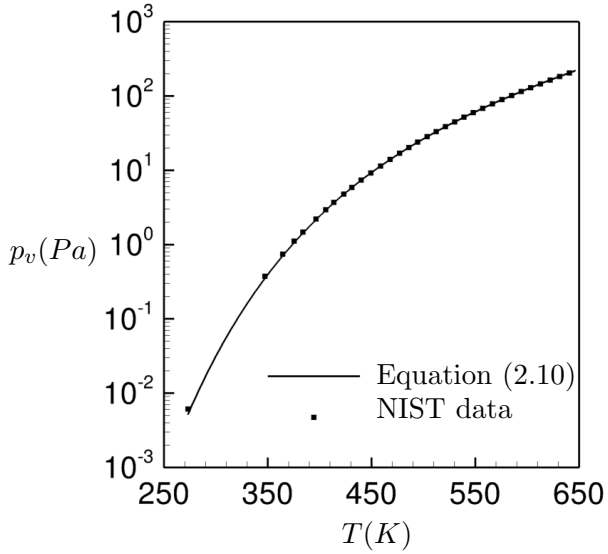

Figure 2.1: Vapor pressure variation with temperature.

The expression for the speed of sound in the mixture is obtained from equation (2.5) and the Gibbs equation, and is given by

$$\begin{aligned} a^2 &= \frac{C_1 T}{C_0 - C_1/C_{pm}}, \quad \text{where} \\ C_1 &= (Y_v R_v + Y_g R_g)(p + P_c) + (1 - Y_v - Y_g) K_l p, \\ C_0 &= 2p + P_c - \rho T (Y_v R_v + Y_g R_g) - (1 - Y_v - Y_g)\rho K_l T \quad \text{and} \\ C_{pm} &= Y_g C_{pg} + Y_v C_{pv} + (1 - Y_v - Y_g) C_{pl}. \end{aligned} \tag{2.11}$$

Here, C_{pv}, C_{pg} and C_{pl} are the specific heats at constant pressure for vapor, NCG and liquid respectively. The speed of sound obtained (equation (2.11)) is compared to the experimentally available data for water–vapor mixture as shown in figure 2.2(a) and water–air mixture in figure 2.2(b). The speed of sound derived in the present work does not consider mass transfer effects, and hence is a frozen speed of sound.

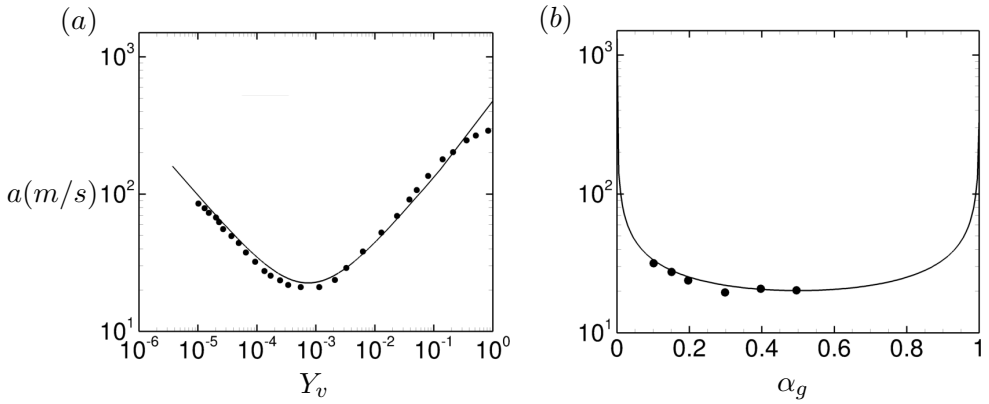

Figure 2.2: Speed of sound in water–vapor mixture (a) and in water–NCG mixture (b). Equation (2.11) (——) is compared with data from Kieffer [93] and Karplus [94] (•) in (a) and (b) respectively.

To perform LES, the equations (2.1) are Favre filtered spatially:

$$\begin{aligned}
\frac{\partial \overline{\rho}}{\partial t} &= -\frac{\partial}{\partial x_k}\left(\overline{\rho}\tilde{u_k}\right), \\
\frac{\partial \overline{\rho}\tilde{u_i}}{\partial t} &= -\frac{\partial}{\partial x_k}\left(\overline{\rho}\tilde{u}_i\tilde{u}_k + \overline{p}\delta_{ik} - \tilde{\sigma}_{ik} - \tau_{ik}\right), \\
\frac{\partial \overline{\rho}\tilde{e}_s}{\partial t} &= -\frac{\partial}{\partial x_k}\left(\overline{\rho}\tilde{e_s}\tilde{u_k} - \tilde{Q}_k - q_k\right) - \overline{p}\frac{\partial \tilde{u_k}}{\partial x_k} + \tilde{\sigma_{ik}}\frac{\partial \tilde{u_i}}{\partial x_k}, \\
\frac{\partial \overline{\rho}\tilde{Y_v}}{\partial t} &= -\frac{\partial}{\partial x_k}\left(\overline{\rho}\tilde{Y_v}\tilde{u_k} - t_{vk}\right) + \tilde{S}_e - \tilde{S}_c, \\
\frac{\partial \overline{\rho}\tilde{Y_g}}{\partial t} &= -\frac{\partial}{\partial x_k}\left(\overline{\rho}\tilde{Y_g}\tilde{u_k} - t_{gk}\right).
\end{aligned} \tag{2.12}$$

Here, the tilde quantities are Favre averaged quantities and τ_{ik}, q_k, t_{vk} and t_{gk} are subgrid scale (SGS) terms namely: SGS stress, SGS heat flux, SGS scalar flux of vapor and SGS scalar flux of NCG respectively. These terms are modeled using the Dynamic Smagorinsky model (DSM) [95]:

$$
\begin{aligned}
\tau_{ij} - \frac{\delta_{ij}}{3}\tau_{kk} &= -2C_S(\mathbf{x},t)\overline{\rho}\Delta^2 \left|\tilde{S}\right| \widetilde{S^*_{ij}}, \\
\tau_{kk} &= 2C_I(\mathbf{x},t)\overline{\rho}\Delta^2 \left|\tilde{S}\right|^2, \\
q_i &= -\overline{\rho}\frac{C_S(\mathbf{x},t)\Delta^2 \left|\tilde{S}\right|}{Pr_T}\frac{\partial \overline{T}}{\partial x_i}, \\
t_{vi} &= -\overline{\rho}\frac{C_S(\mathbf{x},t)\Delta^2 \left|\tilde{S}\right|}{Sc_T}\frac{\partial \overline{Y_v}}{\partial x_i}, \\
t_{gi} &= -\overline{\rho}\frac{C_S(\mathbf{x},t)\Delta^2 \left|\tilde{S}\right|}{Sc_T}\frac{\partial \overline{Y_g}}{\partial x_i},
\end{aligned}
\tag{2.13}
$$

where $|S| = \sqrt{2S_{ij}S_{ij}}$ and $S^*_{ij} = S_{ij} - 1/3S_{kk}\delta_{ij}$. The model coefficients C_s, C_I, Pr_T and Sc_T are determined using the Germano identity. For example,

$$
\begin{aligned}
C_S\Delta^2 &= \frac{1}{2}\frac{\left\langle L^*_{ij}M^*_{ij}\right\rangle}{\left\langle M^*_{ij}M^*_{ij}\right\rangle}, \\
L^*_{ij} &= \left(\frac{\widehat{\overline{\rho u_i}\cdot\overline{\rho u_j}}}{\overline{\rho}}\right) - \frac{\widehat{\overline{\rho u_i}}\cdot\widehat{\overline{\rho u_j}}}{\widehat{\overline{\rho}}}, \\
M^*_{ij} &= \overline{\rho}\widehat{\left|\tilde{S}\right|\widetilde{S^*_{ij}}} - \widehat{\overline{\rho}}\left(\frac{\widehat{\Delta}}{\Delta}\right)^2 \widehat{\left|\tilde{S}\right|}\widehat{\widetilde{S^*_{ij}}},
\end{aligned}
\tag{2.14}
$$

where, $\langle\cdot\rangle$ denotes spatial average over homogeneous direction(s) and the caret denotes test filtering. Test filtering is defined by the linear interpolation from face values of a control volume, which is again the interpolation from two adjacent cell center values [95]:

$$
\widehat{\phi} = \frac{1}{N_{\text{face}}}\sum_{\text{no of face}}\phi_f = \frac{1}{2N_{\text{face}}}\sum_{\text{no of face}}(\phi_{icv1} + \phi_{icv2}), \tag{2.15}
$$

where N_{face} is the number of faces for a given control volume.

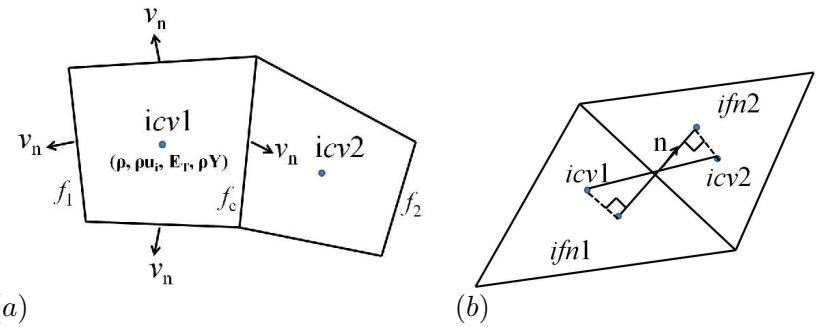

Figure 2.3: (a) Schematic of the collocated finite volume method. (b) Schematic for computation of face normal gradient for viscous terms.

2.1.2 Numerical method

The algorithm uses a predictor–corrector approach. In the predictor step, the governing equations are spatially discretized using a symmetric non–dissipative collocated cell–centered finite volume scheme. Figure 2.3 illustrates the storage of variables and the notation used. The viscous fluxes are split into compressible and incompressible contributions and treated separately. Once the fluxes are obtained, a predicted value is computed using an explicit Adams–Bashforth time integration. The corrector step uses a characteristic based filtering to compute the final solution from the predicted value.

Predictor step

The predicted variables are obtained by solving the discrete forms of equations (2.1) using a cell–centered finite volume method. The discrete forms of the governing equations are obtained by integrating them over a control volume (CV) and applying the Gauss theorem. The discrete continuity equation, for example, has the form

$$\frac{\partial \rho_{\text{cv}}}{\partial t} = -\frac{1}{V_{\text{cv}}} \sum_{\text{faces}} (\rho V_N)_{f_c} A_{f_c}, \tag{2.16}$$

where V_{cv} is the volume of a CV, V_N is the face–normal velocity, and the subscript f_c refers to variables being computed at the face of a computational cell. A_{f_c} is the area of the face. The convective fluxes at the face are first estimated using a symmetric average

with a gradient term using Taylor series expansion to obtain

$$\phi_{f_c} = \frac{\phi_{icv1} + \phi_{icv2}}{2} + \frac{1}{2}\left(\nabla\phi|_{icv1} \cdot \Delta\mathbf{x}^{icv1} + \nabla\phi|_{icv2} \cdot \Delta\mathbf{x}^{icv2}\right), \tag{2.17}$$

where $\Delta\mathbf{x}^{icv1} = \mathbf{x}_{f_c} - \mathbf{x}_{icv1}$, and $\nabla\phi|_{icv1}$denotes the gradient defined at $icv1$. The viscous term is split into two parts, $\sigma_{ij} = \sigma^1_{ij} + \sigma^2_{ij}$, where $\sigma^1_{ij} = \frac{\mu}{Re}\frac{\partial u_i}{\partial x_j}$ and $\sigma^2_{ij} = \frac{\mu}{Re}\left(\frac{\partial u_j}{\partial x_i} - \frac{2}{3}\frac{\partial u_k}{\partial x_k}\delta_{ij}\right)$. σ^2_{ij} can be interpreted as a "compressible" contribution, since it vanishes in the incompressible limit. The "incompressible" component σ^1_{ij} is computed by

$$\frac{1}{V_{\text{cv}}}\sum_{\text{faces}}\left(\frac{\mu}{Re}\right)_f \left.\frac{\partial u_i}{\partial x_j}\right|_f n_j A_f = \frac{1}{V_{\text{cv}}}\sum_{\text{faces}}\left(\frac{\mu}{Re}\right)_f \left.\frac{\partial u_i}{\partial n}\right|_f A_f. \tag{2.18}$$

Here, the normal gradient at the face is computed by

$$\frac{\partial\phi}{\partial n} = \frac{\phi_{ifn2} - \phi_{ifn1}}{d_f}, \tag{2.19}$$

where $ifn1$ ($ifn2$) is the projection of $icv1$ ($icv2$) onto the extension of normal vector $\mathbf{n}$ and d_f is the distance between $ifn1$ and $ifn2$ as illustrated in Figure 2.3(b). ϕ_{ifn1} is given by

$$\phi_{ifn1} = \phi_{icv1} + \nabla\phi|_{icv1} \cdot (\mathbf{x}_{ifn1} - \mathbf{x}_{icv1}), \tag{2.20}$$

where the linear least-square method is used to determine the gradient $\nabla\phi$ at $icv1$. Viscosity at the cell face is obtained using equation (2.17) and a least square reconstruction. Thus, the incompressible part corresponds to a compact–stencil method. $\sigma^2_{ij,f}$ is constructed by the interpolation of $\left.\sigma^2_{ij}\right|_{icv1}$ and $\left.\sigma^2_{ij}\right|_{icv2}$ using equation (2.17).

Once the fluxes are obtained, the predicted variables are computed using an explicit Adams–Bashfort time integration:

$$\widetilde{q}^{n+1}_j = q^n_j + \frac{\Delta t}{2}\left[3\text{rhs}_j(\mathbf{q}^n) - \text{rhs}_j(\mathbf{q}^{n-1})\right], \tag{2.21}$$

where rhs_j denotes j^{th} component of the righ–hand side of the governing equation, and the superscript n denotes the n^{th} time step.

Corrector step

As previously mentioned, the predictor step uses a non–dissipative scheme. Thus, it is unable to capture shocks and material discotinuities. The corrector step adds dissipation and it is based on the characteristic based filtering method developed by Yee et al. [96] for ideal gases on structured grids, which was extended to ideal gases on unstructured grids by Park and Mahesh [95] and later also extended for a water–vapor mixture by Gnanaskandan and Mahesh [1]. The corrector step is used to compute the final solution q_j^{n+1} from the predicted value $\widehat{q}_j^{n+1}$ as

$$q_{cv}^{n+1} = \widehat{q}_{cv}^{n+1} - \frac{\Delta t}{V_{cv}} \sum_{\text{faces}} (F_f^*.n_f) A_f, \tag{2.22}$$

where F_f^* is the filter numerical flux of the following form

$$F_{fc}^* = \frac{1}{2} R_{fc} \Phi_{fc}^*. \tag{2.23}$$

Here R_{f_c} is the matrix of right eigenvectors at the face computed using the Roe average of the variables from left and right cell–centered values. The variable $\mathbf{\Phi_{fc}^*}$ is a vector, the lth component of which, ϕ^{*l}, is given by

$$\phi_{fc}^{*l} = k \theta_{fc}^l \phi_{fc}^l, \tag{2.24}$$

where k is an adjustable parameter and θ_{fc} is Harten's switch function, given by

$$\begin{aligned} \theta_{fc} &= \sqrt{0.5(\widehat{\theta}_{icv1}^2 + \widehat{\theta}_{icv2}^2)}, \\ \widehat{\theta}_{icv1} &= \frac{|\beta_{fc}| - |\beta_{f1}|}{|\beta_{fc}| + |\beta_{f1}|}, \\ \widehat{\theta}_{icv2} &= \frac{|\beta_{f2}| - |\beta_{fc}|}{|\beta_{f2}| + |\beta_{fc}|}. \end{aligned} \tag{2.25}$$

Here, $\beta_f = R_f^{-1}(q_{icv2} - q_{icv1})$ is the difference between characteristic variables across the face. f_1 and f_2 in a structured grid are the face neighbors in the corresponding

direction (i.e. in the direction of the face normal). This definition is not possible in an unstructured grid, hence the concept of most parallel faces was introduced in Park and Mahesh [95]. Figure 2.3(a) illustrates this concept. For ϕ^ℓ, the Harten–Yee total variation diminishing (TVD) form for unstructured grids is used as suggested by Park and Mahesh [95].

$$\begin{aligned} \phi^\ell_{f_c} &= \Psi\left(a^\ell_{f_c}\right) g^{+\ell}_{f_c} - \Psi\left(a^\ell_{f_c} + \gamma^\ell_{f_c}\right) \beta^\ell_{f_c}, \\ \gamma^\ell_{f_c} &= \frac{\Psi\left(a^\ell_{f_c}\right) g^{-\ell}_{f_c} \beta^\ell_{f_c}}{\left(\beta^\ell_{f_c}\right)^2 + \epsilon}, \end{aligned} \tag{2.26}$$

where $\epsilon = 10^{-7}$, $\Psi(z) = \sqrt{\delta + z^2}$ (δ being 1/16) is introduced for entropy fixing and a^l_{fc} is an eigenvalue of the Jacobian matrix. The limiter function g_{fc} is computed using the minmod limiter as described by Park and Mahesh [95] on unstructured grids.

$$\begin{aligned} g^{+\ell}_{f_c} &\equiv \frac{1}{2}\left\{\text{minmod}\left(\beta^\ell_{f_1}, \beta^\ell_{f_c}\right) + \text{minmod}\left(\beta^\ell_{f_c}, \beta^\ell_{f_2}\right)\right\}, \\ g^{-\ell}_{f_c} &\equiv \frac{1}{2}\left\{\text{minmod}\left(\beta^\ell_{f_2}, \beta^\ell_{f_c}\right) - \text{minmod}\left(\beta^\ell_{f_1}, \beta^\ell_{f_c}\right)\right\}. \end{aligned} \tag{2.27}$$

In order to determine the eigenvectors of the system, the flux Jacobian matrix needs to be computed. First the expression for pressure needs to be expressed in terms of solution variables $q_j = (\rho, \rho u, \rho v, \rho w, \rho E_T, \rho Y_v, \rho Y_g)$. Note that total energy ($E_T = \rho e_s + \frac{1}{2}\rho u_k u_k$) is used here even though internal energy is solved in the predictor step, since jump conditions need to be obtained for conservative variables. Combining equations

(2.4) and (2.5), a quadratic equation $ap^2 + bp + c = 0$ is obtained, where

$$\begin{aligned} a &= C_{vl}(q_1 - q_6 - q_7) + C_{vv}q_6 + C_{vg}q_7, \\ b &= C_{pl}P_c(q_1 - q_6 - q_7) + (C_{vv}q_6 + C_{vg}q_7)P_c - \\ &\quad [(q_1 - q_6 - q_7)K_l + q_6R_v + q_7R_g]\left[q_5 - 0.5\frac{{q_2}^2 + {q_3}^2 + {q_4}^2}{q_1}\right] \text{ and} \\ c &= -(q_6R_v + q_7R_g)P_c\left[q_5 - 0.5\frac{{q_2}^2 + {q_3}^2 + {q_4}^2}{q_1}\right]. \end{aligned} \tag{2.28}$$

$\frac{\partial p}{\partial q_j}$ is then obtained as

$$\frac{\partial p}{\partial q_j} = -\frac{\left[p^2\frac{\partial a}{\partial q_j} + p\frac{\partial b}{\partial q_j} + \frac{\partial c}{\partial q_j}\right]}{2ap + b}. \tag{2.29}$$

The flux Jacobian matrix thus obtained, denoted by A_{ij} is given in Appendix A. Once the flux Jacobian matrix is obtained, the eigenvector matrix R_{ij} and its inverse R_{ij}^{-1}, given in Appendix, A can be evaluated.

Park and Mahesh [95] showed that for a single phase flow, the original Harten's switch (θ_{fc}) proposed by Yee et al. [96] is excessively dissipative. They proposed a modification to Harten's switch to accurately represent under–resolved turbulence for single–phase flows by multiplying θ_{fc} by a localization term based on divergence and vorticity based on the work of Ducros et al. [97] as

$$\begin{aligned} \theta_{fc} &= \theta_{fc}\theta^*_{fc}, \\ \theta^*_{fc} &= \frac{1}{2}(\theta^*_{icv1} + \theta^*_{icv2}), \\ \theta^*_{icv1} &= \frac{(\nabla \cdot \mathbf{u})^2_{icv1}}{(\nabla \cdot \mathbf{u})^2_{icv1} + \Omega^2_{icv1} + \epsilon}. \end{aligned} \tag{2.30}$$

Here Ω is the vorticity magnitude and $\epsilon = 10^{-7}$ is a small positive value. The modified term, henceforth called as modified single–phase switch, limits dissipation away from discontinuities. Gnanaskandan and Mahesh [1] modified it for the multiphase mixture of

water and vapor to avoid the non–monotonic behavior in the regions of flow cavitation as the single–phase switch, equation (2.30), reaches extremely small values due to high vorticity. This is given by

$$\theta^*_{fc} = \frac{1}{2}(\theta^*_{icv1} + \theta^*_{icv2}) + |(\alpha_{v_{icv2}} - \alpha_{v_{icv1}})|. \tag{2.31}$$

While the modification proposed by Gnanaskandan and Mahesh [1] works well for water–vapor mixture, it still does not prevent the non–monotonic behavior when NCG is present. We illustrate this by considering a cavitating inviscid vortex. We consider a square domain of size $10R \times 10R$. The flow is initialized with the following velocity field:

$$\begin{aligned} u &= -\frac{C(y - y_c)}{R^2} exp(\frac{-r^2}{2}) \quad \text{and} \\ v &= \frac{C(x - x_c)}{R^2} exp(\frac{-r^2}{2}), \end{aligned} \tag{2.32}$$

where $r = \sqrt{(x - x_c)^2 + (y - y_c)^2}/R$, $R = 1.0$, $C = 5.0$ and $x_c = y_c = 5R$. As we march in time, pressure inside the vortex core drops leading to flow cavitation and NCG expansion. When the modifications of equations (2.30) and (2.31) are used, we see non–monotonic behavior in the solution as illustrated by the flow velocity divergence in figures 2.4(a) and (b). As a remedy, an additional term due to the NCG volume fraction is added to the multiphase switch as

$$\theta^*_{fc} = \frac{1}{2}(\theta^*_{icv1} + \theta^*_{icv2}) + |(\alpha_{v_{icv2}} - \alpha_{v_{icv1}})| + |(\alpha_{g_{icv2}} - \alpha_{g_{icv1}})|. \tag{2.33}$$

This additional term prevents non–monotonic behavior due to the expansion of NCG in the low pressure regions as shown in the figure 2.4(c). This can be better visualized in figure 2.5, that shows profiles of the velocity divergence across the vortex. It is evident that the solution does not present overshoots with the use of equation (2.33). Hence, θ_{fc} as defined by equation (2.33) is used for the computation of θ^l_{fc} in equation (2.24).

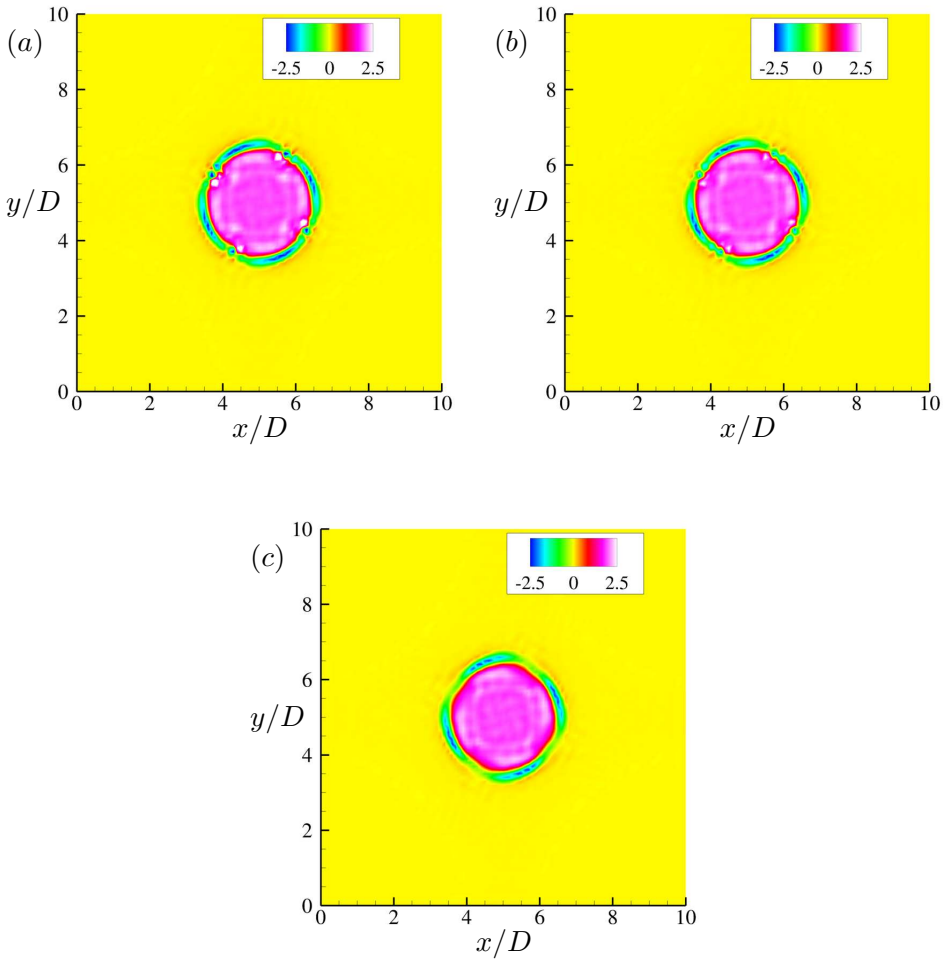

Figure 2.4: Velocity divergence contours using different modifications to the Harten's switch: equation (2.30) (a), equation (2.31) (b) and equation (2.33) (c).

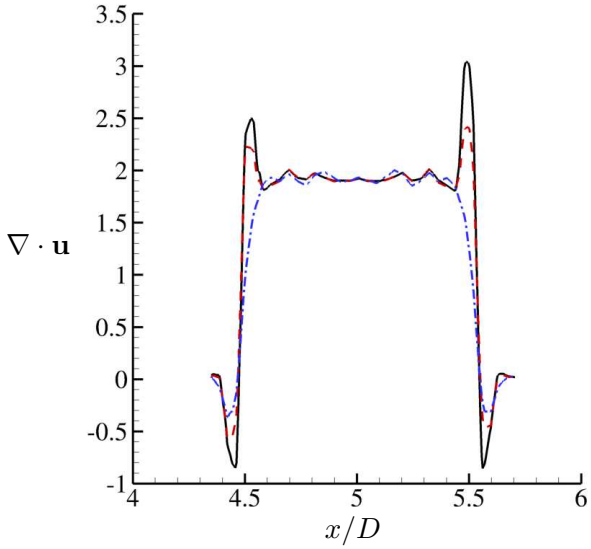

Figure 2.5: Velocity divergence profiles across the vortex using different modifications to the Harten's switch: equation (2.30) (——), equation (2.31) (----) and equation (2.33) (–· –·).

2.1.3 Validation

The base numerical method for a water–vapor mixture has been validated in Gnanaskandan and Mahesh [1] for a wide range of problems. This section presents a validation for the extensions added to the governing equations and numerical method, and evaluates the accuracy of the shock capturing scheme in computing the jump conditions for two problems.

The first problem involves a one dimensional tube consisting of water and a small amount of vapor. The initial conditions are given by

$$\begin{aligned} Q(x,0) &= \begin{cases} Q_L, & \text{x/L} < 0.5 \\ Q_R, & \text{x/L} \geq 0.5 \end{cases} \\ Q &= [\alpha_v, u, p], \\ Q_L &= [0.1, -100.0, 1.0 \times 10^5], \\ Q_R &= [0.1, 100.0, 1.0 \times 10^5]. \end{aligned} \tag{2.34}$$

The computational domain is discretized uniformly using 1000 volumes and a time step of 1×10^{-6}s is used. A low pressure region is created at the center of the domain as the two streams flow in opposite directions. This causes a vapor bubble to be produced as soon as the pressure reaches vapor pressure. Two interfaces are created dynamically due to the rarefaction waves, as a result. The mixture pressure, velocity and vapor volume fraction at a given instant of time are given in figure 2.6 where they are compared to the results obtained using a multi–fluid approach by Saurel and Lemetayer [98]. It can be seen that a very good agreement is obtained.

In the second problem, a single–phase one dimensional tube contains two different ideal gases at two different pressures. This problem has been previously investigated by many authors [99–101] when developing first and second order numerical schemes. The initial condition is given by

$$\begin{aligned} Q(x,0) &= \begin{cases} Q_L, & \text{x/L} < 0.5 \\ Q_R, & \text{x/L} \geq 0.5 \end{cases} \\ Q &= [\rho, u, p, \gamma, Y_1, Y_2], \\ Q_L &= [1.0, 0.0, 1.0, 1.4, 1.0, 0.0], \\ Q_R &= [0.125, 0.0, 0.1, 1.2, 0.0, 1.0]. \end{aligned} \tag{2.35}$$

This problem is stiffer than the previous one; the density and pressure differ by $O(1)$ across the discontinuities. As a result of this pressure difference, a shock wave and a rarefaction wave are released as soon as the solution advances in time. The computational domain is again discretized uniformly using 1000 volumes. The mixture pressure, density and velocity are compared against the data from Chargy et al. [99] in figure 2.7, where good agreement is obtained.

2.2 Inception regime

Most LES of cavitation has been applied to attached or sheet–to–cloud regimes using compressible formulations of the homogeneous mixture equations. The inception

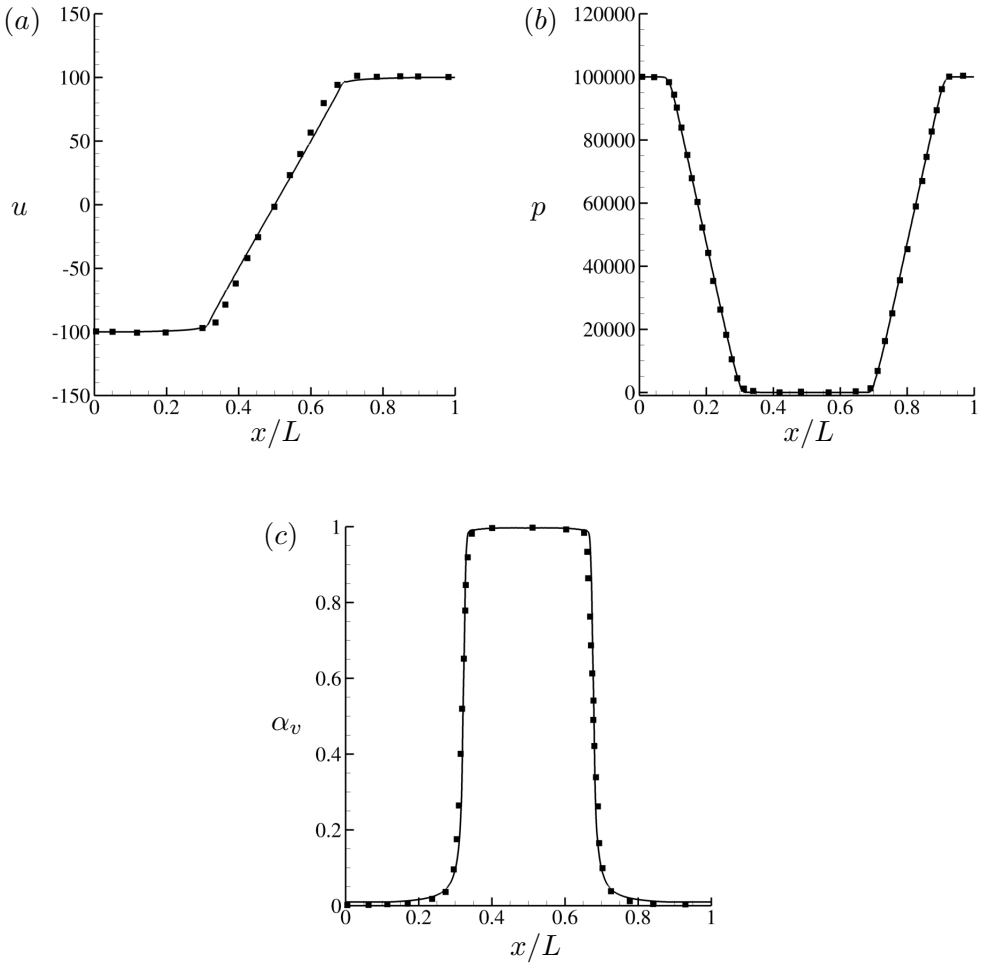

Figure 2.6: Comparison of present numerical results (——) with data available in Saurel and Lemetayer [98] (■) for velocity (a), pressure (b) and vapor void fraction (c).

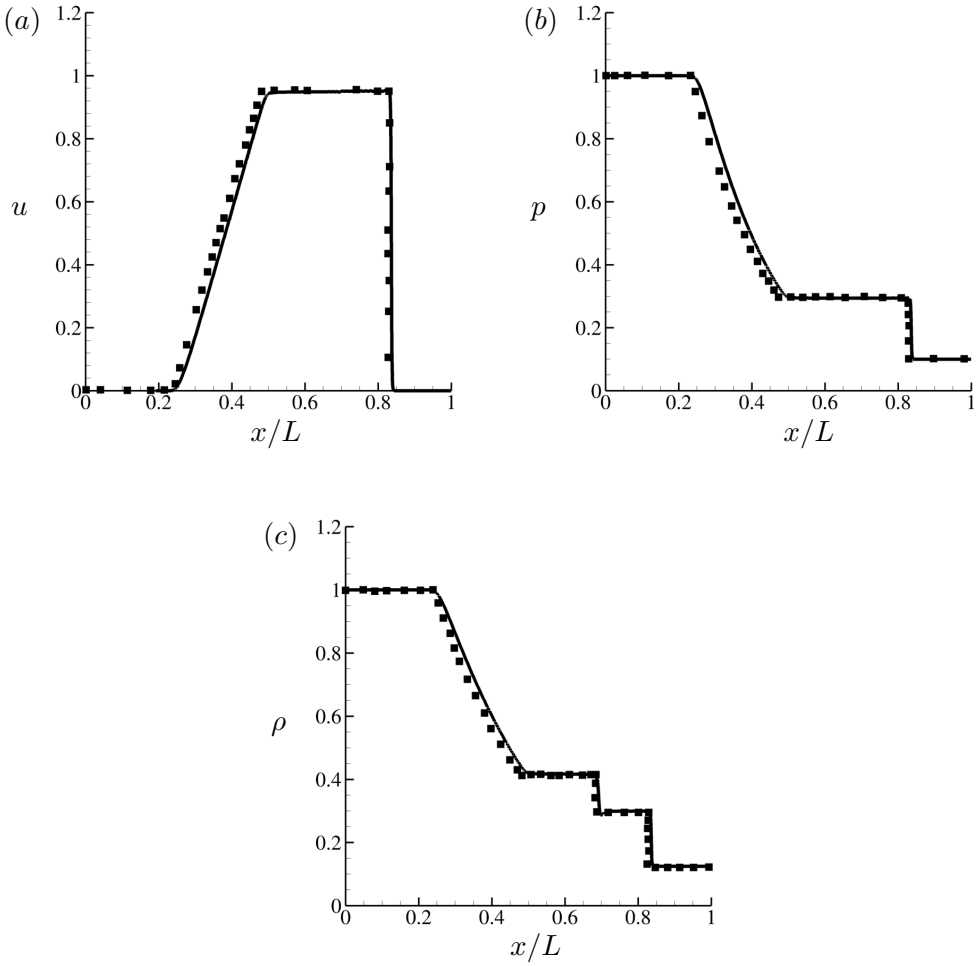

Figure 2.7: Comparison of present numerical results (——) with data available in Chargy et al. [99] (■) for velocity (a), pressure (b) and mixture density (c).

regime has received less attention in numerical simulations, despite being important for practical applications. Inception occurs in the regime of low void fractions where the compressible governing equations can be argued to reduce to the zero–Mach equations which imply the use of the incompressible governing equations along with the same vapor volume fraction transport equation as the compressible formulation. Here, we propose a different approach. The main idea is that since inception is a stochastic process that generates small amounts of vapor for short periods, the effects of these small regions of vapor on the liquid density and dynamics can be neglected. Therefore, here vapor is treated as a passive scalar in the incompressible liquid. Different time steps are used for time advancement of the vapor and velocity fields; the transport equation for the vapor is solved in an inner loop at a smaller time step than that employed for the momentum equation. This is because scalar fronts are thinner than velocity fronts since they do not have pressure to regulate their thickness. An unsteady sharp front implies higher frequencies and therefore smaller timestep. In addition, special attention is paid to the treatment of the source terms to avoid unbounded solutions.

2.2.1 Governing equations

The filtered Navier–Stokes equations are

$$\begin{aligned} \frac{\partial \bar{u}_i}{\partial x_i} &= 0 \\ \frac{\partial \bar{u}_i}{\partial t} + \frac{\partial \bar{u}_i \bar{u}_j}{\partial x_j} &= -\frac{\partial \bar{p}}{\partial x_i} + \nu \frac{\partial^2 \bar{u}_i}{\partial x_j \partial x_j} - \frac{\partial \tau_{ij}}{\partial x_j}, \end{aligned} \tag{2.36}$$

where $\tau_{ij} = \overline{u_i u_j} - \bar{u}_i \bar{u}_j$ is the sub-grid scale (SGS) stress and is modeled using the dynamic Smagorinsky eddy–viscosity model [102]. The filtered transport equation for

the vapor is given by:

$$\begin{aligned}
\frac{\partial \bar{C}}{\partial t} + \frac{\partial \bar{C}\bar{u_j}}{\partial x_j} - \frac{\nu}{Sc}\frac{\partial^2 \bar{C}}{\partial x_j x_j} + \frac{\partial \tau_s}{\partial x_j} &= \bar{S_e} - \bar{S_c} \\
\bar{S_e} &= C_e \bar{\alpha}^2 (1-\bar{\alpha})^2 \frac{\rho_l}{\rho_v} \frac{max(p_v - \bar{p}, 0)}{\sqrt{2\pi R_v T}} \\
\bar{S_c} &= C_c \bar{\alpha}^2 (1-\bar{\alpha})^2 \frac{max(\bar{p} - p_v, 0)}{\sqrt{2\pi R_v T}}.
\end{aligned} \tag{2.37}$$

Here, the passive scalar is considered as the concentration of vapor, $C = \rho_v \alpha$, $\overline{()}$ denotes spatial filtering at the filter width Δ. The Schmidt number for vapor in water is $Sc = 500$. The vapor volume fraction is indicated by α and ρ_v is the vapor density, which is assumed constant. For the SGS scalar flux, $\tau_s = \overline{Cu_j} - \bar{C}\bar{u_j}$, the dynamic Smagorinsky eddy–diffusivity model [103] is employed. It can be seen from equation (2.37) that the source term is again taken from Saito et al. [41]. Similarly from section 2.1, the vapor pressure is taken as equation (2.10).

2.2.2 Numerical methods

If equation (2.37) is written in non–dimensional form, the diffusive term becomes $\frac{1}{ReSc}\frac{\partial^2 \tilde{C}}{\partial \tilde{x_j} \tilde{x_j}}$, where the tilde symbol ($\tilde{}$) indicates non–dimensional units. This reveals that the diffusion term for the vapor concentration is very small, even for cases at a relatively small Re, and is not enough to smoothen the sharp gradients that may arise in the solution. Thus, the scalar field requires a smaller time step than the velocity field. Therefore, in this work we use an algorithm based on the work of Muppidi and Mahesh [104] for passive scalar in jets and is outlined as follows: The incompressible Navier–Stokes equations are solved using a predictor–corrector algorithm developed in Mahesh et al. [78] with Crank–Nicolson scheme for implicit time advancement. After the velocity and pressure fields are obtained at the new time instance $t^{n+1} = t^n + \Delta t_m$, the passive scalar equation is solved in an inner loop with m smaller time steps using $\Delta t_s = \Delta t_m / m$. The velocity and pressure field at the previous (t^n) and new time instances (t^{n+1}) are interpolated to obtain the convective and diffusive fluxes, as well as the source term at the inner time instance. For the time advancement of the scalar equation, we use

the implicit Crank–Nicolson scheme, while the convective fluxes are computed using an upwind discretization. It is relevant to mention that lowering the time step for both scalar and velocity fields would make the simulation more computationally expensive, since the time advancement of the velocity field involves a predictor–corrector method. When our method is compared against the existing numerical approaches for cavitation inception, decoupling the time step used for the scalar field from the one used for the velocity field offers the clear advantage of reducing computational costs. The algorithm can be summarized as follows.

- Advance u^n and p^n to u^{n+1} and p^{n+1}
  - Use u^n and p^n to advance C^n to $C^{n,1}$
    1. Interpolate: $u^{n,1} = u^n + \frac{u^{n+1}-u^n}{\Delta t_m}\Delta t_s$
    2. Interpolate: $p^{n,1} = p^n + \frac{p^{n+1}-p^n}{\Delta t_m}\Delta t_s$
  - Use $u^{n,1}$ and $p^{n,1}$ to advance $C^{n,1}$ to $C^{n,2}$
    1. Interpolate: $u^{n,2} = u^{n,1} + \frac{u^{n+1}-u^n}{\Delta t_m}\Delta t_s$
    2. Interpolate: $p^{n,2} = p^{n,1} + \frac{p^{n+1}-p^n}{\Delta t_m}\Delta t_s$

    $\vdots$
  - Use $u^{n,m-1}$ and $p^{n,m-1}$ to advance $C^{n,m-1}$ to C^{n+1}
- Advance u^{n+1} and p^{n+1} to u^{n+2} and p^{n+2}.

The unfiltered version of equation (2.37) can be written in the discrete form as

$$V_{cv}\left(\frac{\partial C}{\partial t}\right)_{cv} + \sum_f \left(CV_n\right)_f A_f - \frac{\nu}{Sc}\sum_f \left(\frac{\partial C}{\partial n}\right)_f A_f = V_{cv}\left(S_e - S_c\right), \tag{2.38}$$

where V_{cv} and A_f represent the volume of a mesh element and the area of a face, respectively. The fluid velocity at a face center and in a direction normal to it is indicated by V_n. To solve equation (2.38), the values of the scalar flux across a face, $(CV_n)_f$, and the face–normal derivative, $\left(\frac{\partial C}{\partial n}\right)_f$, are required. Consider a uniform and

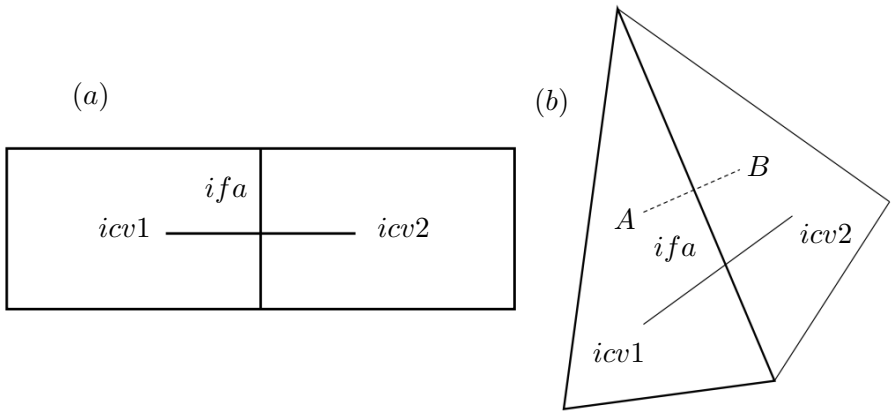

Figure 2.8: Examples of a mesh element. An internal face is indicated by ifa and the control volumes adjacent to it are given by $icv1$ and $icv2$.

structured mesh element, as displayed in figure 2.8(a), where the fluid is moving from $icv1$ to $icv2$. The convective flux at ifa, in an upwind discretization, is computed as

$$(CV_n)_{ifa} = C_{icv1} V_n, \tag{2.39}$$

and the face–normal derivative can be computed as

$$\left(\frac{\partial C}{\partial n}\right)_{ifa} = \frac{C_{icv2} - C_{icv1}}{d_{icv}}, \tag{2.40}$$

where d_{icv} is the distance along the solid line connecting $icv1$ and $icv2$ centroids. Consider now a skewed mesh element as shown in figure 2.8(b). It is noted that the line connecting the centroids of the control volumes adjacent to ifa does not pass through the face center and is at an angle with the face normal. Equations (2.39) and (2.40) become inaccurate in cases like this. Observe now the points A and B in figure 2.8(b). They are connected by a dashed line that is orthogonal to ifa and passes through the face center. Accurate computation of the fluxes requires obtaining the value of C at these points (C_A, C_B). A reconstruction scheme based on least–squares is used for this purpose [104], as follows: Given the coordinates of the face center ($x_{i,ifa}$) and the face normal, the coordinate of any point along the face normal (dashed line) can be

computed as

$$x_i = l_i r + x_{i,ifa}, \tag{2.41}$$

where l_i is the directional cosine of the face normal and r is a length variable. Let r_A be the value of r that minimizes the distance between A and $icv1$ centroid in a least–square sense (e.g. $(x_{i,A} - x_{i,icv1})^2$), and r_B be the value of r that minimizes the distance between B and $icv2$ centroid, also in a least–square sense. The final value for r is the one that minimizes both as $r = min[r_A, r_B]$. With the locations of points A and B in hand, C_A, C_B and the fluxes can be computed as

$$\begin{aligned} C_A &= C_{icv1} + (\nabla C)_{icv1}(x_{i,A} - x_{i,icv1}), \\ (CV_n)_{ifa} &= C_A V_n, \\ \left(\frac{\partial C}{\partial n}\right)_{ifa} &= \frac{C_B - C_A}{d_{AB}}, \end{aligned} \tag{2.42}$$

where d_{AB} is the distance between points A and B.

Treatment of source terms

The source terms can have a big impact on the reliability of numerical solutions as they can drive them to unphysical values. In our case, these unrealistic solutions are $\alpha > 1$ and $\alpha < 0$. Usually, the source terms are better handled explicitly when they are positive, and implicitly when they are negative (sink) [105, 106]. For cavitation problems, we have both cases (see equation (2.37)). In the present work, they are treated as suggested in the work of Lian et al. [106], where the source ($\bar{S}_e$) is divided between an equivalent sink and an enhanced source. We write the unfiltered version of the RHS of equation (2.37) in a generalized Crank–Nicolson form as

$$\begin{aligned} ... = &- \psi(\theta_1 S_e^{n+1} + (1-\theta_1) S_e^n) + (1+\psi)(\theta_2 S_e^{n+1} + (1-\theta_2) S_e^n) \\ &- (\theta_3 S_c^{n+1} + (1-\theta_3) S_c^n), \end{aligned} \tag{2.43}$$

where the parameters θ_1, θ_2 and θ_3 can take the values of 0, 0.5 or 1 indicating explicit, Crank–Nicolson or implicit formulation, respectively. The first, second and third terms in the RHS of equation (2.43) are the equivalent sink, the enhanced source and the original sink, respectively. Due to the non–linear nature of both source and sink terms, they are linearized following a Taylor series expansion with respect to the vapor concentration as

$$\begin{aligned} S_e^{n+1} &= S_e^n + \frac{\partial S_e}{\partial C}^n (C^{n+1} - C^n), \\ S_c^{n+1} &= S_c^n + \frac{\partial S_c}{\partial C}^n (C^{n+1} - C^n). \end{aligned} \tag{2.44}$$

Since $\alpha = C/\rho_v$, the partial derivatives of evaporation and condensation source terms are given by

$$\begin{aligned} \frac{\partial S_e}{\partial C} &= 2C(1 - 3\frac{C}{\rho_v} + 2\frac{C^2}{\rho_v^2})\frac{\rho_l}{\rho_v^3} C_e \frac{max(p_v - p, 0)}{\sqrt{2\pi R_v T}}, \\ \frac{\partial S_c}{\partial C} &= 2C(1 - 3\frac{C}{\rho_v} + 2\frac{C^2}{\rho_v^2})\frac{1}{\rho_v^2} C_c \frac{max(p - p_v, 0)}{\sqrt{2\pi R_v T}}. \end{aligned} \tag{2.45}$$

It was recommended in Lian et al. [106] that both the original and equivalent sink should be treated implicitly ($\theta_1 = \theta_3 = 1$) while the enhanced source should be treated explicitly ($\theta_2 = 0$) with $\psi = 1$. This choice of parameters was shown to provide stable results when employed with a linear source term in Lian et al. [106]. However, the cavitation source and sink terms employed in this work are biquadratic. Although $\theta_3 = 1$ works well for the sink, we will show that the values for θ_1 and θ_2 need to be adjusted.

When $p < p_v$, only the source is activated and, ignoring the convective and diffusive fluxes, the change in vapor concentration during one time step (Δt_s) is given by

$$\Delta C = C^{n+1} - C^n = \frac{\Delta t_s S_e}{1 + \frac{\partial S_e}{\partial C}\Delta t_s(\psi\theta_1 - (1+\psi)\theta_2)}. \tag{2.46}$$

Figure 2.9 presents how the solution changes for different values of $\Delta t_s/t_r$ (where t_r is a given reference time), and for a given value of pressure, when the parameters are chosen to be the same as suggested by Lian et al. [106]: $\psi = 1$, $\theta_1 = 1$ and $\theta_2 = 0$.

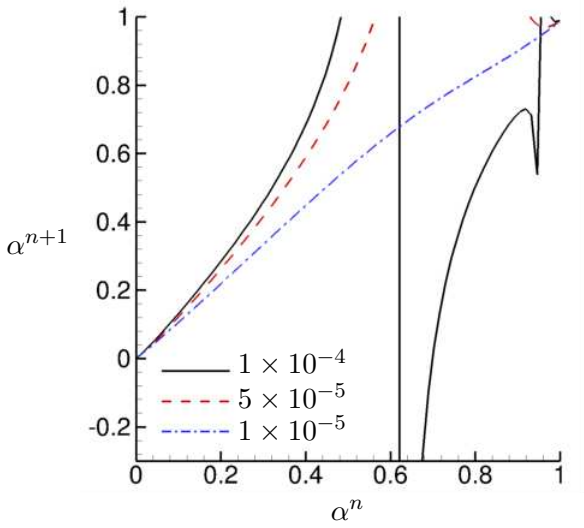

Figure 2.9: Change in solution for different scalar time steps.

Here, we have used a very large value for the empirical constant, $C_e = 200m^{-1}$, to create a substantial growth of vapor concentration. Figure 2.9 reveals that, even when applying implicit time advancement for the transport equation, we need a time step as small as $\Delta t_s/t_r = 1 \times 10^{-5}$ for the vapor volume fraction to remain bounded in the {0,1} range. Figure 2.10 shows the change in the void fraction at $\Delta t_s/t_r = 5 \times 10^{-5}$ for different combinations of the parameters ψ, θ_1 and θ_2. The first observation that can be made from figure 2.10 is that the proper choice of parameters allow the solution to remain bounded even for higher time steps. It can be seen that when treating the enhanced source explicitly ($\theta_2 = 0$) as suggested in Lian et al. [106], values of α within the range of {0,1} are only achieved when the equivalent sink is also treated explicitly ($\theta_1 = 0$). We can see that three combinations of parameters provide limited cavitation: $\theta_1 = \theta_2 = 0$, $\theta_1 = \theta_2 = 0.5$ and $\theta_1 = 1$ with $\theta_2 = 0.5$.

A question remains of why these combinations work and why their α^{n+1} curves have different slopes. A logical way to study this would be through von Neumann stability analysis. However, due to the non–linear nature of the source term, this task becomes unnecessarily hard. Consequently, we follow the approach in Patankar [107]. Applying equation (2.44) into the RHS of equation (2.43), the linearized evaporation source term

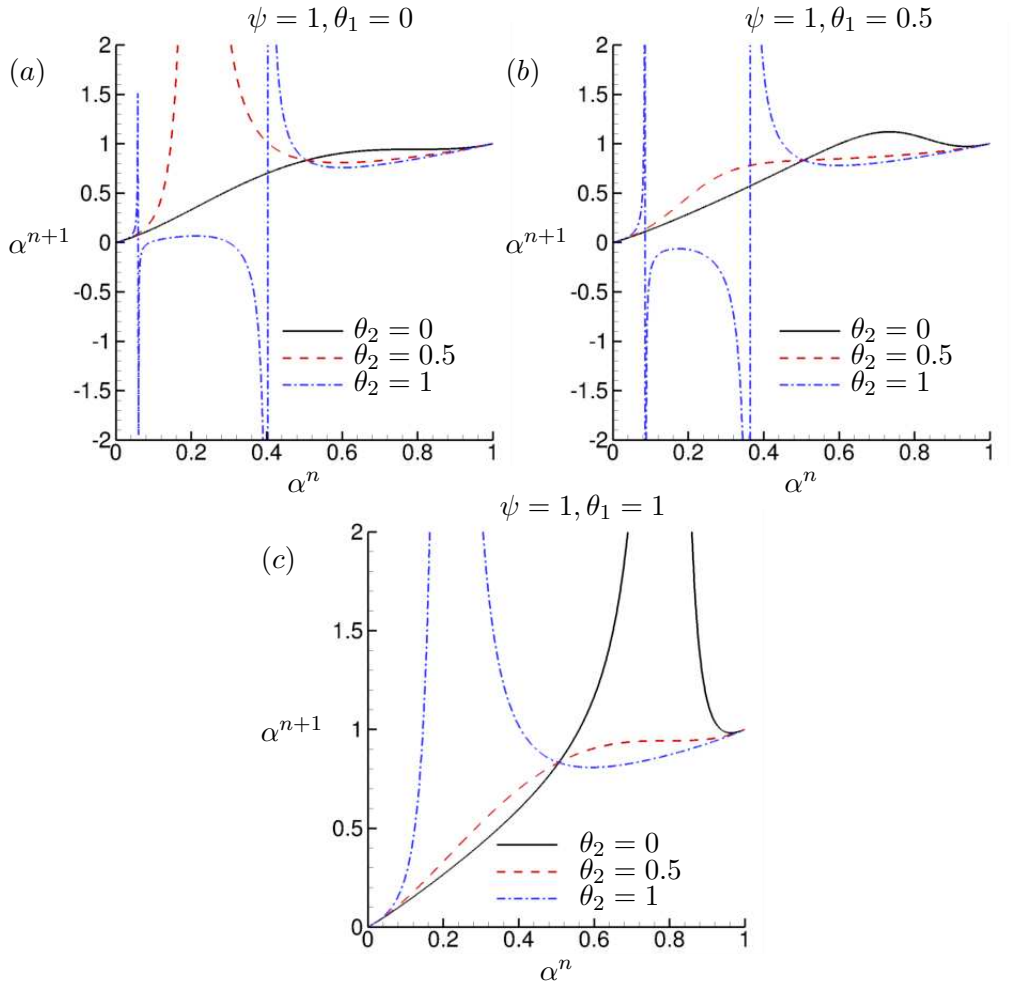

Figure 2.10: Change in solution for different choice of the parameters ψ, θ_1, θ_2 for $\Delta t_s/t_r = 5 \times 10^{-5}$.

becomes

$$\begin{aligned} S_{el} &= S_{ec} + S_{ep} C^{n+1}, \\ S_{ec} &= S_e^n - (-\psi\theta_1 + (1+\psi)\theta_2)\frac{\partial S_e}{\partial C}^n C^n, \\ S_{ep} &= (-\psi\theta_1 + (1+\psi)\theta_2)\frac{\partial S_e}{\partial C}^n . \end{aligned} \tag{2.47}$$

Equation (2.47) reveals that the different choices of parameters will result in distinctive slopes for S_{el}, which is plotted in figure 2.11. The source term of Saito et al. [41] has a region where $\frac{\partial S_e}{\partial C} > 0$ and another where $\frac{\partial S_e}{\partial C} < 0$ with the transition between them located at $\alpha = 0.5$. Therefore, in figure 2.11 we show lines of S_{el} for values of C^n at these two different regions. A line with zero slope (horizontal) indicates that the solution is growing at a constant rate while lines with positive and negative slope mean an accelerated and decelerated solution change, respectively. The steeper the S_{el} line is, the faster the solution changes. If the time step is not small enough, combinations of the parameters that result in steeper S_{el} lines will lead to an unrealistic solution. This becomes clear when comparing figure 2.11(a) with figure 2.10(a) for $\psi = 1$ and $\theta_1 = 0$. Here we can see that increasing θ_2 from 0 to 1 makes the S_{el} line steeper and the only bounded solution occurs when $\theta_2 = 0$, which has zero slope. When $\theta_2 = 0.5$, the S_{el} line is a bit steeper than the S_e curve, leading to a solution of $\alpha^{n+1} > 1$ in figure 2.10(a). When $\theta_2 = 1$, the S_{el} line becomes steeper and the solution blows–up even earlier. A combination of parameters that results in S_{el} lines with negative slopes are also preferable and recommended in Patankar [107] since they imply a decelerated solution growth that allows for higher time steps. However, we can see in figure 2.11 that no combination yields negative slopes in both regions of the S_e curve. Thus, we can see that the safer choices of parameters are $\theta_1 = \theta_2 = 0$, $\theta_1 = \theta_2 = 0.5$ and $\theta_1 = 1$ with $\theta_2 = 0.5$, which are the exact combinations that generated restricted solutions in figure 2.10.

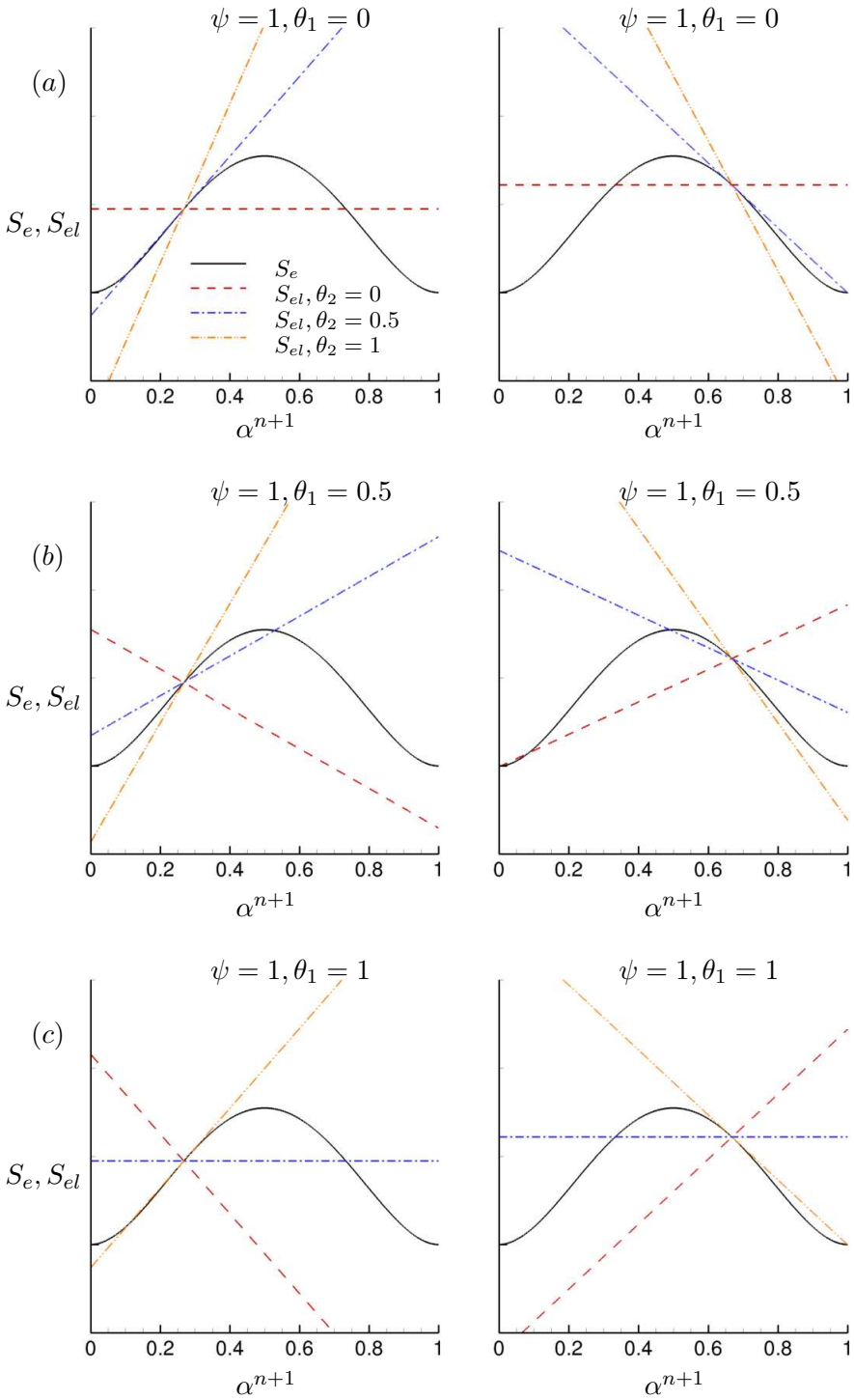

Figure 2.11: Comparison between the source term and its linearization. The plots on the left are for a specific C^n in the region where $\frac{\partial S_e}{\partial C} > 0$ and the plots on the right are for a specific C^n in the region where $\frac{\partial S_e}{\partial C} < 0$.

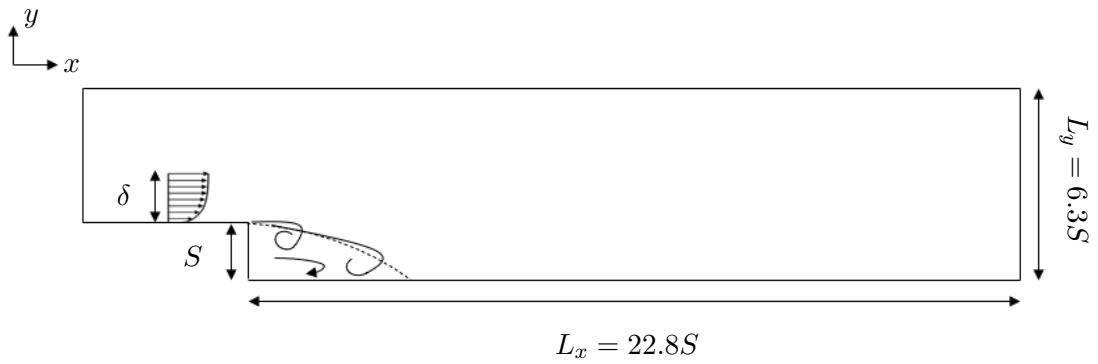

Figure 2.12: Computational domain for the backstep problem.

2.2.3 Validation

We verify that our present model, which combines the incompressible Navier–Stokes equations with a vapor transport equation, agrees with a fully compressible homogeneous mixture model under inception conditions. Towards this end, we perform simulations under inception conditions over a backstep from the work of Agarwal et al. [4] and compare to corresponding results obtained using the fully compressible homogeneous mixture model with a preconditioning methodology, to handle the acoustic stiffness, developed by Bhatt and Mahesh [20]. The domain has a step height (S) of $10mm$, an expansion ratio (ER) of 1.19 and an aspect ratio (AR) equal to 5.3. A sketch of the domain is shown in figure 2.12. The Re is taken to be 200 based on the step height and on the free–stream velocity. This small value for Re is chosen to make the solution independent of subgrid model. No–slip boundary conditions are applied to every wall in the domain and the outflow is located at 22.8 S downstream from the step corner. The very low Re used in this comparison results in a two–dimensional flow. Thus, the grid is coarsened to $\Delta x/S = 1$ and $\Delta y/S = 0.1$ with 3 points in the spanwise direction. The simulations are performed at $\sigma = 1.98$, based on the inflow pressure and velocity, with a free–stream vapor concentration equivalent to a volume fraction of $\alpha = 1 \times 10^{-6}$. It is essential to highlight that the use of a high cavitation number concurrently with a small free–stream volume fraction is necessary for such comparison due to two main

reasons. The first relates to the fact that, if σ is small to the point of forming considerable amounts of vapor, the flow can not be deemed divergence–free anymore and the passive scalar assumption fails. The second reason is that when a pocket of vapor collapses, pressure waves are released affecting the flow field, which is not captured by the incompressible Navier–Stokes.

Figure 2.13(a), (b) and (c) show profiles of $\langle u \rangle / u_\infty$, $\langle \alpha \rangle$ and $\sqrt{\langle \alpha'^2 \rangle}$, respectively, at three different locations downstream of the step. Good agreement is achieved for the mean velocity profiles, showing that the flow dynamics are unaffected by the produced vapor. Profiles of $\langle \alpha \rangle$ and $\sqrt{\langle \alpha'^2 \rangle}$ also show very good agreement, indicating that the present method is capable of capturing vapor growth under inception conditions.

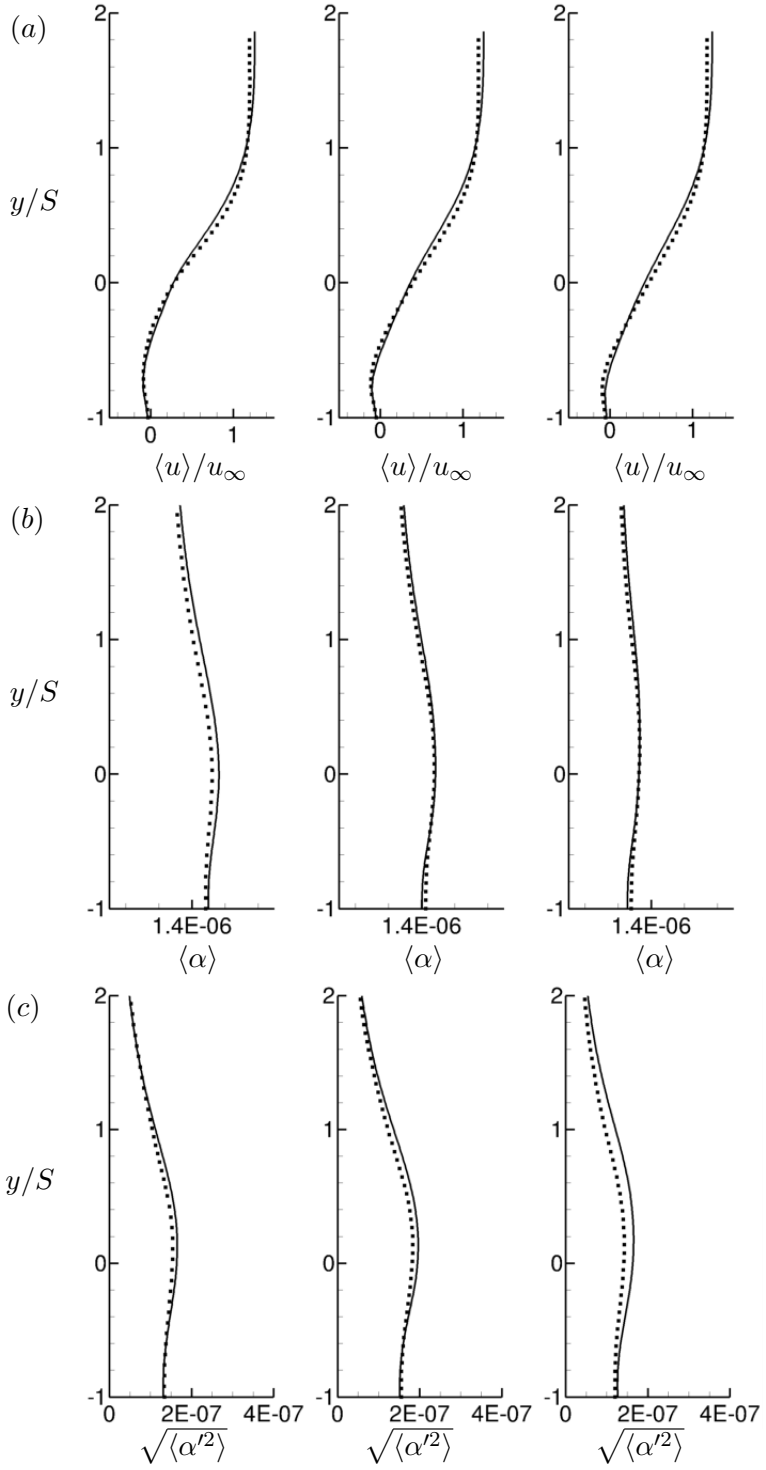

Figure 2.13: Results from present model (lines) validated against model of Bhatt and Mahesh [20] (symbols). Profiles from left to right are taken at $x = 1S$, $x = 2S$ and $x = 3S$ downstream of the step, respectively.

Chapter 3

Cavitation regimes in a flow over a circular cylinder

The objectives of this study are to (i) investigate cavitating flow over a circular cylinder over a range of σ spanning non–cavitating, cyclic and transitional cavitation regimes, (ii) discuss the changes in shedding characteristics over the regimes using numerical results and dynamic mode decomposition, (iii) using the Rankine–Hugoniot jump conditions, discuss the condensation shock propagation in the transitional regime, (iv) study the effect of NCG and free–stream nuclei content on the shedding characteristics and condensation shock propagation and (v) study turbulent cavitating flow at $Re = 3900$ and compare it to past work and laminar flow simulations at $Re = 200$.

The chapter is organized as follows. The problem setup and simulation details are provided in section 3.1. Results are discussed in section 3.2 as follows. Shedding characteristics, including a DMD analysis is presented in subsection 3.2.1, while the effects of the free–stream nuclei levels are discussed in subsection 3.2.2. The effects of the NCG on the condensation shock are explored in subsection 3.2.3, and large–eddy simulation results of the $Re = 3900$ cavitating cylinder are presented in section 3.2.4.

Cases	**Free–stream nuclei** $(\alpha_{v0}, \alpha_{g0})$	**Cavitation number** (σ)	**Reynolds number** (Re)
Case A3900	$1.0e^{-9}, 1.0e^{-6}$	$1.0, 0.7$	3900
Case A200	$1.0e^{-9}, 1.0e^{-6}$	$5.0, 1.0, 0.85, 0.75, 0.7$	200
Case B	$1.0e^{-2}, 1.0e^{-2}$	$1.5, 1.0, 0.85, 0.75, 0.7, 0.5$	200
Case C	$1.0e^{-2}, 0.0$	$1.5, 1.0, 0.85, 0.75, 0.7, 0.5$	200

Table 3.1: Cases showing flow conditions chosen for the problem.

3.1 Problem Setup

Table 3.1 lists the flow conditions considered for the simulations. The cavitation number in the free–stream is $\sigma = \frac{p_\infty - p_v}{\frac{1}{2}\rho_\infty U_\infty}$, where p_∞, ρ_∞ and U_∞ are pressure, density and velocity in the free–stream respectively. Cavitation number in the flow is varied from non–cavitating conditions to the cloud shedding regime. The Reynolds number, defined as $Re = \frac{\rho_\infty U_\infty D}{\mu}$ where D is the cylinder diameter, used here are $Re = 200$ and $Re = 3900$ as considered by Gnanaskandan and Mahesh [44] for investigation of cavitation in near wake of the cylinder for water–vapor mixture. The simulations are initialized with a spatially uniform void fraction of vapor (α_{v0}) that nucleates the cavitation. NCG (α_{g0}) is introduced in the free–stream similar to the vapor nuclei in a spatially uniform manner. Different amounts of free–stream vapor and gas volume fraction are used in this study. Details are provided in the table 3.1, with the corresponding σ and Re.

Figure 3.1 shows the schematic of the problem. The grid is 2D and 3D for the $Re = 200$ and $Re = 3900$ simulations, respectively. The domain size and mesh used in the present work is same as the finer grid and larger domain size used by Gnanaskandan and Mahesh [44]. They performed a grid refinement study and showed that time evolution of lift/drag coefficient as well as the profiles of mean and fluctuations in the void fraction show good agreement between their chosen grids. The computational domain is cylindrical with the origin at the center of the cylinder. The domain is extended radially until $100D$ and covers a distance of 2π and π in the spanwise direction for the 2D and 3D simulations respectively. The free–stream direction is in the positive x direction as

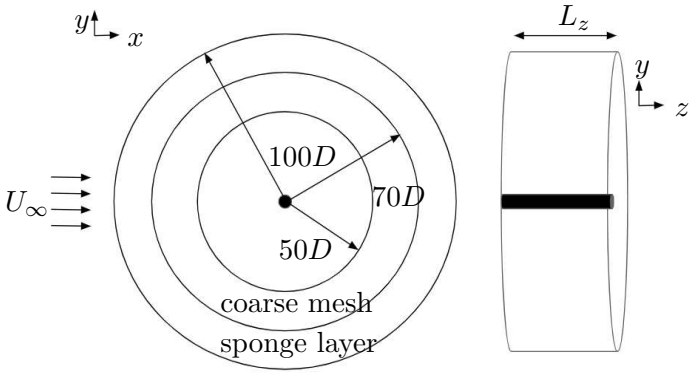

Figure 3.1: Domain illustrating sponge layer and region of coarse mesh (not to scale).

indicated by the arrows in the figure 3.1. Free–stream conditions are imposed on all the farfield boundaries. Collapse of cavitation clouds produces strong pressure waves which propagate over the entire domain. In order to avoid reflection of these pressure waves from the boundaries, we apply acoustically absorbing sponge layers at the boundaries as shown in figure 3.1. This introduces an additional term in the governing equations (2.1) given by, $\Gamma(q - q_{ref})$. Here 'q' denotes the vector of conservative variables and the subscript 'ref' denotes the reference solution to which the flow is damped to, which is free–stream values in the cases considered. 'Γ' denotes the amplitude of the forcing. In addition, the grid is coarsened in the far field to further reduce any reflections. The mesh spacing considered near the cylinder surface is $0.005D \times 0.01D$ in the radial and azimuthal directions, which stretches to $0.03D \times 0.03D$ at approximately $2D$ downstream and then further stretches to $0.07D \times 0.07D$ at a distance of $5D$ downstream. For the 3D grid required at $Re = 3900$, 80 points are used in the spanwise direction while the same resolution as the 2D grid is maintained in the xy plane.

3.2 Results

Over the range of σ studied, we observe two types of cavitation regimes as described by Fry [28]: cyclic and transitional. The cyclic cavitation regime is observed for high values of σ, which is characterised by periodic shedding of the cavitating vortices originating

at the surface and is illustrated in figure 3.2(a). These cavitating vortices collapse as they move downstream into the region of high pressure, producing pressure waves. As σ is reduced, the flow enters the transitional cavitation regime. Here, the cavity shedding process alternates between two phenomena. The first is similar to cyclic cavitation in the vortex cores; the difference however is that these vortex cores cavitate further downstream and the cavity thus formed is not attached to the cylinder. During this part of the cycle, the cylinder surface and immediate wake remain cavitation free as shown in figure 3.2(b). This is followed by the second phenomenon where the instantaneous pressure in the immediate wake drops below vapor pressure, where a cavity forms symmetrically spanning the entire aft–body of the cylinder as shown in figure 3.2(c). Then, a pressure wave generated after the collapse of a vortex core impinges on the attached cavity, condensing it as displayed in figure 3.2(c). This is called a condensation front, or condensation shock if it moves at supersonic speed. Once this front hits the cylinder, it will lead to cavity detachment.

3.2.1 Shedding characteristics

For single–phase flow over a bluff body, vortices shed periodically from the surface forming the classical primary Kármán vortex street in the near wake. This is followed by a transition in the intermediate wake to a two–layered vortex street [108]. The first vortex street transition was explained by Durgin and Karlsson [109] using a model in which a concentration of vorticity is strained into an elliptical shape by the nearby vortices in the street. This distorted vortex is then rotated, aligning its major axis with the streamwise direction. This process eventually results in distorted vortices merging and becoming shear layers on either side of the street. An important parameter that indicates the straining of the vortices and their merging is the spacing ratio, defined as the ratio between the cross–wake distance of different sign vortices to the longitudinal distance between same sign vortices. In the experiments of Durgin and Karlsson [109], the authors found a spacing ratio greater than 0.366 to be indicative of the transition, which was later confirmed by Karasudani and Funakoshi [110].

For cavitating flows, analysis of flow variables in the near wake can reveal both the

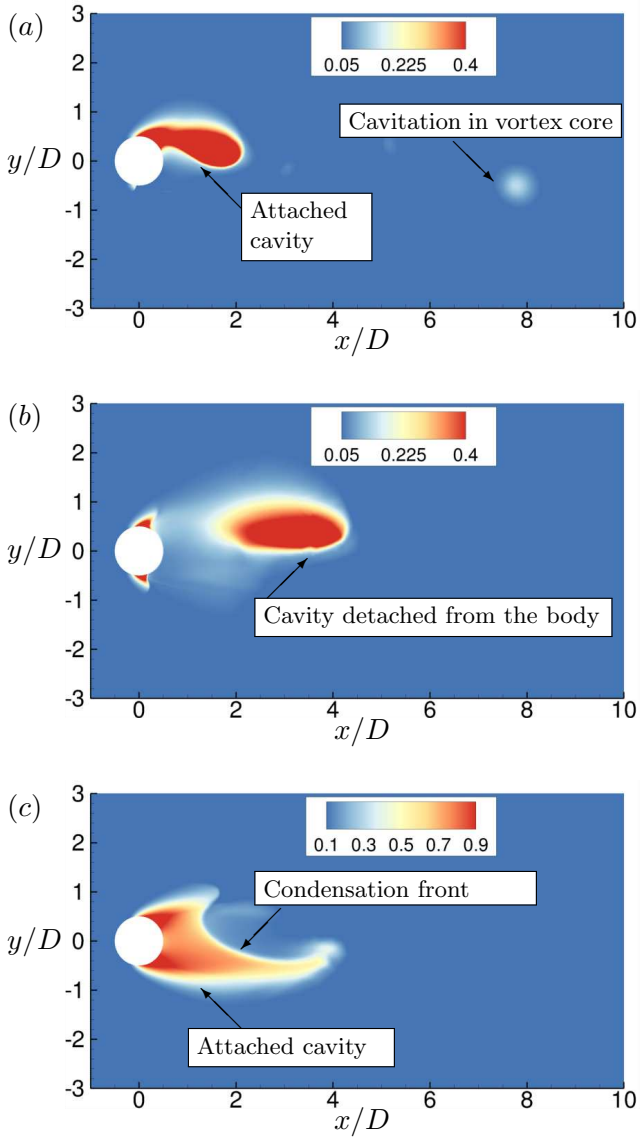

Figure 3.2: Instantaneous total void fraction (vapor + NCG volume fraction) contour for the cyclic regime (a) and for the transitional regime (b, c) for Case B.

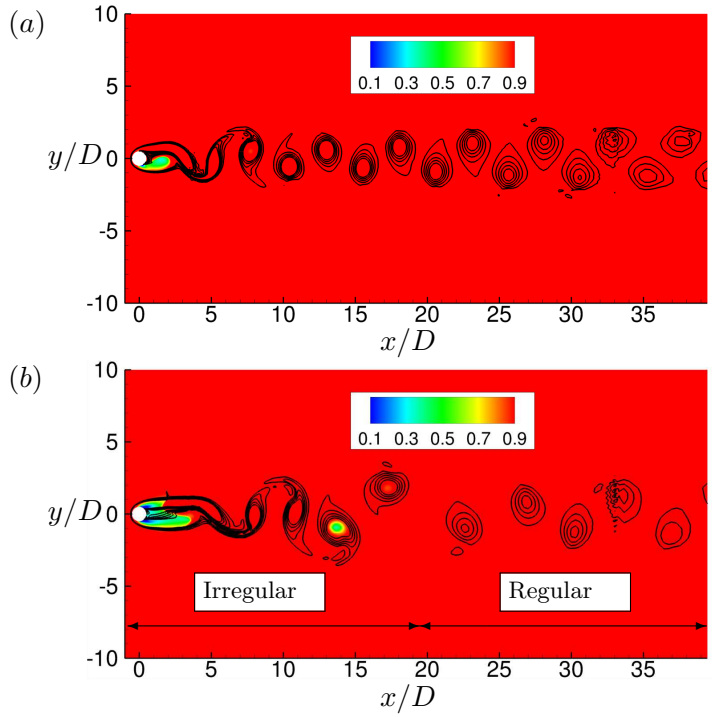

Figure 3.3: Instantaneous solution indicating vortex shedding at $\sigma = 1.0$ (a) and $\sigma = 0.7$ (b) for Case B. Lines indicate constant vorticity and coloured countours represent density.

vortex and/or cavity shedding frequency. In the cyclic regime (figure 3.3(a)), the dominant shedding frequency is that of a single cavitated vortex from the surface into the wake. Note the regular vortex shedding from top and bottom of the cylinder in this regime (figure 3.3(a)). In the transitional regime (figure 3.3(b)), we observe that this regular vortex shedding is disrupted at the onset of condensation front propagation, which occurs as the entire aft–body of the cylinder cavitates due to lower σ. Consequently, the cylinder wake exhibits irregular and regular vortex shedding periodically (figure 3.3(b)). The dominant shedding frequency in the transitional regime indicates the cavity shedding after the passage of the condensation front and the recurrence of irregular and regular vortex shedding processes. The frequency of individual vortex shedding from the surface becomes secondary.

St versus σ

We define Strouhal number ($St = fL/U$) to characterize the shedding frequency and plot it over a range of cavitation numbers spanning the cyclic and the transitional regime as shown in figure 3.4. Here, f is the cavity shedding frequency obtained from drag history, U is the free–stream velocity and two length scales, D and L_{cav}, are chosen for L and plotted respectively in figure 3.4(a) and 3.4(b). L_{cav} is the cavity length defined as the position along the wake centerline where the total void fraction decreases to a value lower than 0.05 [6, 111]. The values used to compute St at different σ in figure 3.4(b) are shown in figure 3.4(c) and compared to the experimental fit from Varga and Sebestiyen [112] showing good agreement. We note that St computed for non–cavitating conditions is 0.385. With reduction in σ, St decreases in the cyclic regime. Gnanaskandan and Mahesh [44] explained this behavior through vorticity dilatation due to cavitation. However, the authors did not consider the sharp jump in St moving through the transitional regime with further reduction in σ (figure 3.4). Fry [28] characterized the transition from the cyclic to the transitional regime by a peak in pressure fluctuations along the wake. Exactly at this transition, we observe that St drops by an order of magnitude with σ ($St = 0.285$ at $\sigma = 0.85$ to $St = 0.018$ at $\sigma = 0.75$) as the dominant frequency in the cyclic regime due to the periodic vortex shedding shifts to the frequency of irregular–regular vortex shedding in the transitional regime.

In addition, a maxima in the St versus σ plot (figure 3.4(b)) is observed at $\sigma = 0.85$ when L_{cav} is chosen as a reference length. Young and Holl [113] and Ganesh et al. [111] for flow over a triangular prism reported similar maximum in St versus σ. They considered a configuration with flow confinement (top/bottom walls) and considered the base of the prism as the length scale.

Effect of NCG

Note that St corresponding to the dominant frequency of shedding plotted in figure 3.4 shows that the trend observed is not sensitive to the free–stream nuclei content of vapor and NCG. However, a small amount of NCG does influence the secondary shedding

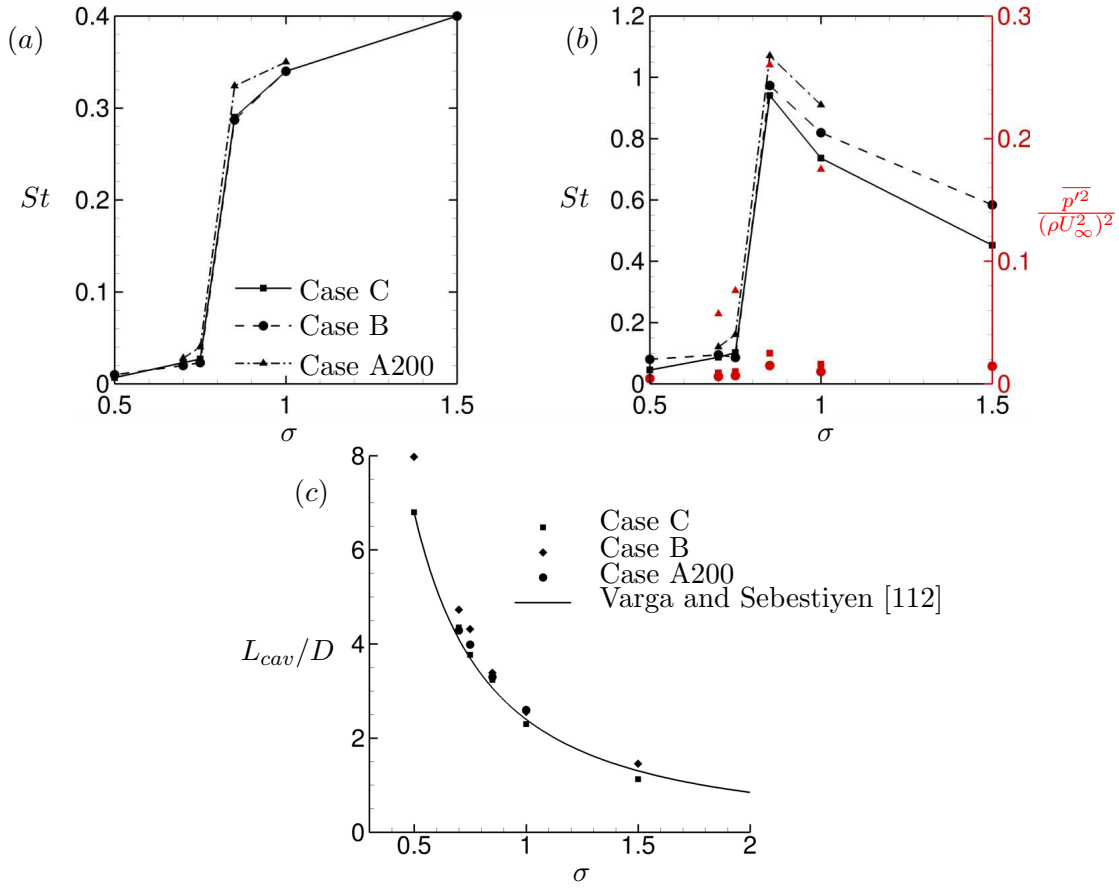

Figure 3.4: St for different σ based on the cylinder diameter (a) and cavity length (b). Non–dimensional pressure fluctuations are represented by red symbols in (b) for Case A200 (▲), Case B (●) and Case C (■). Cavity length normalized by cylinder diameter for different σ (c).

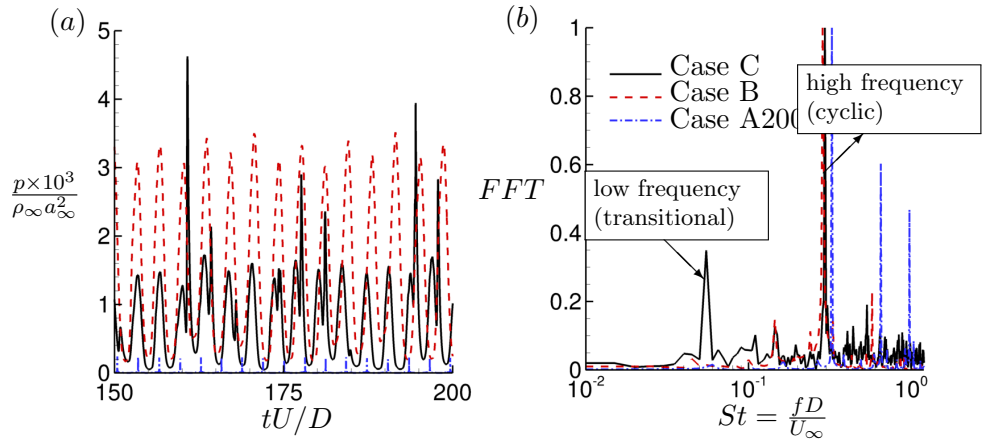

Figure 3.5: (a) Pressure signal at $x = 2.5D$ in the cylinder wake scaled with free–stream density and speed of sound at $\sigma = 0.85$ and (b) FFT of the corresponding signal scaled with its maximum value for better visualization.

process, which is explained through the frequency components of the pressure history in the wake of the cylinder as shown in figure 3.5. We consider $\sigma = 0.85$ corresponding to the cyclic cavitation regime near transition. The pressure history of flow without NCG exhibits both cyclic and transitional behavior; the dominant frequency corresponds to cyclic shedding. In the presence of NCG, regardless of its free–stream nuclei content, the low frequency due to regular–irregular vortex shedding (figure 3.5(b)) of the transitional regime is completely suppressed. Thus, the presence of NCG can delay the transition from cyclic to transitional shedding.

In order to understand the effect of gas on the pressure waves produced due to cavity collapse, we plot the pressure history in the wake of cylinder at $x/D = 2.5$ and $x/D = 5$ along the wake centerline, as shown in figure 3.6 for Case B and Case C at $\sigma = 1.0$. Note that at $x/D = 2.5$, the peak value of pressure is less when the NCG is present. Also, the pressure wave produced due to collapse no longer has a sharp pressure peak as it reaches the station at $x/D = 5$ as seen in figure 3.6(b). The distance between the peaks at $x/D = 2.5$ and $x/D = 5$ in the time domain reflects the propagation speed of the wave, which is smaller when the NCG is present. This is due to the reduction in sound speed of the mixture in the presence of gas. Smaller amplitudes of pressure

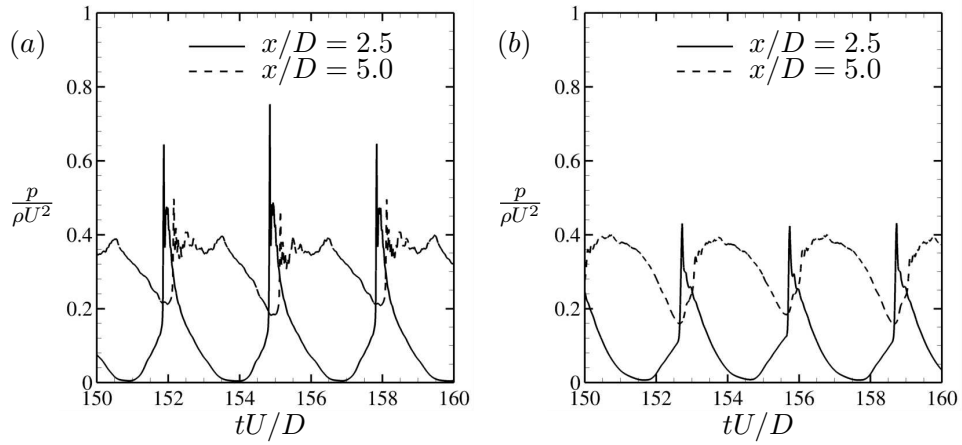

Figure 3.6: Pressure history for the flow where NCG is absent (Case C) (a) and present (Case B) (b).

waves can be explained from the inviscid, isentropic relation for pressure perturbation in the medium,

$$p - \overline{p} = \overline{a}^2(\rho - \overline{\rho}) = Z\overline{a}S \tag{3.1}$$

where $S = (\rho - \overline{\rho})/\overline{\rho}$ is the condensation ratio, $\overline{a}$ is the mean sound speed and $Z = \overline{\rho}\,\overline{a}$ is the acoustic impedance of the medium. Acoustic impedance is smaller for the medium when NCG is present due to reduction in mean density and sound speed. Pressure perturbation scaled by $Z\overline{a}$ is plotted in figure 3.7(a). Peak values of scaled pressure perturbations are smaller when the gas is present indicating smaller condensation ratio. This is also seen from the total void fraction plots in figure 3.7(b). We can see that as the pressure wave passes through the medium in which the gas is present, it creates smaller drop in total gaseous phase void fraction. Reduction in sound speed, lower acoustic impedance and smaller condensation ratio entails smaller pressure perturbation in the presence of non–condensable gas as seen from equation (3.1). Therefore, in the presence of NCG weaker pressure waves impinge on the cylinder surface. Consequently, the secondary peak in lift curve, which is due to the impingement of the pressure wave on the cylinder surface (primary peak correspond to cavity shedding) as shown in figure

3.7(c), is absent in the presence of non–condensable gas.

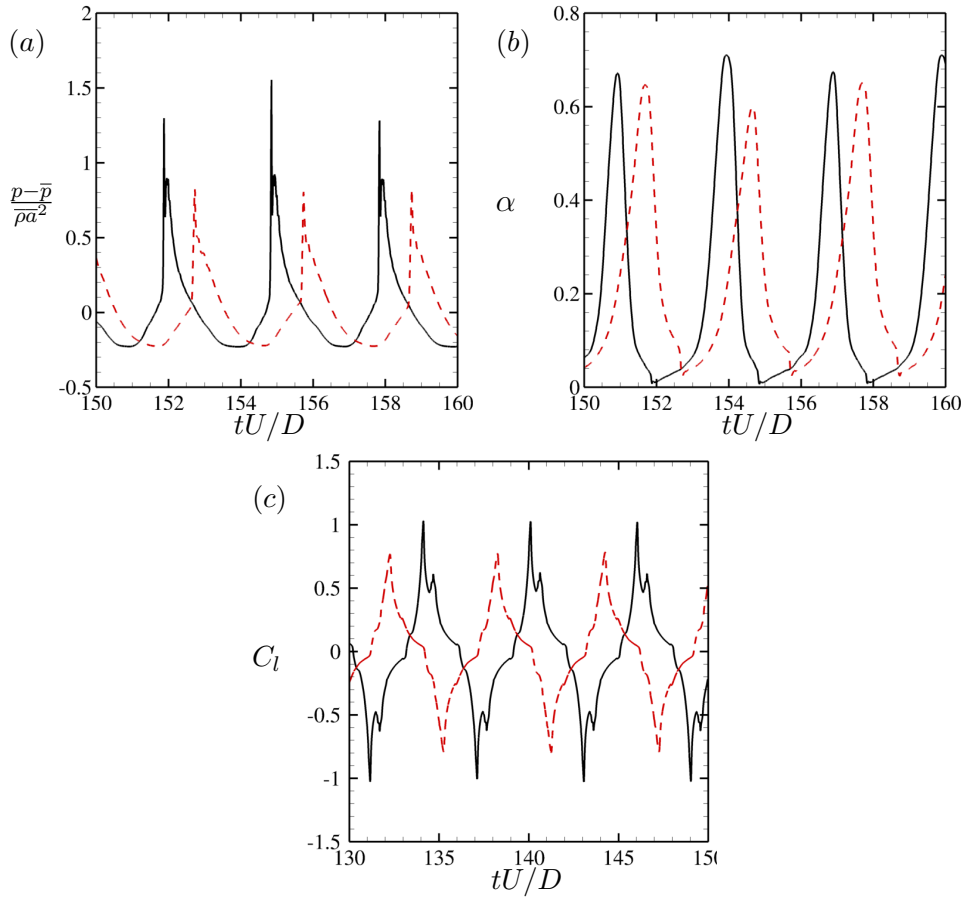

Figure 3.7: Scaled pressure pertubation (a) and total void fraction (b) along the wake centerline at $x/D = 2.5$, and lift curves (c) for Case C (——) and Case B (----).

Dynamic mode decomposition

A detailed analysis of the behavior behind the dominant frequencies in both the cyclic and the transitional, as well as in the non–cavitating regime, is considered by performing dynamic mode decomposition (DMD) and examining the corresponding modes. DMD is a data–driven modal decomposition technique that identifies a set of modes from multiple snapshots of the observable vectors. An eigenvalue is assigned to each of these modes, which denotes the growth/decay rate and oscillation frequency of the

mode. The obtained modes and their eigenvalues capture the system dynamics. We use a novel DMD algorithm developed by Anantharamu and Mahesh [114] that has low computational cost and low memory requirements. The basic idea behind DMD is that the set of observable vectors (snapshot vectors of flow variables) $\{\psi_i\}_{i=1}^{N-1}$ can be written as a linear combination of DMD modes $\{\phi_i\}_{i=1}^{N-1}$ as

$$\psi_i = \sum_{j=1}^{N-1} c_j \lambda_j \phi_j; i = 1, ..., N-1, \tag{3.2}$$

where λ_j are the eigenvalues of the projected linear mapping and c_j are the j^{th} entry of the first vector ψ_1. The complete derivation of the algorithm can be seen in Anantharamu and Mahesh [114]. For the cyclic and non–cavitating regime around $N = 200$ snapshots of the flow field were taken with $\Delta t/(D/u_\infty) = 0.1$ between them, while $N = 400$ snapshots with $\Delta t/(D/u_\infty) = 0.5$ were taken for the transitional regimes. We consider (i) the delay of Kármán vortex street transition to the two layer vortices moving from non–cavitating to the cyclic cavitation regime and (ii) comparison of mode shapes in the cyclic and the transitional regime.

The dominant mode for Case A200 at non–cavitating ($\sigma = 5.0$) and cavitating conditions in the cyclic regime ($\sigma = 1.0$ and $\sigma = 0.85$), corresponds to the dominant frequencies in lift spectra and are shown in figure 3.8 colored by spanwise vorticity. These dominant frequencies in lift spectra indicate the shedding frequency of individual vortices. The dominant mode in figure 3.8(a) clearly reveals the primary Kármán vortex street and its transition to a two–layered vortex street. The streamwise position of this transition is Re dependent and is observed at about $x = 23D$ for the non–cavitating case in figure 3.8(a). Comparison to the cavitating cases in figures 3.8(b) and (c) reveals that this transition is delayed to $x = 30D$ for $\sigma = 1.0$ and to even farther distances at $\sigma = 0.85$. This indicates that cavitation delays the first transition of the Kármán vortex street and that its distance from the cylinder grows with decreasing cavitation number.

Figures 3.9(a) and (b) display the vortex street at $\sigma = 5.0$ and $\sigma = 1.0$ respectively. The vortices inside the boxes are used to compute the spacing ratio, as defined in section 3.2.1, at two streamwise positions: the first position is the closest possible to

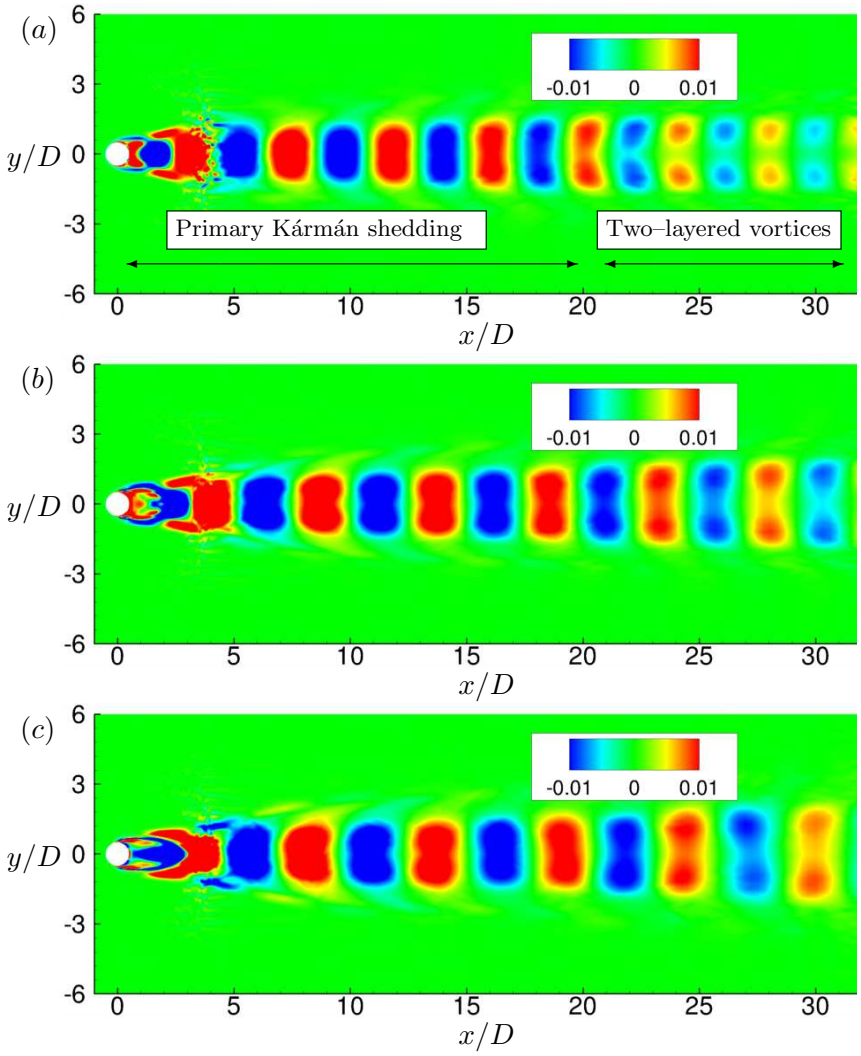

Figure 3.8: Most energetic modes colored by spanwise vorticity at $\sigma = 5.0$ (a), $\sigma = 1.0$ (b) and $\sigma = 0.85$ (c).

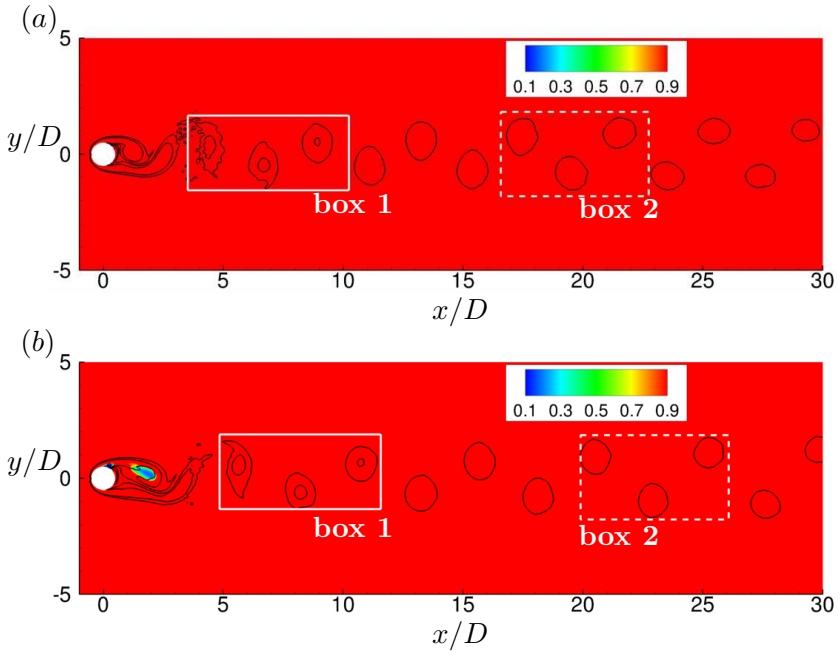

Figure 3.9: Vortex street colored by density for $\sigma = 5.0$ (a), $\sigma = 1.0$ (b). White boxes indicate the region where spacing ratio is computed.

the cylinder and the second is just before the vortex street transition. Table 3.2 shows that for $\sigma = 5.0$, the spacing ratio more than doubles over a small distance, quickly surpassing the 0.366 threshold estimated by Durgin and Karlsson [109]. Meanwhile, the spacing ratio for $\sigma = 1.0$ grows slowly with streamwise distance and it is just slightly higher than the limit of 0.366 before the transition initiates. In order for the spacing ratio to be larger in the non–cavitating case, either the cross–wake distance (h) has to be higher or the longitudinal distance (a) has to be smaller. Table 3.2 reveals that it is the longitudinal distance between same sign vortices that is smaller for $\sigma = 5.0$ at the two different streamwise positions. This parameter is inversely proportional to the shedding frequency of individual vortices, which is reduced from 0.193 to 0.175, based on lift history, when cavitation number is lowered from $\sigma = 5.0$ to $\sigma = 1.0$. Thus, we can conclude that the reduction of shedding frequency due to cavitation plays a major role in delaying the first vortex street transition.

Mode shapes of axial velocity corresponding to the dominant frequency of the drag

		h	a	h/a
$\sigma = 5.0$	box 1	0.845	4.421	0.191
	box 2	1.633	4.027	0.406
$\sigma = 1.0$	box 1	1.147	5.026	0.228
	box 2	1.751	4.724	0.371

Table 3.2: Cross wake distance between different sign vortices (h), longitudinal distance between same sign vortices (a) and their ratio at two different wake positions for $\sigma = 5.0$ and $\sigma = 1.0$.

spectra are significantly altered moving from the cyclic to the transitional regime (figure 3.10). Length scales of the corresponding modes are an order of magnitude larger for the transitional regime, explaining the sharp jump in St. In the transitional regime (figure 3.10(b)), the modes are horizontally stretched and their length scales are significantly higher than the distance between subsequent vortex shedding as observed in the cyclic regime (figure 3.10(a)). In addition, in the transitional regime immediately following the cylinder trailing edge, the mode shows large region of negative axial velocity, suggesting the flow reversal due to the condensation front propagation.

3.2.2 Mean flow characteristics

Distribution of vapor and NCG in the cylinder wake

We consider the distribution of mean volume fractions of vapor and NCG in the near wake of cylinder for Case A200 at $\sigma = 1$ and 0.7, respectively in the cyclic and the transitional regime, as shown in figure 3.11. In the cyclic regime (figure 3.11(a, b)), majority of the vapor is concentrated on the cylinder surface and core of shed vortices from top and bottom. Regions near the cavity trailing edge and in the immediate wake remain cavitation free. NCG is concentrated in the incoming shear layer beginning at the cylinder surface into the near wake. Also, note that NCG is distributed in the neighbouring regions of the vapor concentration. NCG volume fractions are orders of magnitude smaller than vapor as additional NCG cannot be produced through phase change and volume fractions are observed only through expansion of existing amount

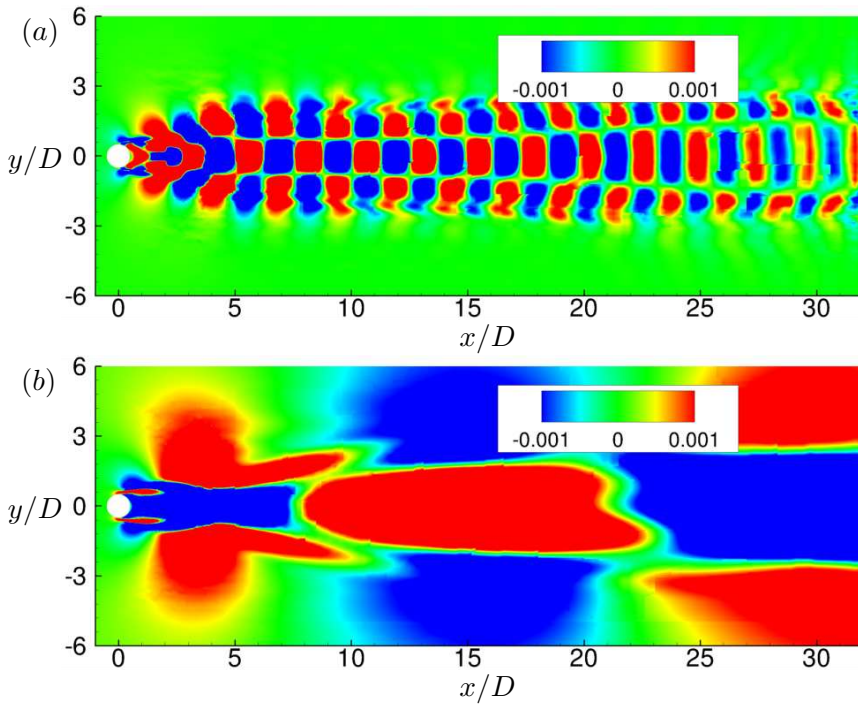

Figure 3.10: Modes corresponding to drag peak frequency at $\sigma = 1.0$ (a) and $\sigma = 0.7$ (b) for Case A200, colored with streamwise velocity.

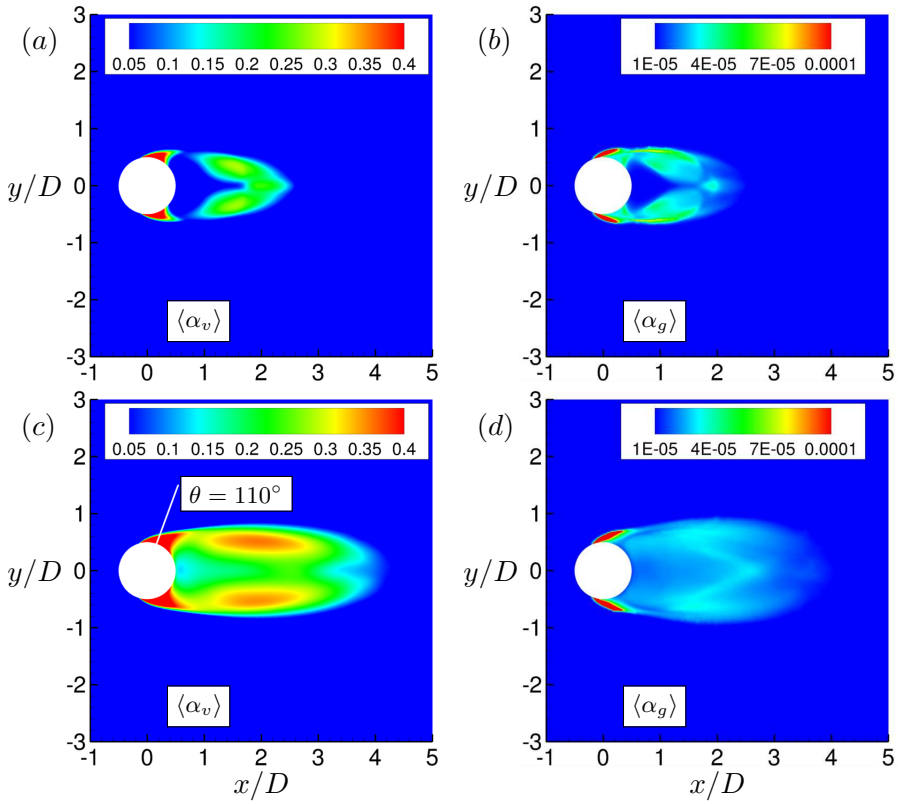

Figure 3.11: Time averaged vapor and NCG volume fraction contours respectively at $\sigma = 1$ (a, b) and $\sigma = 0.7$ (c, d) for the Case A200. White line in (c) indicates azimuthal position of 110°.

of gas in the free–stream. In the transitional regime (figure 3.11(c, d)), in addition to the cylinder surface and the core of shed vortices, vapor is produced near the cavity trailing edge and in the immediate wake as the local pressure in the immediate wake drops below vapor pressure with reduction in σ. NCG volume fractions are smaller than those observed in the cyclic regime and are concentrated mainly in the incoming shear layer.

Cavitation inside the boundary–layer

In order to distinguish the mass transfer process due to phase change from expansion, we consider the local cavitation number which is defined as $\sigma_{loc} = \frac{p_{loc} - p_v}{0.5\rho_\infty u_\infty^2}$, where p_{loc}

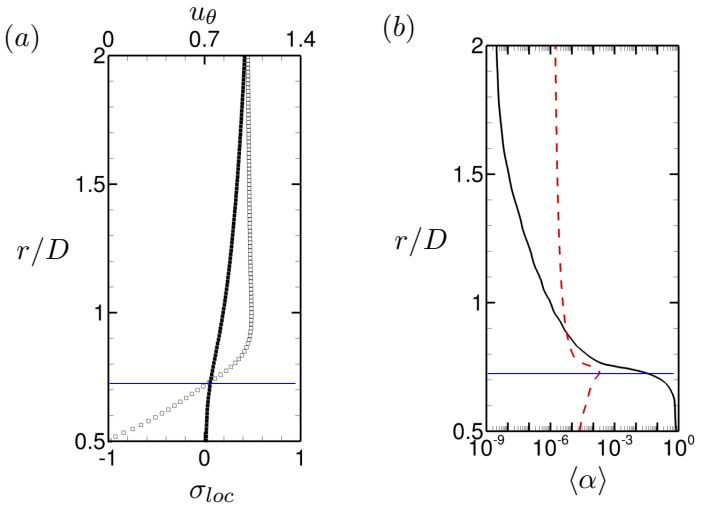

Figure 3.12: Cavitation inside the boundary–layer at $\sigma = 0.7$ and for Case A200. Profiles taken at 110° from the leading edge. (a) Azimuthal velocity profile (▫) with local cavitation number (■) and (b) mean vapor (——) and NCG (----) volume fraction.

is the local pressure inside a cell. At a given instant if σ_{loc} is positive in the region, the observed increase in vapor volume is only due to the expansion or the advection from nearby regions. If it is negative, the resulting increase in the volume of vapor is also accompanied by mass transfer. Consequently, in the regions of negative σ_{loc}, we expect the vapor to distinguish itself from NCG. We choose $\sigma = 0.7$ and Case A200 for explanation. Figure 3.12(a) shows boundary–layer profile radially at 110° from leading edge (as indicated in figure 3.11(c)) of the cylinder along with σ_{loc}. The region separating positive σ_{loc} within the boundary–layer is indicated by the solid blue line. Note that vapor and NCG volume fractions deviate significantly in this region (figure 3.12(b)) as vapor is produced due to the mass transfer. The maximum NCG volume fraction is observed at $\sigma_{loc} = 0$. As one moves radially outward, both vapor and NCG gas volume fractions are comparable in the remaining regions within the boundary–layer, predominantly due to the expansion and the advection process; finally reaching to the corresponding free–stream values. Hence, cavitation as a mass transfer process is only observed in a finite near–wall region within the boundary–layer.

Effect of free–stream nuclei

We discuss two important effects of the free–stream nuclei content: i) distribution of vapor/NCG in the near wake and ii) laminar separation of the boundary–layer. Figure 3.13 shows vapor/NCG distribution as discussed in the section 3.2.2, although at a high concentration of vapor/NCG (Case B). In the cyclic regime, vapor volume fractions show only minor difference in magnitude and distribution as compared to the low free–stream nuclei concentration (Case A200, in figure 3.11). However, the NCG volume fraction is orders of magnitude higher as compared to the low free–stream nuclei case (figure 3.11(b), figure 3.13(b)) and its distribution is almost indistinguishable from vapor at high nuclei concentration (figure 3.13(a, b)). As NCG does not undergo phase change, its initial concentration in the free–stream has a very significant effect on the wake of the cylinder. While due to the significant effect of mass transfer, vapor is not as sensitive as NCG to the initial nuclei content. The same is also observed in the transitional regime (figure 3.13(c, d)). Note that vapor/gas diffusion can influence the distribution shown in the near wake. Although, we are unable to consider it at the current level of modeling.

One point of divergence between experiments and simulations using the homogeneous mixture approach involves the location of boundary–layer separation. While experiments show that the boundary–layer separation point moves upstream along the cylinder as the flow cavitates [115], the same was not observed numerically by Gnanaskandan and Mahesh [44]. The reason behind this discrepancy, as explained in Gnanaskandan and Mahesh [44], is the fact that the homogeneous mixture approach predicts the inception point upstream of the boundary–layer separation point. In our simulations with low free–stream void fraction (Case A200), the inception point is also observed to be upstream of the separation point (not shown here). Differently from the work in Gnanaskandan and Mahesh [44], where a high free–stream void fraction is employed, the boundary–layer separation point is shifted upstream as the cavitation number is reduced from non–cavitating condition to a cavitating one when the free–stream contains small amounts of vapor and gas (Case A200). This is evident from figure 3.14(a) that shows the skin friction along the cylinder surface, with the separation

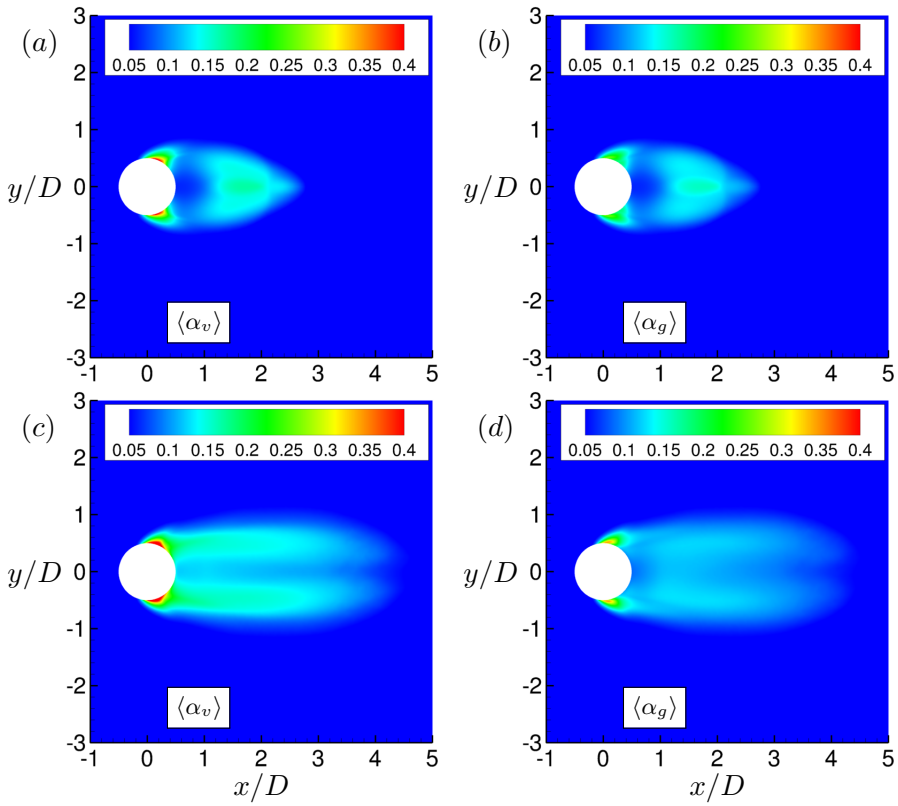

Figure 3.13: Time averaged vapor and NCG volume fraction contours respectively at $\sigma = 1$ (a, b) and $\sigma = 0.7$ (c, d) for Case B.

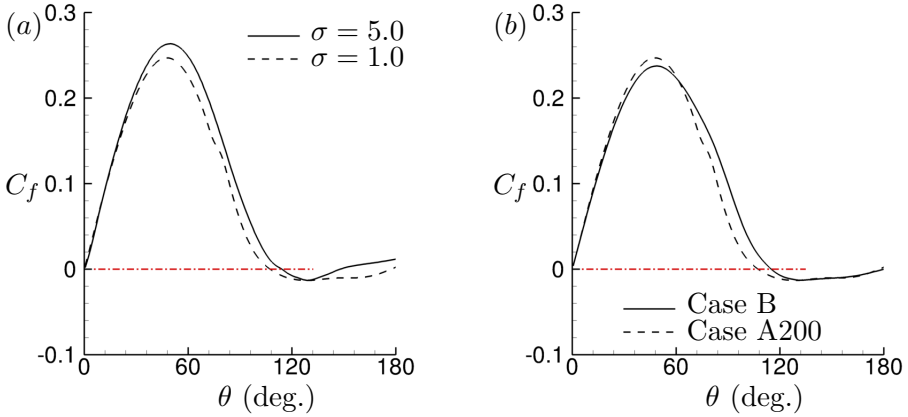

Figure 3.14: Skin friction at different σ for Case A200 (a) and at $\sigma = 1.0$ for different cases (b). The dash red line represents $C_f = 0$ and indicates the separation point.

point shifting from 115° to 106° as σ is reduced from 5.0 to 1.0.

It is found that the contents of vapor and NCG in the free–stream have significant impact on the separation point, as displayed in figure 3.14(b), with it moving downstream (from 106° to 116°) as the free–stream volume fraction increases. In Gnanaskandan and Mahesh [44], the authors discussed that the cavitation would start as soon as the local pressure is reduced to values below the vapor pressure. The expansion due to cavitation would then push the separation point downstream. The same behavior is observable for Case A200. Beside this is the fact that before the flow cavitates, both vapor and gas traveling along the cylinder surface expand due to a decrease in pressure. Both the ideal gas expansion and the subsequently expansion due to phase change contribute to pushing the boundary–layer separation further downstream. The reason for Case A200 showing the correct change in the boundary–layer separation point as the flow cavitates in comparison with the high volume fraction cases, however, lies on the fact that as the amounts of vapor and gas at the cylinder surface are substantially reduced, so are their effects on the flow due to ideal gas expansion. This leads to the conclusion that by adding NCG to a cavitating flow, the separation point would move downstream.

3.2.3 Condensation shock

In this section, we consider the low frequency cavity shedding in the transitional regime using $\sigma = 0.7$ to illustrate the shedding cycle in the presence (Case A200) and absence (Case C) of NCG. Figure 3.15 shows density contours taken at two different instances during the cycle for Case C (figure 3.15(a, c)) and Case A200 (figure 3.15(b, d)). The condensation front is visualized by the density discontinuity in the cavity closure region as indicated by the arrows in figure 3.15(a). As the front propagates upstream when NCG is absent, it condenses the vapor along the way, finally detaching the cavity completely as it impinges on the trailing edge of the cylinder as shown in figure 3.15(c). In the presence of NCG however, figure 3.15(d) shows that the cavity remains attached after the cylinder is struck by the first propagating front. A second front is formed approaching the cylinder trailing edge. This indicates that when NCG is present, the pressure recovery in the back of the cylinder after the passage of the first front is not enough to condense the vapor and to compress large amounts of NCG in order to lead to cavity detachment. This indicates that a weaker condensation front impinges the cylinder surface in the presence of NCG. Likewise, Vennig et al. [39] in the experimental investigation on a flow over a hydrofoil observed that when the flow was rich in nuclei, a first shock wave only partially condensed the cavity prior to the passage of second shock wave leading to full spanwise detachment.

In order to quantify the behavior we construct an $x-t$ diagram by taking data along the wake centerline (starting from trailing edge of the cylinder to a $5D$ distance along the wake) and stacking them in time. The $x-t$ diagram is shown in figure 3.16(a) and (b) for Case C and Case A200, respectively. The density discontinuity moving towards the cylinder when advancing in time indicates the condensation front. The slope of this discontinuity represents the inverse of the speed of the propagating front. It is evident here that in the presence of NCG, two fronts propagate before the complete detachment of the cavity as shown in figure 3.16(b). Curvature in the density discontinuity indicates that the speed of the condensation front changes as it travels towards the cylinder in the presence of NCG as compared to the almost straight line for the case without gas.

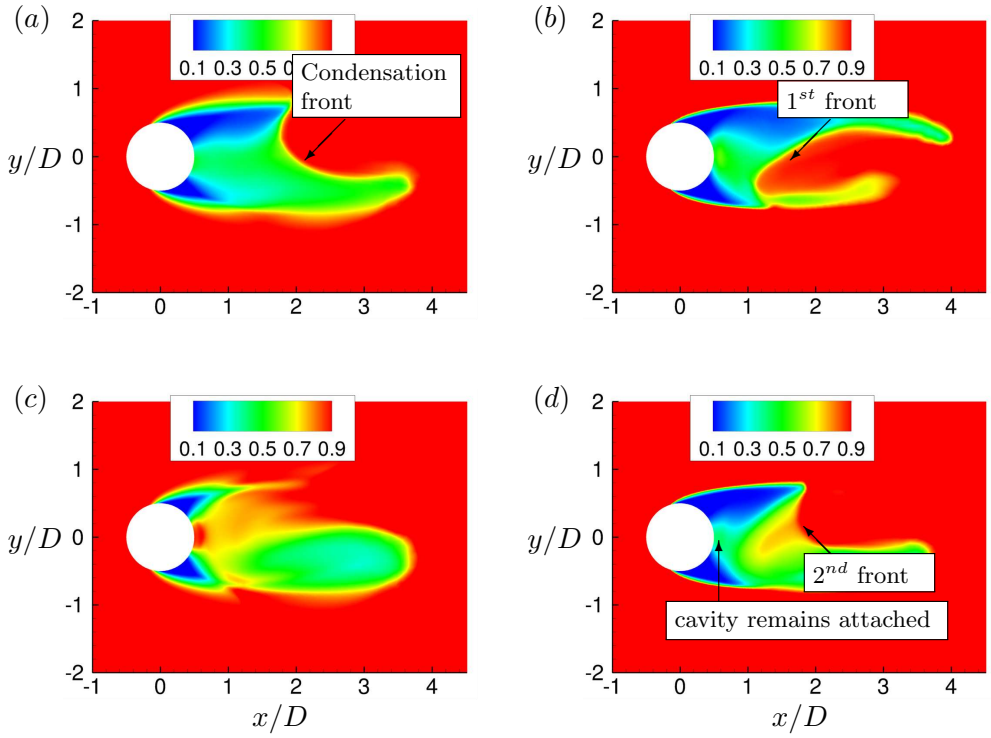

Figure 3.15: Density contours showing the propagation of a condensation front in the absence (Case C) (a, c) and presence (Case A200) (b, d) of NCG.

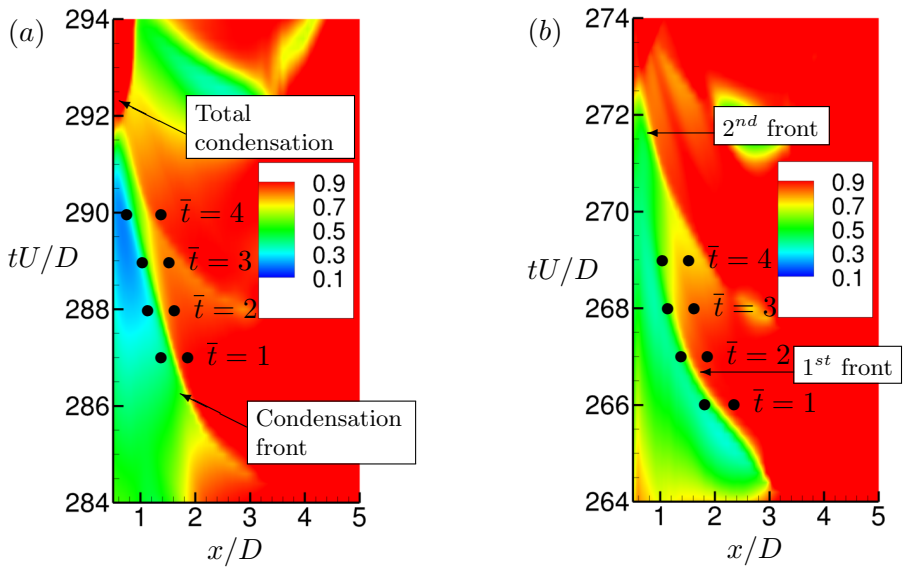

Figure 3.16: $x - t$ plot of density along the wake centerline for $\sigma = 0.7$ when (a) NCG is absent (Case C) and (b) present (Case A200).

Therefore, we use Rankine–Hugoniot jump conditions derived in Appendix B at different time instances ($\bar{t}$), as given in figure 3.16, to obtain the speed of the front. Left and right states in the equation (B.15) are obtained from quantities across the condensation front in the $x - t$ plot at the given time instants and are indicated by the bullet points. The speed of sound ahead of the front is obtained using equation (2.11).

Shock Mach numbers

The speed of condensation front along with the sound speed allows us to comment on the Mach number at which the front propagates. Figure 3.17 shows the computed Mach number for the condensation front when NCG is absent (Case C) and present (Case A200) for the time instances mentioned in figure 3.16. Note that the computed Mach numbers refer to the first condensation front that impinges on the cylinder. Interestingly, all the Mach numbers in the figure 3.17 are greater than 1, indicating that the front is indeed supersonic; it is henceforth referred to as condensation shock. An important distinction is that in the presence of NCG, the Mach number at which the condensation

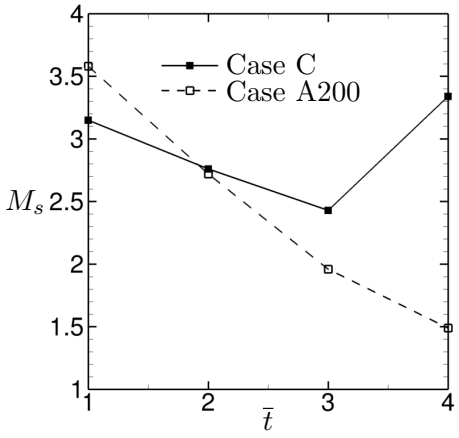

Figure 3.17: Mach number of condensation front for $\sigma = 0.7$.

shock impinges the cylinder is much smaller than in the case without the gas, despite both having nearly same Mach numbers when they are formed. It is also evident that the shock Mach number monotonically reduces as it approaches cylinder in the presence of NCG. This reduction in shock Mach number is associated with a decrease in pressure jump across the discontinuity in the presence of gas, which will be discussed later in this subsection.

Cavity Mach numbers

In the condensation shock regime, the shock wave induced by the collapse of a previously shed cavity, propagates upstream through the growing cavity initiating the condensation process [33]. Since the shock cannot propagate through the cavity if it is supersonic, it is important to consider the Mach numbers inside the cavity for the range of cavitation numbers studied, in order to assess the onset of the condensation shock. Here we consider two σ for Case C; $\sigma = 0.85$ (figure 3.18) in the cyclic regime and $\sigma = 0.7$ (figure 3.19) in the transitional regime. Note that the cavity Mach numbers are different from the shock Mach numbers computed in the earlier section. For $\sigma = 0.85$, instantaneous density contours showing the cavity region (figure 3.18(a)) and corresponding Mach number contours (figure 3.18(b)) indicate that the cavity is supersonic. It is noticeable that the pressure wave generated due to the collapse of the previously shed cavity

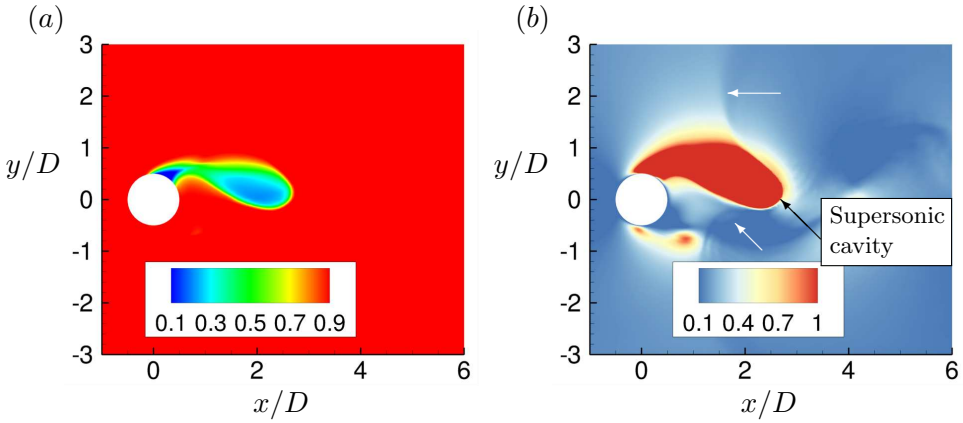

Figure 3.18: Instantaneous density (a) and Mach number (b) contour of the attached cavity for $\sigma = 0.85$.

(indicated by the white arrow), does not propagate through the cavity as shown in figure 3.18(b), and instead travels through the surrounding subsonic liquid region. In contrast, at $\sigma = 0.7$, the cavity region surrounding the cylinder trailing edge and near wake is subsonic as shown in figure 3.19(a). The propagation of the shock wave through the cavity is indicated by the black arrow.

Effect of NCG on condensation shock

Previously, it was demonstrated that in the presence of NCG, the Mach number of the condensation shock decreases as it approaches the cylinder. Consequently, two condensation shock waves were necessary for complete condensation and detachment of the cavity. This section explains this weakening of the condensation shock as it travels in the presence of NCG. The strength of the condensation shock is characterized by the pressure ratio and is plotted in figure 3.20 for the instants of time mentioned in figure 3.16. It is evident that the pressure ratio monotonically decreases as the shock approaches the cylinder surface in the presence of NCG (Case A200). The initial pressure ratio of 16 reduces to 2.5 near the cylinder trailing edge. Variation in the pressure ratio when NCG is absent (Case C) is expected due to the finite rate of condensation; if the condensation rate is not strong enough to condense large portions of the vapor as

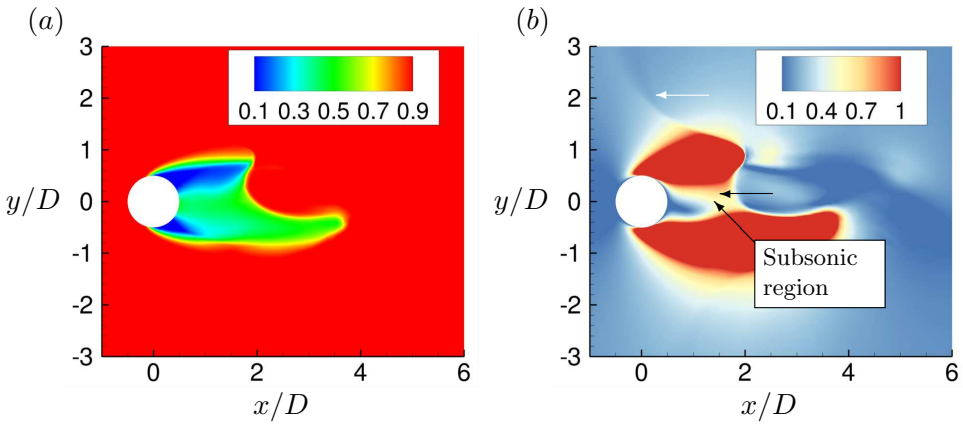

Figure 3.19: Instantaneous density (a) and Mach number (b) contour of the attached cavity for $\sigma = 0.7$.

the shock moves, some amount of uncondensed vapor remain after the passage of the shock decreasing its strength. In the cases considered here, the pressure rise observed across the condensation shock is much lower as compared to the pressure jump across the typical shock wave generated due to cavity collapse.

Reduction in the pressure ratio due to the presence of gaseous phase behind the shock is explained by considering a typical setting of condensation shock moving from water to the cavity consisted of vapor/NCG mixture as shown in figure 3.21(a). Density and pressure behind the shock (ρ_R and p_R) are higher than that ahead of the shock (ρ_L and p_L). At time $t+\Delta t$, the condensation shock moves through the cavity of vapor/gas mixture to $x+\Delta x$ creating region $R*$ behind the shock as shown in figure 3.21(b). Now, the jump conditions are determined across the region L and $R*$. Assuming that the vapor is completely condensed as the shock travels through the cavity; if the cavity consisted only of vapor, the region $R*$ behind the shock remains nearly the same as R and is primarily water. In contrast to that, if the cavity also had NCG, the region $R*$ would have the mixture of water and NCG. Consequently, the overall density is reduced as compared to the original density of water ($\rho_{R^*} < \rho_R$), and using the jump conditions derived in (B.14) it can be shown that the pressure jump accordingly is also reduced ($p_{R^*}/p_L < p_R/p_L$). Hence, the condensation shock weakens as it propagates through the cavity that contains NCG. Subsequently, we consider the conditions at

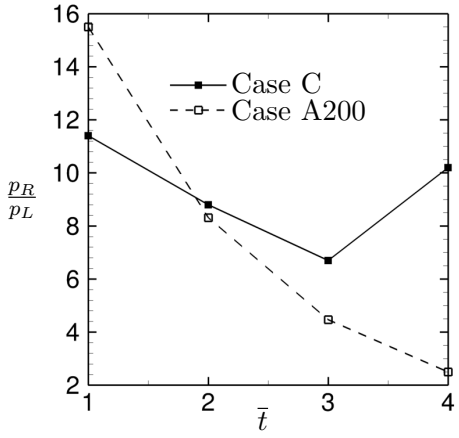

Figure 3.20: Pressure ratio across a condensation shock for $\sigma = 0.7$.

which condensation shock cease to exist as it weakens with the reduction in pressure ratio.

For single–phase flows, the pressure ratio across the shock is determined uniquely using the shock Mach number [116]. However, this is not the case for condensation shocks since multiple phases can be present on either side of the shock. Equation (B.15) derived in Appendix B shows that the shock speed and consequently the shock Mach number are not uniquely related to the pressure ratio, it also depends on vapor/NCG mass fractions ahead and behind the shock and the resulting density difference. In contrast, pressure and density ratio are equal to 1 at sonic conditions for single–phase flows. As an example, figure 3.22 shows pressure jump plotted at sonic conditions across a condensation shock using the current system of equations and the jump conditions described by equation (B.14) for different amounts of total void fraction ahead of the front (α_L). It is clear that in case of condensation shocks, the pressure jump is not unique at a given shock Mach number.

By combining the ratios of density and gaseous phase volume fraction into a single parameter ($\beta = \frac{\alpha_R/\alpha_L}{\rho_R/\rho_L}$) and plotting the resultant pressure ratio for different shock Mach number, figure 3.23(a) is obtained and equation (3.3) can be derived from it with a linear fit, assuming u_L to be 0 for simplicity.

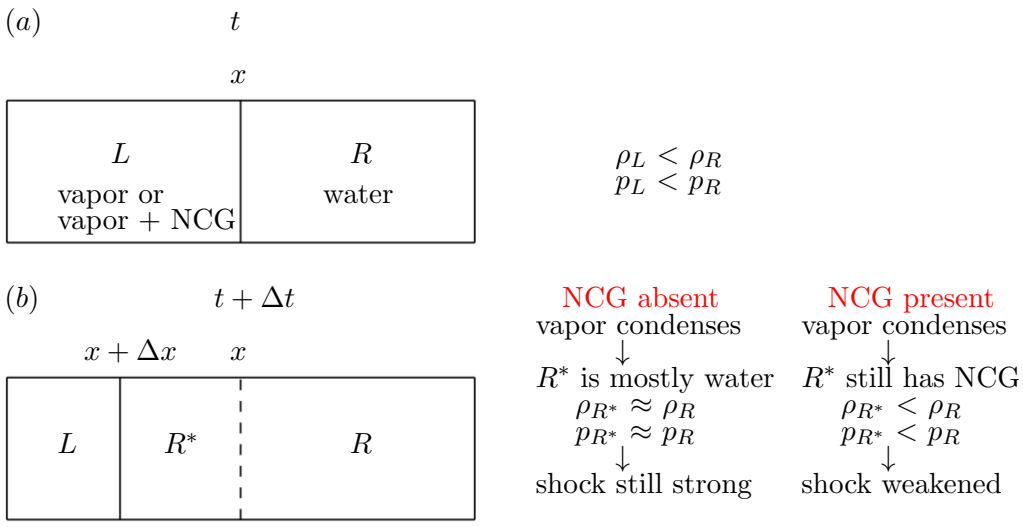

Figure 3.21: Diagram for the example of a left–moving shock.

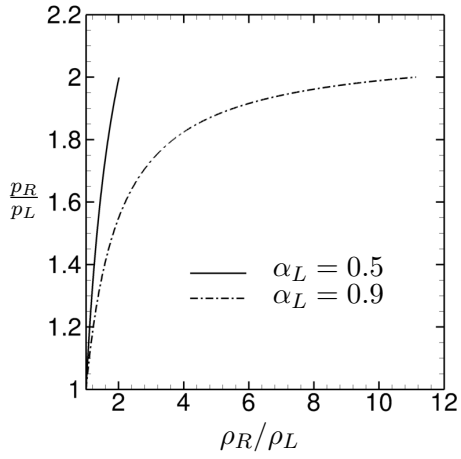

Figure 3.22: Pressure jump across condensation shock at sonic conditions for different density ratios and gaseous phase void fractions ahead of the shock

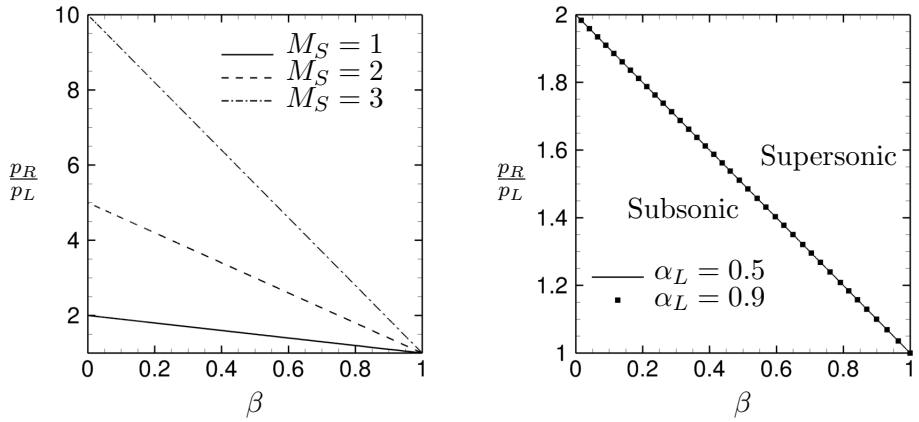

Figure 3.23: Pressure ratio against different values of β at different M_S (a). Pressure ratio necessary for condensation shock (b).

$$p_R/p_L = -M_S^2\beta + M_S^2 + 1. \tag{3.3}$$

At sonic conditions, the pressure ratio is simplified to

$$p_R/p_L = 2 - \beta, \tag{3.4}$$

and is shown in detail in figure 3.23(b). From figure 3.23(b), it is evident that the results of figure 3.22 can collapse when plotted using equation (3.4). Figure 3.23(b) allows us to consider a parameter space for which the condensation front is supersonic. Note that in the single–phase limit ($\alpha_R = \alpha_L = 1$), equation (2.5) reduces to the ideal gas equation of state and equation (3.4) suggests that $p_R/p_L = 1$ and $\rho_R/\rho_L = 1$ has to be identically satisfied at sonic conditions. $\beta = 0$ when the phase is completely liquid behind the shock. This suggest that the pressure ratio has to be greater than 2 for the condensation front propagating from the liquid ($\beta = 0$) into a gaseous cavity to be supersonic. It is important to note, however, that if the phase behind the shock is not completely liquid ($\beta > 0$), the pressure ratio for the occurrence of supersonic Mach number can be less than 2. In the current simulations, although the pressure ratio across the condensation front reduces as it propagates through the cavity containing

NCG, it remains greater than a factor of 2, indicating that the condensation front remains supersonic as it travels towards the cylinder. Since the state ahead of the shock is the attached cavity, we can conclude that as long as the pressure ratio across the condensation shock does not drop to values below 2, the condensation shock will remain supersonic regardless of the amounts of gaseous phase inside the cavity.

3.2.4 LES of cavitating flow at $Re = 3900$

LES of turbulent cavitating flow over a cylinder is performed at $Re = 3900$ in both the cyclic and the transitional regimes, respectively at $\sigma = 1.0$ and $\sigma = 0.7$, using low free–stream nuclei concentration (Case A3900). As noted in the Appendix C, the temperature changes in the flow are negligible. Hence, we perform LES calculations using isothermal formulation.

Cyclic regime

We consider mean vapor and NCG volume fraction at $Re = 3900$ and compare it to $Re = 200$ (figure 3.24). At $Re = 3900$, only a thin layer of vapor is observed at the cylinder surface as compared to the $Re = 200$ (figure 3.24(a, c)). Also, at higher Re, more vapor is observed in the region of near wake. At $Re = 3900$, the incoming boundary–layer is turbulent and confined close to the cylinder surface. This results in higher vorticity inside the Kármán vortices leading to larger pressure drop and more vapor production in the wake. The mean volume fraction of NCG at $Re = 3900$, however, is observed to be one order of magnitude lower than at $Re = 200$ (figure 3.24(b, d)).

The skin friction coefficient is compared to the result from Gnanaskandan and Mahesh [44] in figure 3.25. They studied the cyclic cavitation regime at $\sigma = 1.0$ using free–stream nuclei concentration of 0.01 for vapor (Case C of the current simulations). As noted for the laminar separation at $Re = 200$, we observe that at $Re = 3900$ the boundary–layer separation point moves upstream as compared to Gnanaskandan and Mahesh [44] (figure 3.25). The difference between the separation points is approximately

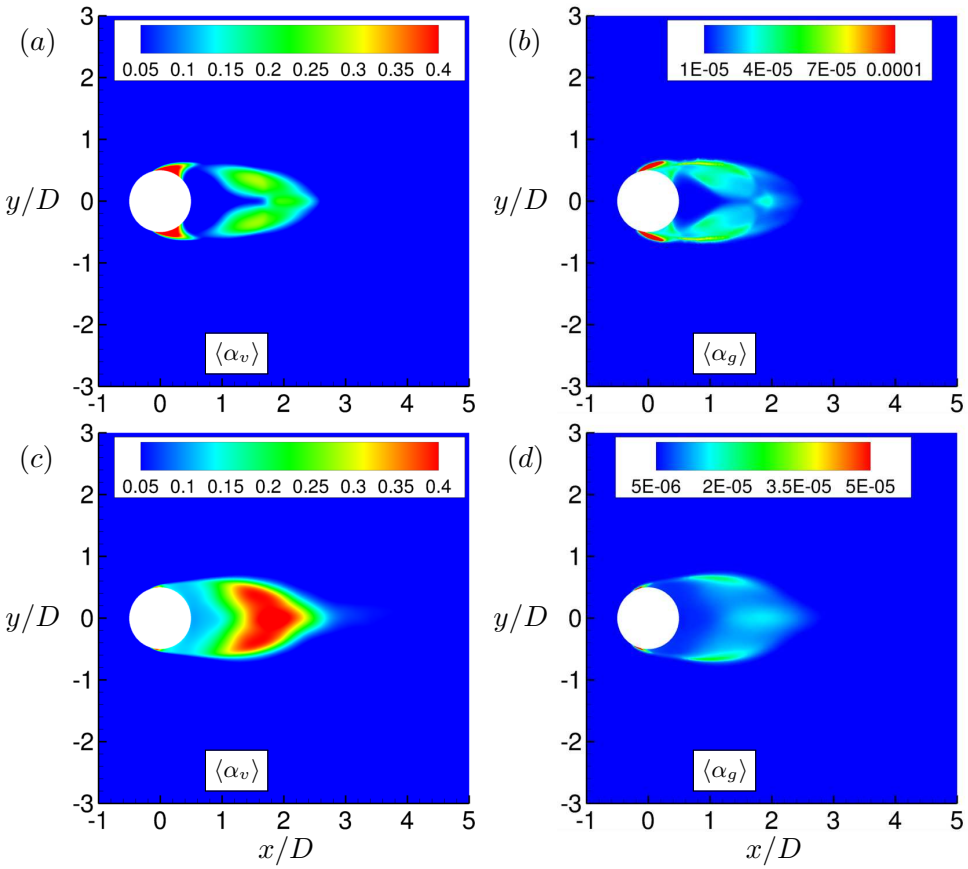

Figure 3.24: Mean volume fractions at $Re = 200$ ((a) vapor (b) NCG) and $Re = 3900$ ((c) vapor (d) NCG).

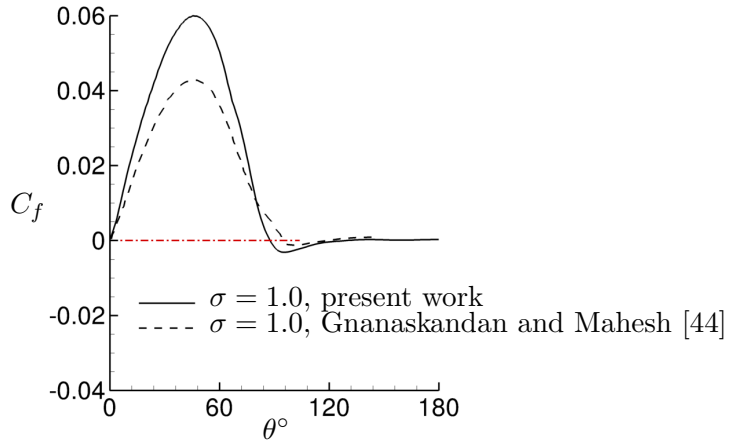

Figure 3.25: Skin friction coefficient at $Re = 3900$. Red dashed line identifies $C_f = 0$

10°, the same observed for $Re = 200$. These results confirm the role of free–stream total void fraction on the location of boundary–layer separation.

Transitional regime

We noted that in the transitional regime, flow cavitates over the entire aft body of the cylinder continuing into the regions in the immediate wake. Consequently, the grown cavity is observed to be nearly two–dimensional with negligible vorticity within the cavity (figure 3.26(b)). Figure 3.26(a, b) shows a comparison to the cyclic cavitation. In the cyclic regime, significant vorticity is observed in the immediate wake of the cylinder (figure 3.26(a)). Vortex stretching/tilting plotted in figure 3.26(c, d) confirms this distinction. In the transitional regime, a stable region of incoming shear layer is visible on the either side of the cylinder and majority of stretching/tilting is observed following the cavity closure. Consequently, in the transitional regime, periodic shedding and breakdown of Kármán vortices is significantly altered. In addition, in the cyclic regime due to the three dimensionality of the flow, significant vorticity production is observed in the near wake by mis–aligned density gradients in the cavity region and the pressure gradients in the pressure waves generated by cavity collapse. In the transitional regime, vorticity production within the 2D cavity is negligible, while vorticity production is observed in the cavity closure at the onset of three dimensionality in the flow.

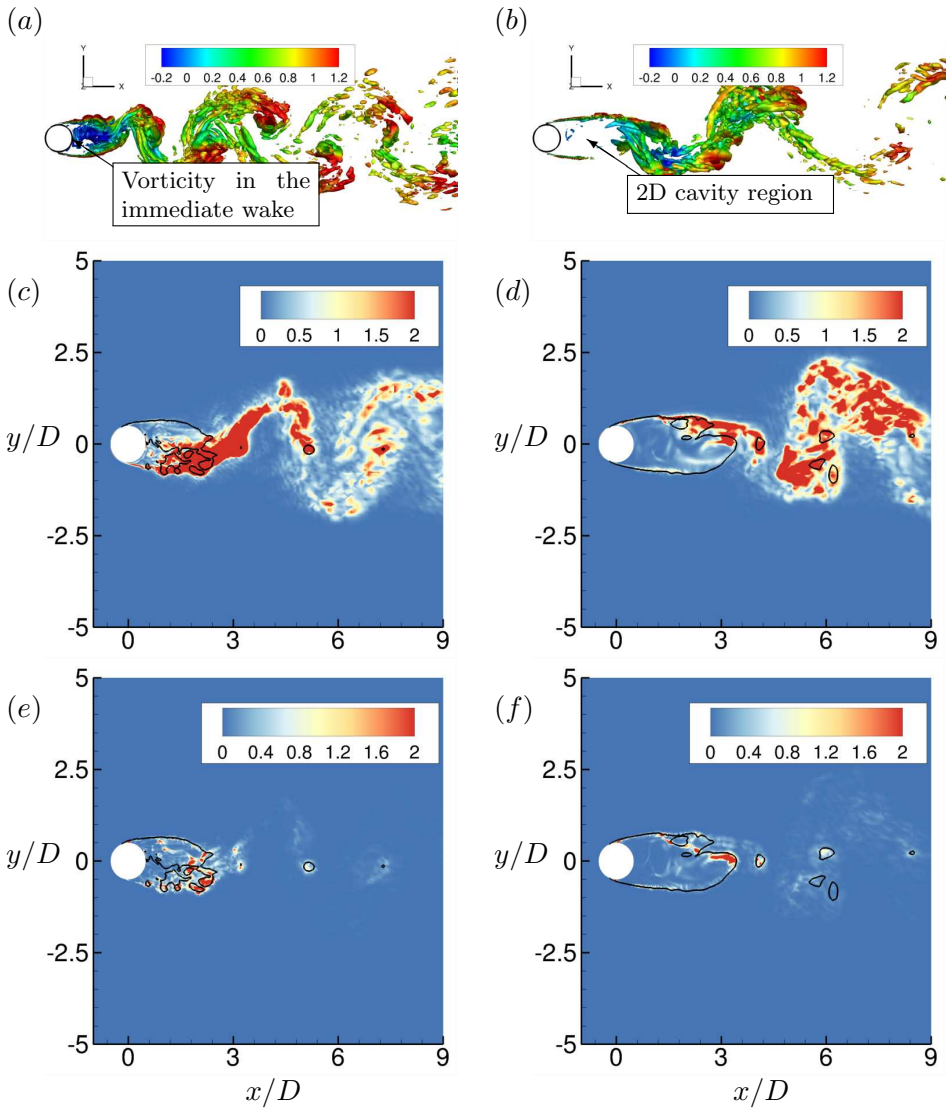

Figure 3.26: Vortex transport for cyclic regime (a, c, e) and transitional regime (b, d, f). Q criterion colored by streamwise velocity (a, b), vorticity stretching/tilting (c, d) and baroclinic torque (e, f). Black lines indicate isosurface of total void fraction of 0.1 and represent the cavity interface.

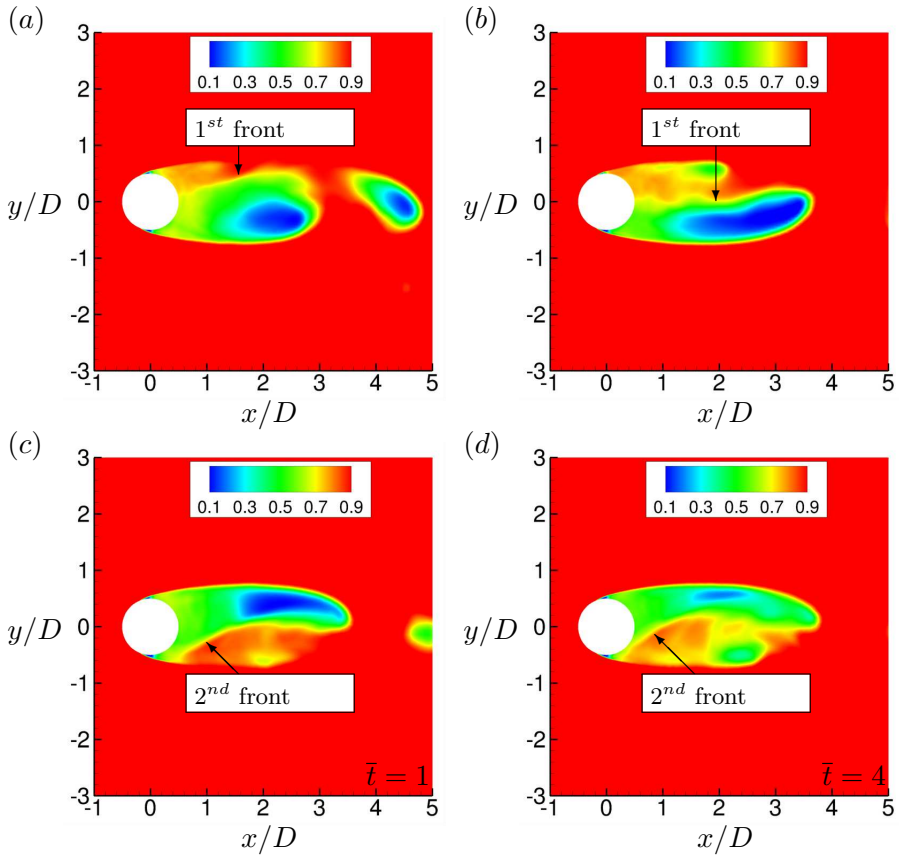

Figure 3.27: Spanwise average of density contours showing the propagation of a condensation front at $\sigma = 0.7$ and $Re = 3900$. Time increases from left to right.

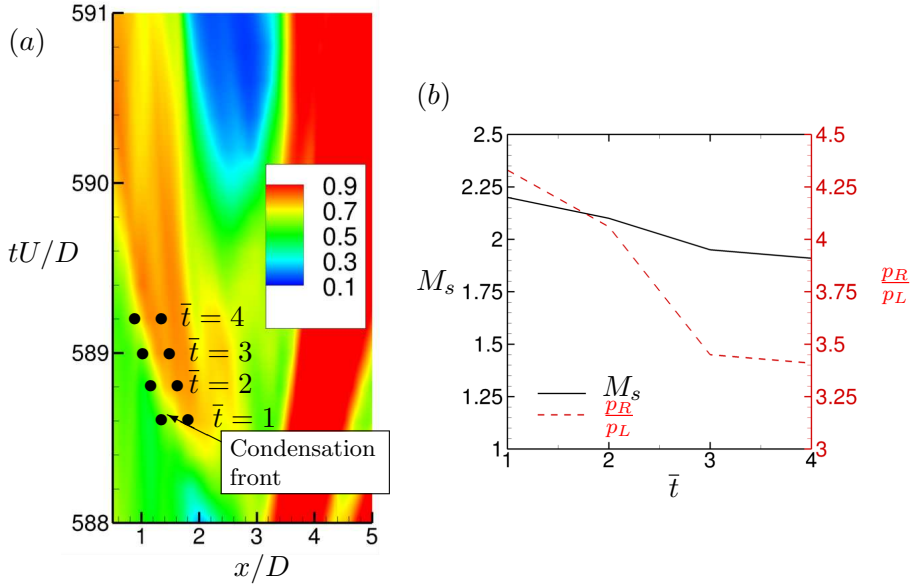

Figure 3.28: $x - t$ plot of spanwise averaged density (a) and condensation front Mach number and pressure ratio (b) at $\sigma = 0.7$ and $Re = 3900$.

In the transitional regime, at $Re = 200$, we observed that in the presence of NCG propagation of multiple condensation shocks leading to complete cavity detachment. The same is also observed at $Re = 3900$ as illustrated in figure 3.27 using spanwise averaged density contours at multiple time instances. Compared to $Re = 200$, the condensation front at $Re = 3900$ is oriented more vertically rather than towards the cylinder trailing edge. Note the first front moving in the direction of the negative $y - axis$ and the second front moving in the direction of positive $y - axis$ and also oriented towards the cylinder surface. Time evolution of condensation front propagation is shown using $x - t$ diagram in figure 3.28(a), only the section front moving towards the cylinder surface is considered. Initial and final time instances of the propagation are displayed in figure 3.28(c) and 3.28(d). Mach number and the pressure ratio across the condensation front are computed at the time instances indicated in figure 3.28(a) and are displayed in figure 3.28(b). Condensation front moves at supersonic speeds at all the instances considered, and consequently is a condensation shock wave. Also, note that the condensation shock is weakened as it propagates and approaches cylinder surface as

indicated in figure 3.28 by reduction in the pressure ratio.

Chapter 4

Inception in a turbulent shear layer

The objectives of this chapter are to (i) use LES to study inception in the turbulent shear layer of a backward–facing step applying the methodology presented in section 2.2, (ii) to find the regions more likely to cavitate using probability density functions, and (iii) to discuss the flow topologies leading to inception.

This chapter is organized as follows. Section 4.1 presents the problem setup while the results are discussed in section 4.2. Subsection 4.2.1 presents a brief analysis of the flow at $Re_\tau = 800$, while a detailed discussion of inception at $Re_\tau = 1500$ is provided in subsection 4.2.2.

4.1 Problem setup

The backward–facing step configuration is taken from the work of Agarwal et al. [4], which was employed for the validation study in subsection 2.2.3. A sketch is given in figure 2.12 and the geometry details are given in subsection 2.2.3. We simulate the experimental cases of $Re_\tau = \frac{\delta u_\tau}{\nu} = 800$ and 1500 (where δ is the boundary–layer thickness, u_τ is the friction velocity and ν is the kinematic viscosity). Differently form the validation case, this study is performed at a much higher Re and with a turbulent

boundary–layer as the inflow boundary condition. This inflow turbulent boundary–layer is generated through the recycle–rescale method of Lund et al. [117], later extended to unstructured grids by Kumar and Mahesh [118]. The flow where $Re_\tau = 800$ does not result in inception for any σ considered by Agarwal et al. [4]. Therefore, we simulate $Re_\tau = 800$ at a lower σ to validate the flow field and focus the analysis on the $Re_\tau = 1500$ flow. It is important to point out that in the present study, inception is assumed to have occurred when there are instances of time in which the local pressure anywhere in the domain drops below vapor pressure. The same criteria may not be used in other studies.

4.2 Result

4.2.1 Flow over backstep at $Re_\tau = 800$

The $Re_\tau = 800$ case is simulated to validate the ability of the LES to reproduce the mean and fluctuating velocity fields measured in the experiments of Agarwal et al. [4]. Such comparison provides confidence that the pressure field, which is central to inception, is accurately represented by our methodology of prescribing a turbulent boundary–layer at the inflow combined with LES. Agarwal et al. [4] study this case for cavitation numbers in the range of $0.45 \leq \sigma \leq 0.55$, however as previously mentioned, no cavitation is observed within this range at $Re_\tau = 800$. Once the velocity field is validated, we evaluate the cavitation model by dropping the inflow pressure to yield $\sigma = 0.25$. It is important to mention that this is not the inception σ. The process of finding the inception σ requires lowering the inflow pressure slowly and checking if there are instants of time where the local pressure is lower than vapor pressure. Different from the validation case in section 2.2.3, this task becomes demanding and computationally expensive for high Re. Given the amounts of vapor produced relative to the freestream levels, displayed later in this section, $\sigma = 0.25$ would be a case between inception and developed cavitation.

The inflow turbulent boundary–layer is generated on a separate flat plate domain with a grid resolution of $\Delta x^+ = 37$, $\Delta y^+ = 0.38$ and $\Delta z^+ = 20$. Figure 4.1 shows the boundary–layer colored by axial velocity and its verification against the data of

Schlatter and Örlü [119]. Good agreement is obtained for all quantities. Approximately 127 million cells are used in the backstep domain with $\Delta y^+ = 0.38$ and $\Delta x^+ = 20$ in the vicinity of the corner. The grid size is uniform in spanwise direction with $\Delta z^+ = 20$. A vapor concentration equivalent to $\alpha = 1 \times 10^{-5}$ is prescribed at the inflow. The velocity profiles are compared to experimental results of Agarwal et al. [4] at $x = 1S$ and $x = 3S$ downstream of the step in figures 4.2 and 4.3, showing good agreement. The predicted reattachment length is around $L_r = 6.4S$, which compares reasonably well with the experimental value of $L_r = 6.2S$. Figure 4.4 shows mean and fluctuation values of vapor volume fraction. Although cavitation is not observed experimentally at $Re_\tau = 800$, the work of Agarwal et al. [4] reports that at different higher Re_τ and at different values of σ, the location where cavitation is observed is at $0.45 < x/L_r < 0.75$. It is evident from figure 4.4 that cavitation activity seems restricted to the region of $0.4 < x/L_r < 0.8$, consistent with experiments. The values of α along the shear layer are not provided by the experiments, thus we can not compare them. However, this test shows that the model is able to simulate cavitation inception in complex flows.

4.2.2 Flow over backstep at $Re_\tau = 1500$

Inception in the shear layer of the backstep is studied at $Re_\tau = 1500$ at the experimental conditions of $\sigma = 0.55$ and $\sigma = 0.45$. The inflow turbulent boundary–layer is generated similarly to the previous case. The grid for this boundary–layer simulation has a resolution of $\Delta x^+ = 30$, $\Delta y^+ = 0.6$ and $\Delta z^+ = 32$. The flow field at an instant of time is illustrated in Figure 4.5(a) showing the axially developing boundary–layer. Figures 4.5(b) and (c) show the verification against the data of Eitel-Amor et al. [120]. It can be seen that we obtain a good agreement in the inner layer, but underpredict the u_τ as well as the Reynolds stresses, which can be explained by the mesh resolution.

For the backward–facing step domain, the grid contains 190 million cells with $\Delta y^+ = 0.6$ and $\Delta x^+ = 12$ in the vicinity of the corner and a uniform $\Delta z^+ = 32$ in the spanwise direction. Similar to the previous case, a vapor concentration equivalent to $\alpha = 1 \times 10^{-5}$ is prescribed at the inflow. The flow field at the center plane, $x = 1S$ and $x = 3S$ are displayed in figure 4.6. Figures 4.7 and 4.8 show a comparison between numerical and the

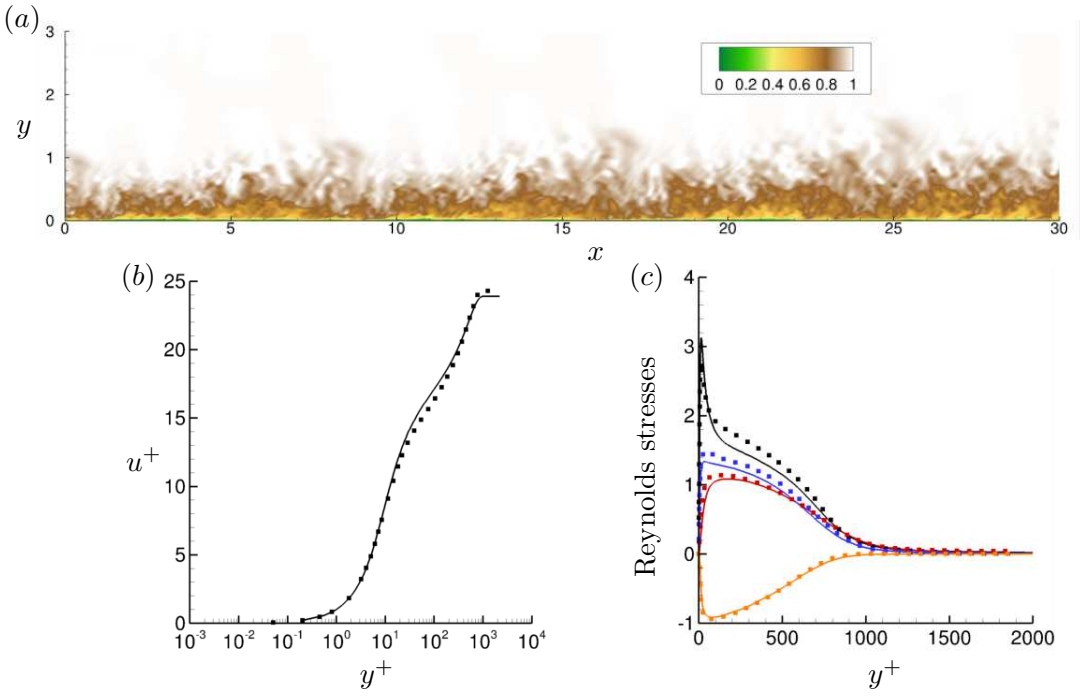

Figure 4.1: Turbulent boundary–layer colored by axial velocity (a). Mean values of axial velocity (b) and values of Reynolds stresses (c) at $Re_\tau = 800$. Simulation results (lines) compared against data from Schlatter and Örlü [119] (symbols). Black, red, blue and orange lines and symbols in (c) represent, respectively, $\sqrt{\langle u'^2 \rangle}/u_\infty$, $\sqrt{\langle v'^2 \rangle}/u_\infty$, $\sqrt{\langle w'^2 \rangle}/u_\infty$ and $\langle u'v' \rangle/u_\infty^2$.

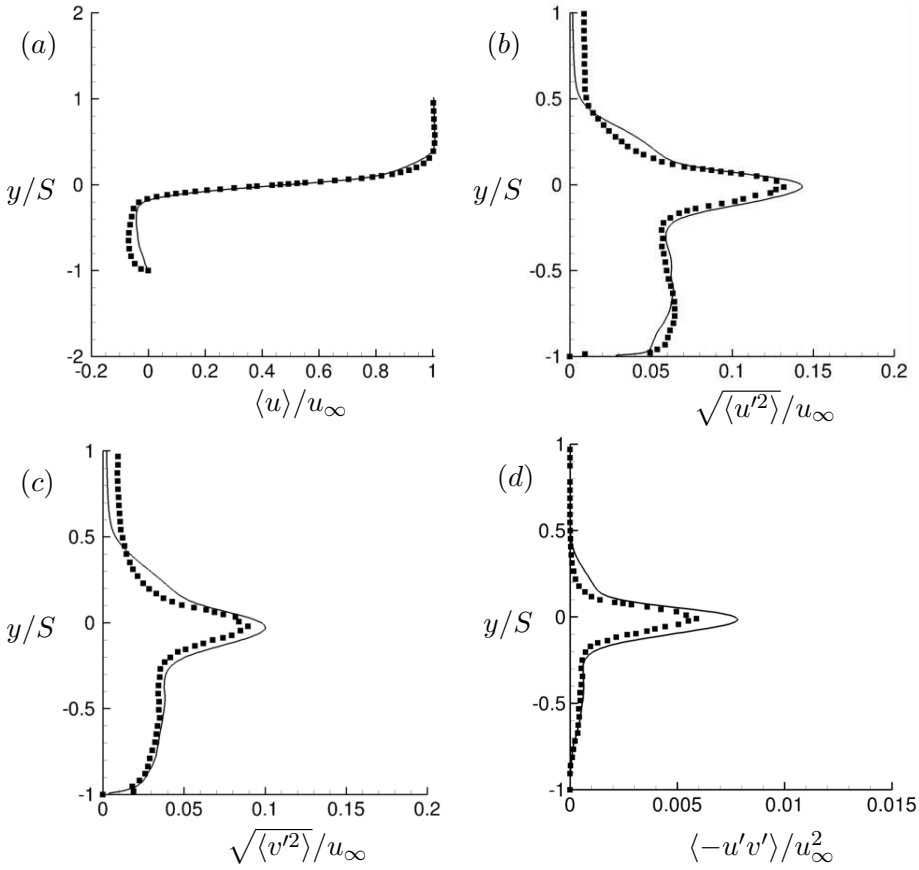

Figure 4.2: Comparison between numerical (lines) and experimental (symbols) profiles of mean velocity and Reynolds stresses for $Re_\tau = 800$ at $x = 1S$ downstream of the step. S represents the step height. The experimental values are obtained from the work of Agarwal et al. [4].

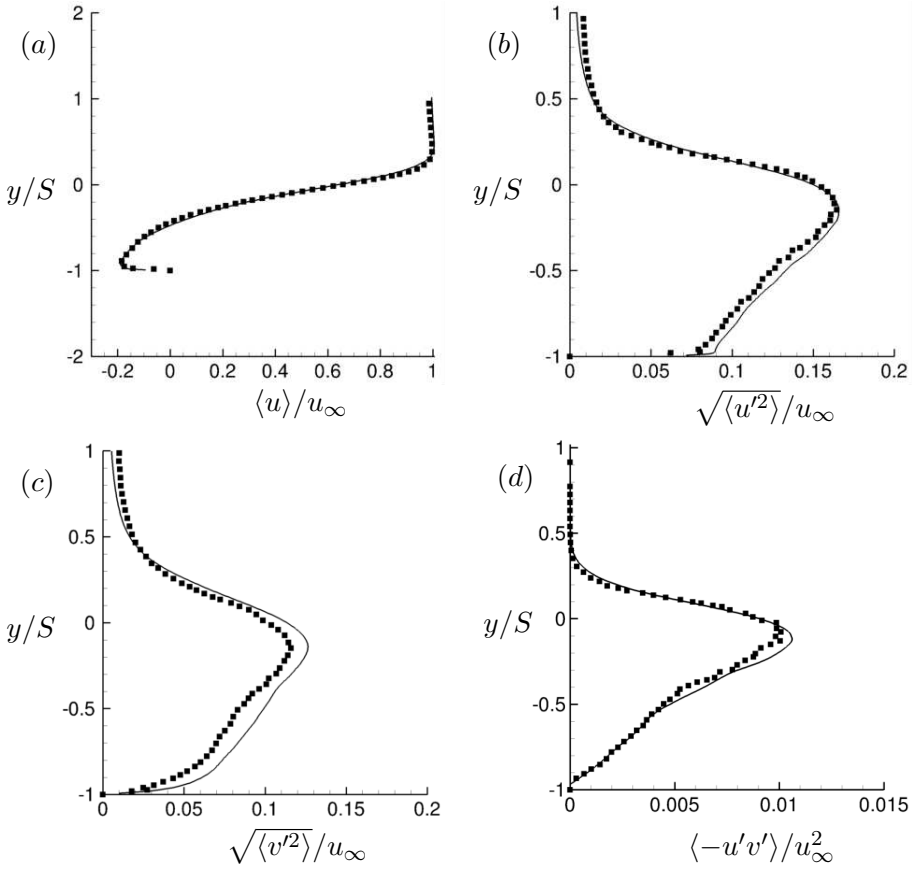

Figure 4.3: Comparison between numerical (lines) and experimental (symbols) profiles of mean velocity and Reynolds stresses for $Re_\tau = 800$ at $x = 3S$ downstream of the step. S represents the step height. The experimental values are obtained from the work of [4].

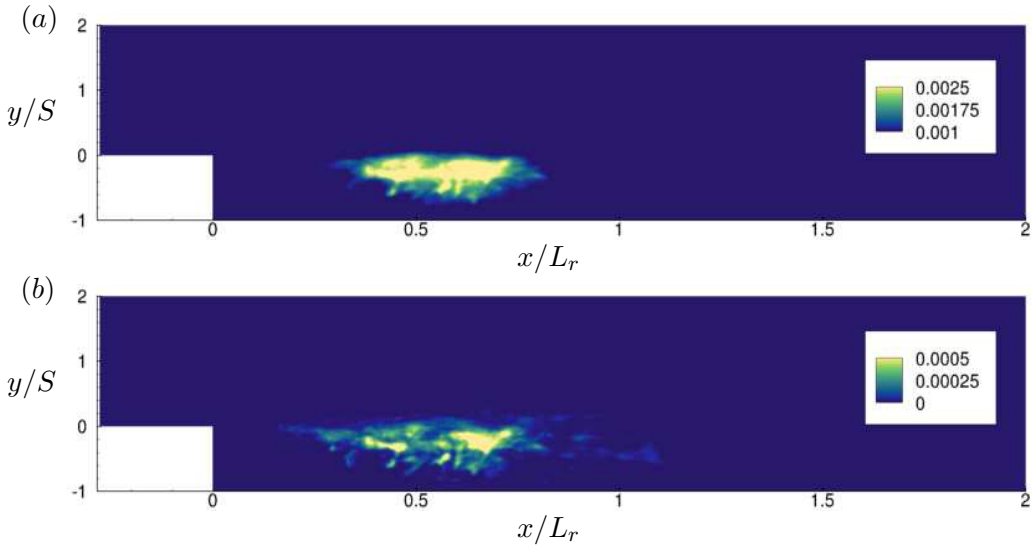

Figure 4.4: Contours of $\langle\alpha\rangle$ and $\langle\alpha'^2\rangle$ are given in (a) and (b), respectively, for $\sigma = 0.25$ at $Re_\tau = 800$.

experimental velocity profiles of Agarwal et al. [4] at $x = 1S$ and $x = 3S$, respectively. Good agreement is obtained for the shear layer profiles despite the differences observed in the incoming boundary–layer, which can be explained by the use of a finer Δx^+ at the backstep inlet section ($x/S < 0$ in figure 4.6(a)). The reattachment length obtained is $L_r = 6.0S$, which is 9% larger than the experimental value of $L_r = 5.5S$.

Pressure and volume fraction statistics

Figures 4.9(a) and (b) show probability density function (PDF) of pressure and volume fraction, respectively, between $x = 3S$ and $x = 6S$ for $\sigma = 0.55$. This region corresponds to the locations between $x = 0.5L_r$ and $x = L_r$. The measured pressure PDFs show a Gaussian behavior, which is also observed in Lee and Sung [121]. It can be noted that the probability of a low–pressure event is higher around half the reattachment point. According to the void fraction PDFs, the probability of finding regions of vapor seems confined around $x = 4S$, which is within the experimental range of Agarwal et al. [4]. Note that the location with a higher probability of a low–pressure event does not necessarily match the location with a high probability of finding vapor at

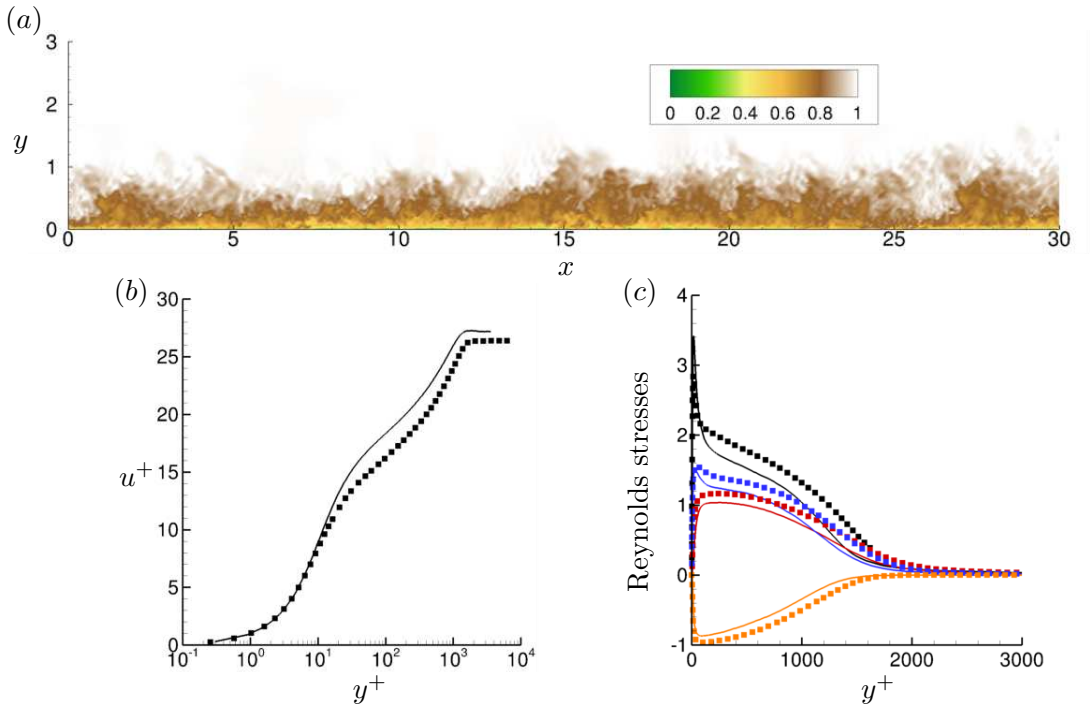

Figure 4.5: Turbulent boundary–layer colored by u/u_∞ (a). Mean values of axial velocity (b) and values of Reynolds stresses (c) at $Re_\tau = 1500$. Simulation results (lines) compared against data from Eitel-Amor et al. [120] (symbols). Black, red, blue and orange lines and symbols in (c) represent, respectively, $\sqrt{\langle u'^2 \rangle}/u_\infty$, $\sqrt{\langle v'^2 \rangle}/u_\infty$, $\sqrt{\langle w'^2 \rangle}/u_\infty$ and $\langle u'v' \rangle/u_\infty^2$.

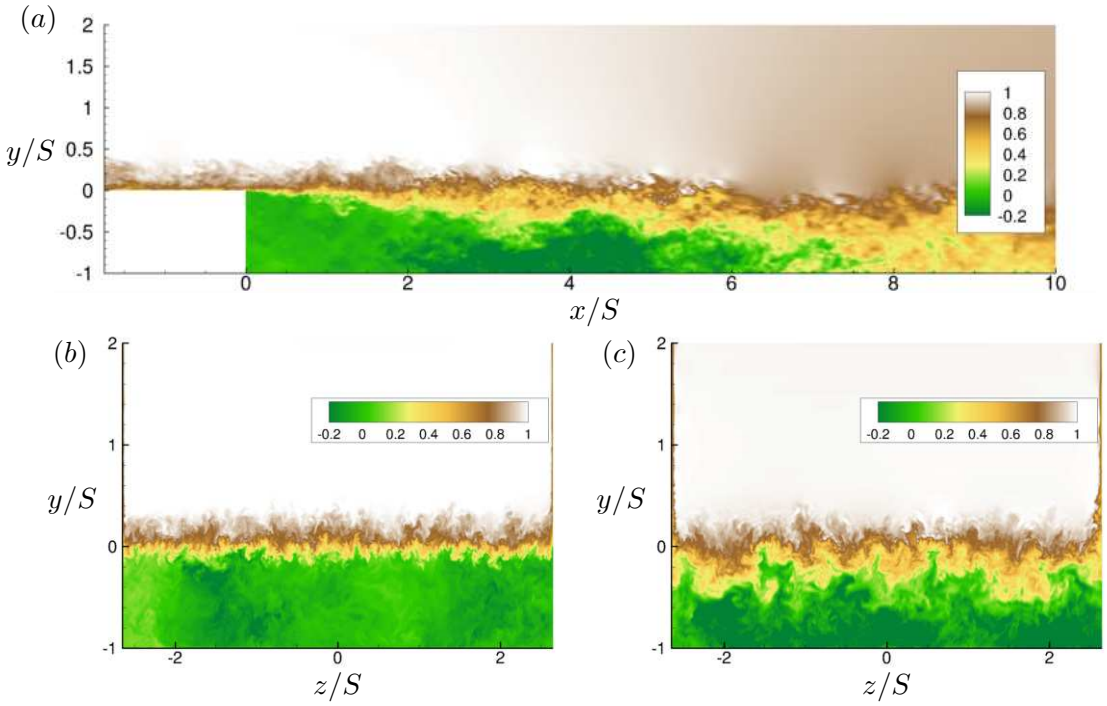

Figure 4.6: Instantaneous flow field colored with u/u_∞ for $Re_\tau = 1500$ at center plane (a) and at positions $x = 1S$ (b) and $x = 3S$ (c) downstream of the step. S represents the step height.

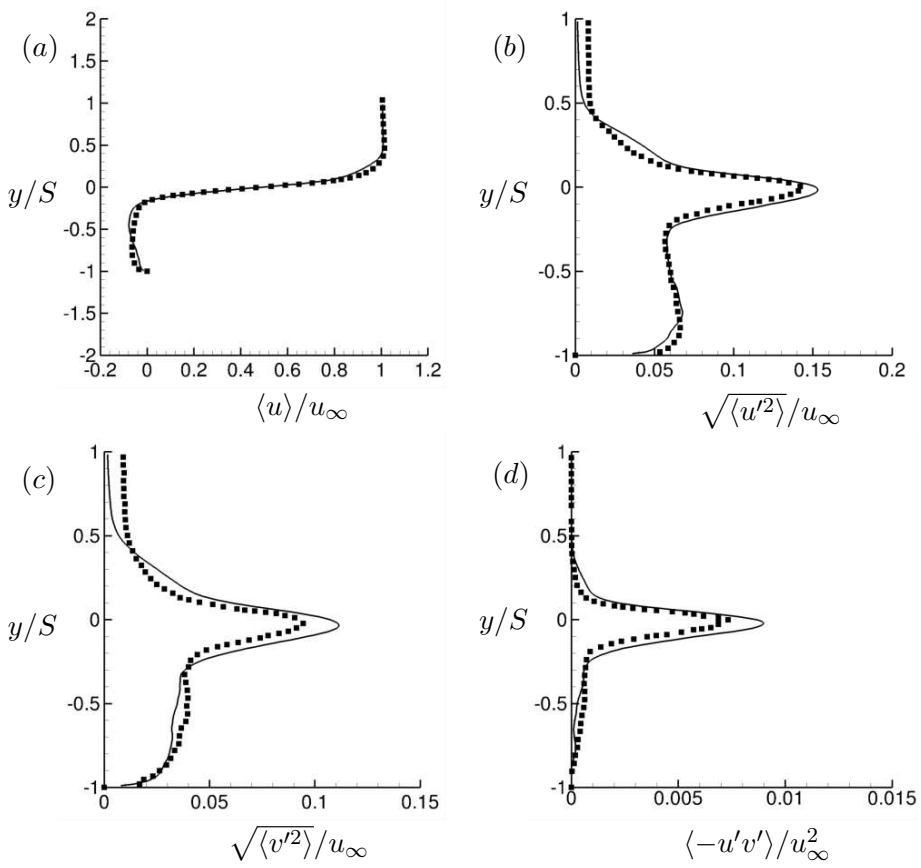

Figure 4.7: Comparison between numerical (lines) and experimental (symbols) profiles of mean velocity and Reynolds stresses for $Re_\tau = 1500$ at $x = 1S$ downstream of the step. S represents the step height. The experimental values are obtained from the work of Agarwal et al. [4].

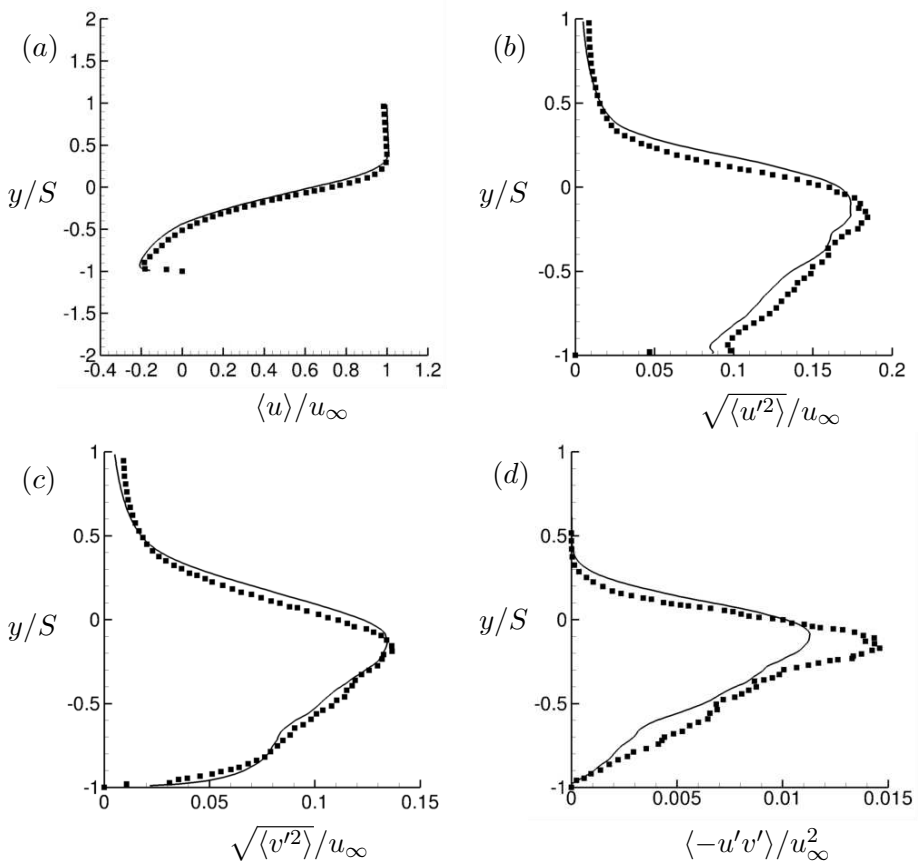

Figure 4.8: Comparison between numerical (lines) and experimental (symbols) profiles of mean velocity and Reynolds stresses for $Re_\tau = 1500$ at $x = 3S$ downstream of the step. S represents the step height. The experimental values are obtained from the work of Agarwal et al. [4].

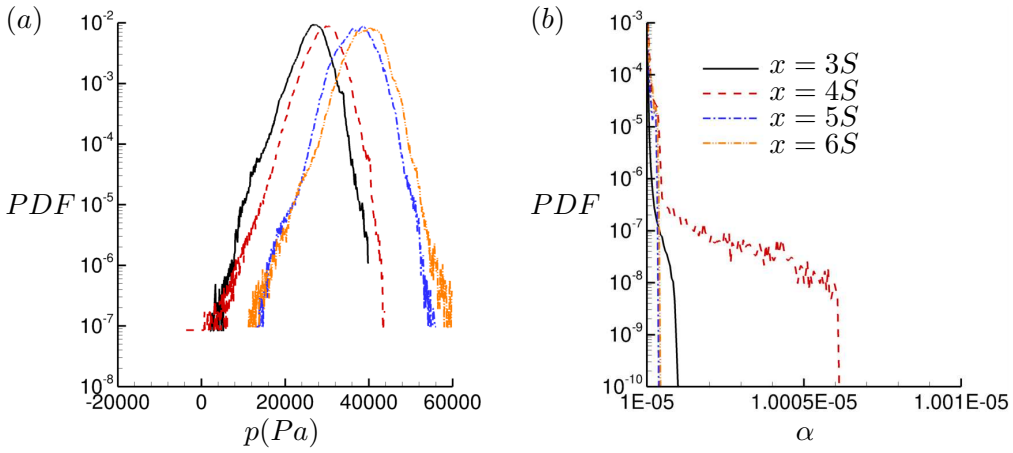

Figure 4.9: Probability density function of pressure (a) and volume fraction (b) at different axial location for $\sigma = 0.55$. The y–axis in (b) is clipped at 10^{-10} for better visualization.

inception conditions. The stations at $x = 3S$ and $x = 4S$, for instance, have PDF curves for pressure showing similar probability for vapor pressure but their probabilities for volume fraction are orders of magnitude apart. This indicates the effects of finite rate evaporation and condensation. Regions at vapor pressure need to be sustained for a finite amount of time to allow for the growth of vapor to more visible sizes. Figure 4.9(a) and (b) show that, for $\sigma = 0.55$, the cavitation process starts at $x = 3S$ and the vapor grows slowly as it is advected following the low–pressure regions to $x = 4S$. Over this distance of one step height, the PDF of void fraction reveals that vapor, most likely, only grows by 0.05%. This very small increase may imply that these incipient structures that start forming at $x = 3S$ do not remain at vapor pressure for their entire travel to $x = 4S$. As the vapor is advected further to $x = 5S$, it is condensed back to freestream levels due to a pressure recovery as shown by the PDFs. Additionally, figure 4.9(a) exposes how violent the pressure fluctuations can be in such flows. Observe how the most likely value for pressure obtained between $x = 3S$ and $x = 4S$ lies around $25kPa$. The tails of the curves, however, suggest that pressure can go as low as vapor pressure. These drastic fluctuations were also noticed in O'Hern [2] and help to clarify why inception can be seen in a shear flow at a relatively high ambient pressure.

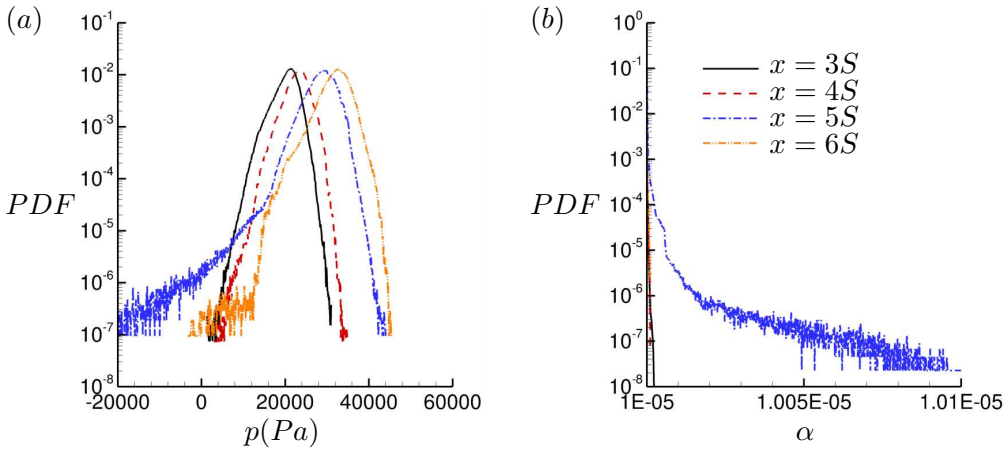

Figure 4.10: Probability density function of pressure (a) and volume fraction (b) at different axial location for $\sigma = 0.55$. The y–axis in (b) is clipped at 10^{-10} for better visualization.

The PDFs of pressure and volume fraction are also computed for $\sigma = 0.45$ and are displayed in figure 4.10. For all locations, the curves in figure 4.10(a) show a peak probability at a lower value of pressure than those obtained for $\sigma = 0.55$ in figure 4.9(a), as expected. It can also be observed that there is a higher probability of finding larger volumes of vapor, which is also foreseen. Note that all stations exhibit some probability of having regions at vapor pressure or lower, in contrast to $\sigma = 0.55$. Similar to $\sigma = 0.55$, the magnitude of the most likely observed pressure increases with axial distance from the step. However, in contrast to $\sigma = 0.55$, the location with a higher likelihood of finding vapor matches the location most likely to experience very low pressure. Note how the tail of the pressure PDF curves show that violent pressure fluctuations are seen at $x = 5S$. These extremely low values of pressure increase the evaporation rates, which are responsible for the explosive growth obtained at the same location.

The inception event rates at $\sigma = 0.55$ and $\sigma = 0.45$ are computed and displayed in figures 4.11(a) and (b) respectively. These events are obtained by counting the number of events with $p \leq p_v$ across the shear layer over two entire flow-throughs and averaging them over the span direction. The decrease in cavitation number from 0.55 to 0.45 is found to increase the inception activity by around $O(1)$. It can be observed that most

of the captured structures are located between $0.4 < x/L_r < 0.8$, consistent with the experimental data of Agarwal et al. [4]. For $\sigma = 0.45$, however, some structures are also detected at a considerable frequency downstream of the experimental range, compatible with the PDF curves of figure 4.10. Furthermore, it can be noted that although these incipient structures are scattered throughout the shear layer for $\sigma = 0.55$, they cover small continuous regions in an axial direction indicating that they only cavitate for very brief periods.

Although figures 4.9 and 4.10 show the likelihood of low pressure in some regions, they do not indicate the most probable cavitating pressure. This information is provided in figure 4.12 for both cases. These curves indicate that the most plausible cavitating pressure is around $-1500Pa$ for $\sigma = 0.55$ and $-5500Pa$ for $\sigma = 0.45$. Since both cases are performed for the same Re_τ, the drop in the inflow cavitation number was obtained by dropping inflow pressure by 17%. This small drop in inflow pressure changes the magnitude of the most likely cavitating pressure by around 3.5×. As it will be demonstrated in the next section, these pressure minima are found to be located inside the cores of the stretched streamwise vortices.

Flow topology of incipient structures

O'Hern [2] found that inception would primarily occur in the elongated quasi–streamwise vortices (QSV), indicating that the lowest values of pressure are expected to be in the core of these vortices. In this work, we examine the incipient structures by studying their flow topology based on the invariants of the velocity gradient tensor, strain rate tensor and rotation rate tensor. Chong et al. [122], Cantwell [123] and Perry and Chong [124] discuss the details of this approach; only a summary of the invariants and their physical meaning will be given here. The velocity gradient tensor, $A_{ij} = \frac{\partial u_i}{\partial x_j}$, has the following characteristic equation:

$$\lambda_i^3 + P\lambda_i^2 + Q\lambda_i + R = 0, \tag{4.1}$$

where λ_i are the eigenvalues and P, Q and R are the first, second and third invariants

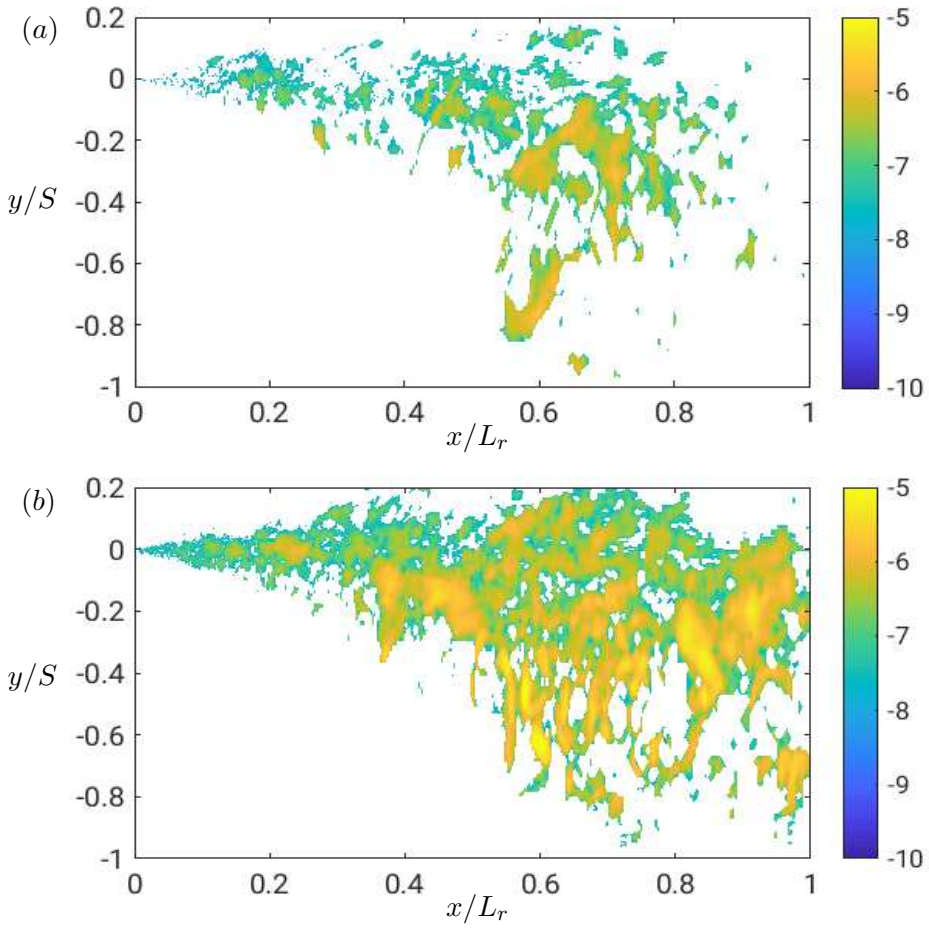

Figure 4.11: Inception event rates for $\sigma = 0.55$ (a) and $\sigma = 0.45$ (b). Levels in both plots are in logarithmic scale.

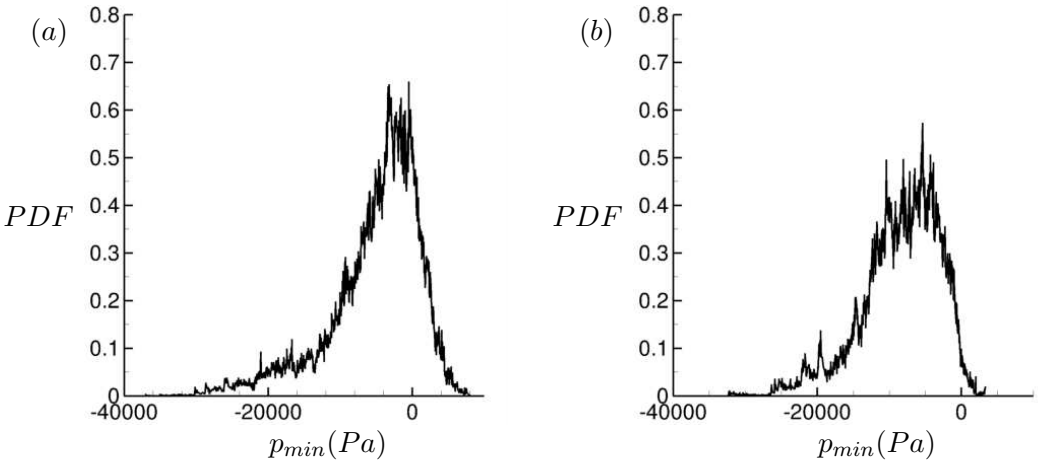

Figure 4.12: Probability density function of minimum pressure for $\sigma = 0.55$ (a) and $\sigma = 0.45$ (b).

of A_{ij}, respectively. These invariants are given by

$$\begin{aligned} P &= -S_{ii}, \\ Q &= \frac{1}{2}(P^2 - S_{ij}S_{ji} - \Omega_{ij}\Omega_{ji}), \\ R &= \frac{1}{3}(-P^3 + 3PQ - S_{ij}S_{jk}S_{ki} - 3\Omega_{ij}\Omega_{jk}S_{ki}). \end{aligned} \tag{4.2}$$

Here, $S_{ij} = \frac{A_{ij}+A_{ji}}{2}$ and $\Omega_{ij} = \frac{A_{ij}-A_{ji}}{2}$ are the strain rate tensor and rotation rate tensor, respectively. $P = 0$ due to incompressibility. Likewise, the invariants of S_{ij} and Ω_{ij} are defined by their respective characteristic equation. For incompressible flows, only the second and third invariants of S_{ij} and the second invariant of Ω_{ij} are non–zero. They are given by the following expressions:

$$Q_s = -\frac{1}{2}S_{ij}S_{ji}, \quad R_s = -\frac{1}{3}S_{ij}S_{jk}S_{ki} \quad \text{and} \quad Q_w = -\frac{1}{2}\Omega_{ij}\Omega_{ji}, \tag{4.3}$$

where the subscripts S and w indicate that the variable is related to the strain rate tensor and rotation rate tensor, respectively.

Figure 4.13(a) shows the topologies in the Q–R plane. The tent–like curve depicts $D = 0$, where D is the discriminant of A_{ij} given by $D = \frac{27}{4}R^2 + Q^3$. Fluid elements

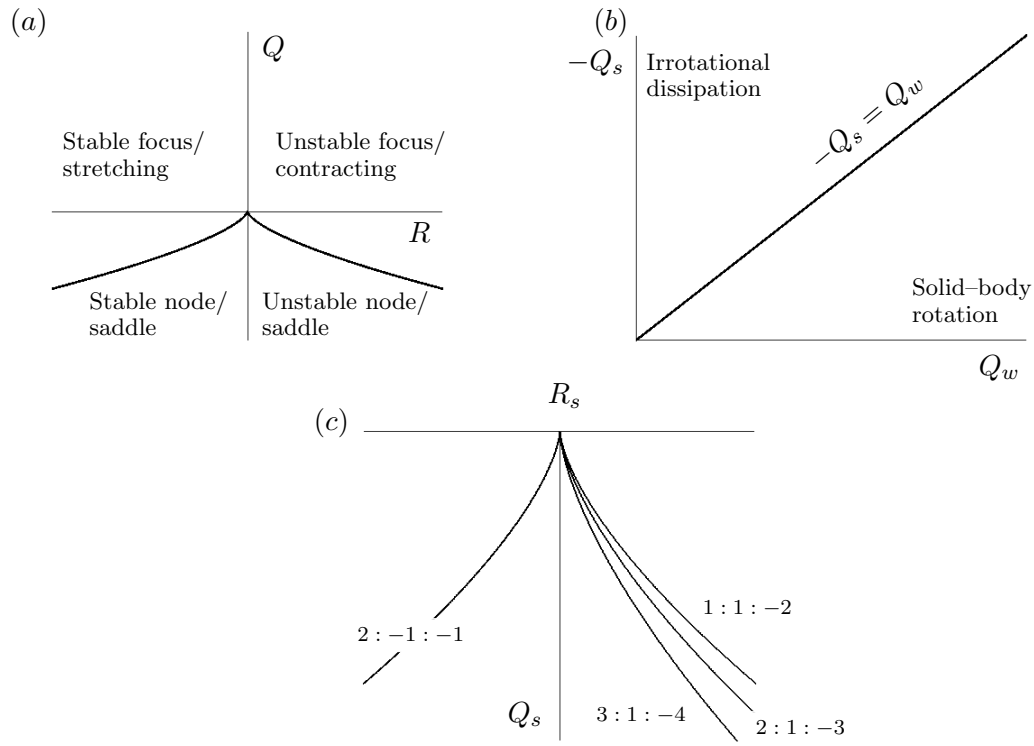

Figure 4.13: The regions formed by the second and third invariants of the velocity gradient tensor (Q–R) and the regions formed by the second invariants of the strain rate tensor and rotation rate tensor (Q_s–Q_w) are given in (a) and (b) respectively with their corresponding flow patterns. Curves representing the ratio between the principal strain rates are shown in the Q_s–R_s plane in (c).

occupying the region of $D > 0$ are focal regions and can be undergoing stretching ($R < 0$) or contraction ($R > 0$). According to Ooi et al. [125], the focal structures with stretching topology are in general elongated and compact in a tube–like shape, while the contracting regions resemble 'blobs' and are usually found at the ends of the focal structure or at the intersection between two stretching regions. Figure 4.13(b) shows the physical interpretation for the Q_s–Q_w plane. Regions of the flow lying below the $Q_w = -Q_s$ line are dominated by rotation (such as the core of a vortex tube) while regions lying above the line are dominated by strain (such as the periphery of a vortex tube) with intense kinetic energy dissipation. The third invariant of the strain rate tensor (R_s) is proportional to the strain skewness and it can be demonstrated that $R_s = -\lambda_1\lambda_2\lambda_3$ [126], where $\lambda_1 > \lambda_2 > \lambda_3$ are the eigenvalues of S_{ij} and $\lambda_1 + \lambda_2 + \lambda_3 = 0$ due to incompressibility. Thus, the Q_s–R_s plane is useful to investigate the geometry of the local straining of a fluid particle. Curves representing the ratio between the principal strain rates $\lambda_1 : \lambda_2 : \lambda_3$ are shown in figure 4.13(c), where each of them indicates a flow geometry (e.g. $1 : 1 : -2$ indicates axisymmetric stretching while $2 : -1 : -1$ corresponds to axisymmetric contraction). For more details, the reader is referred to Perry and Chong [124].

We collect the values of these invariants over time for the regions where the local pressure is lower than vapor pressure and compute their joint–PDFs in the Q–R, Q_s–Q_w and Q_s–R_s planes. The joint–PDFs, however, do not indicate whether these vortices are in the streamwise direction. The work of Agarwal et al. [52] identifies the quasi–streamwise vortices by the threshold of $\sqrt{\omega_x^2 + \omega_y^2}/(u_\infty/S) > 3.5$, where ω_x and ω_y are the streamwise and vertical components of the vorticity, respectively. The PDF of this quantity is presented in figure 4.14(a) while figure 4.14(b) displays the probabilities for the angles between the vorticity vector and the velocity components, for the regions where the local pressure is lower than vapor pressure. It becomes evident that the obtained incipient structures are QSVs.

The joint–PDFs for the invariants for $\sigma = 0.55$ are shown in figure 4.15(a), (b) and (c) respectively. The results for $\sigma = 0.45$ are similar and are, therefore, not presented here. The joint-PDF of Q–R in figure 4.15(a) reveals that pressure drops below vapor

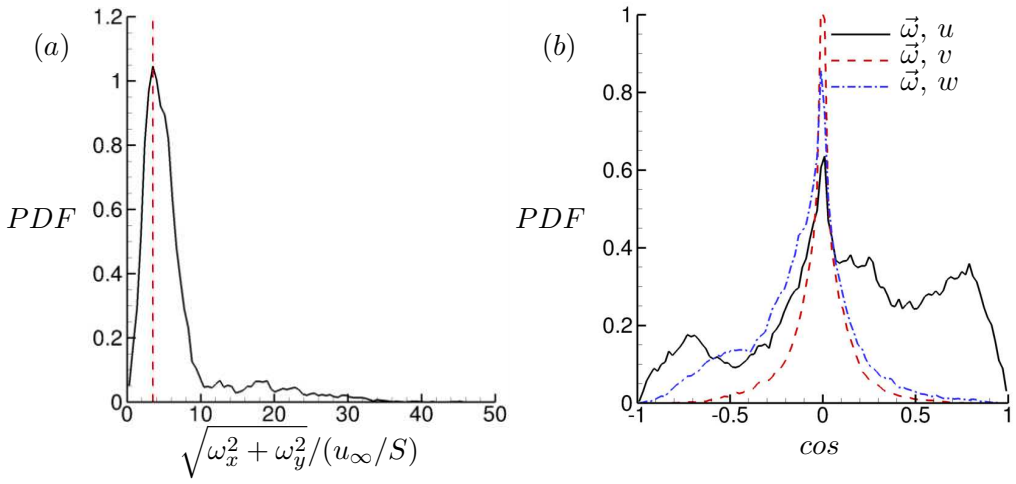

Figure 4.14: PDFs of vorticity magnitude (a) and angle between vorticity vector and the velocity components (b). The red dashed line in (a) indicates $\sqrt{\omega_x^2 + \omega_y^2}/(u_\infty/S) = 3.5$.

pressure primarily in focal regions. The joint-PDF in figure 4.15(b) shows that these events are likely to be dominated by rotation. This reinforces the suggestion of O'Hern [2]. According to figure 4.15(c), these focal incipient structures show a tendency to have strain rate ratios of $2:1:-3$ or $3:1:-4$. In other words, this means that inception likely occurs in focal structures that are being elongated 2 or 3$\times$ more in their most extensive principal direction than in their intermediate principal direction. Figure 4.16 shows a visual example of these structures. Isocontour of $p = p_v$ is given in orange and isocontour of $\alpha = 1.005 \times 10^{-5}$ is given in blue. The presence of multiple locations with a pressure equal to or less than vapor pressure in the shear layer can be observed, however, the largest structure is stretched in the streamwise direction. The isocontour of vapor volume fraction confirms that this structure cavitates first, which agrees with experimental observations.

Figure 4.15(b) showed that regions of higher rotation rates are preferential sites for inception. However, it does not quantify the balance between rotation and straining. The kinematical vorticity number is often employed as a quantitative measurement of

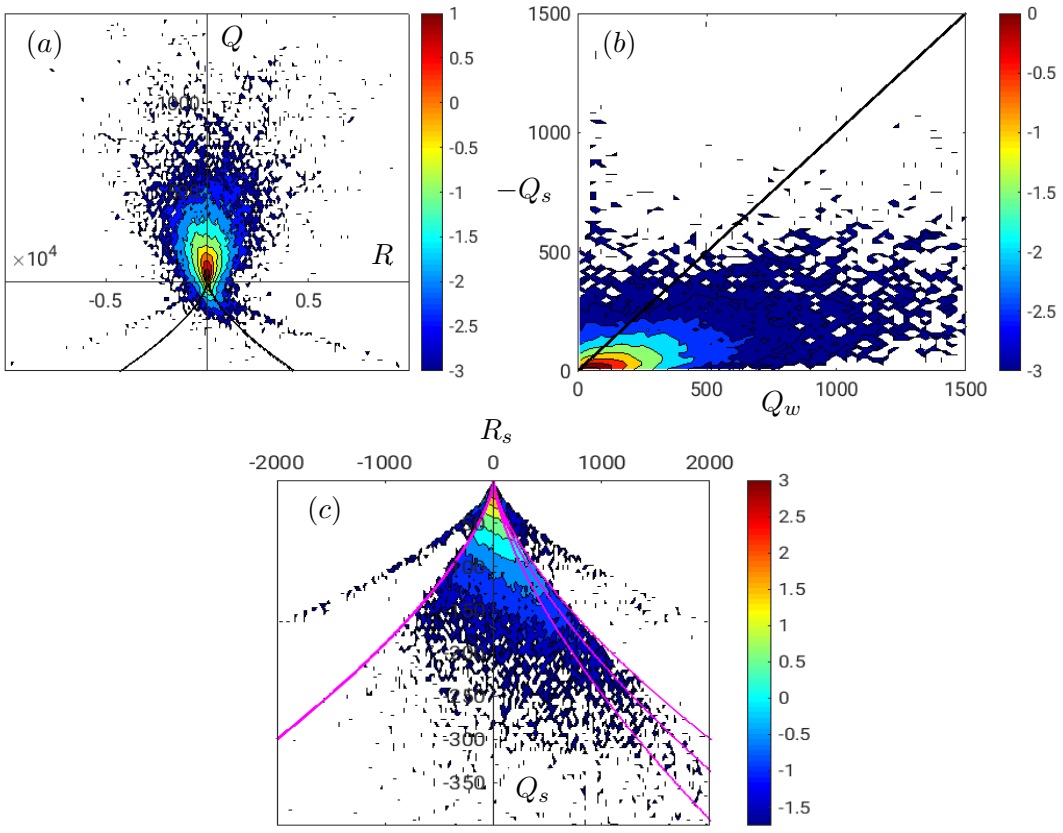

Figure 4.15: Joint–PDFs of Q–R (a), Q_s–Q_w (b) and Q_s–R_s (c) plot for $\sigma = 0.55$. Levels in both plots are in logarithmic scale and the invariants are in non–dimensional units (using the appropriate combination of the step height, S, and the freestream velocity, u_∞).

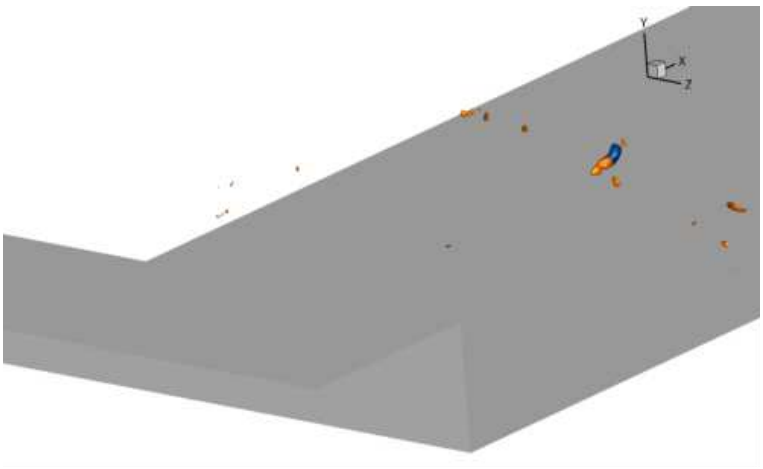

Figure 4.16: Isocontours of $p = p_v$ in orange and $\alpha = 1.005 \times 10^5$ in blue.

the amount of rotation of a fluid particle [127], and is defined as

$$\kappa = \left(\frac{Q_w}{-Q_s} \right)^{\frac{1}{2}}. \tag{4.4}$$

This variable measures the ratio between rotational strength and irrotational stretching [125]. A value of $\kappa = 0$ implies that a fluid particle is undergoing purely irrotational stretching while a value of $\kappa = \infty$ means that the fluid particle is subjected only to solid–body rotation. The joint–PDF between pressure and κ is displayed in figure 5.24 and reveals a predominance of $\kappa \approx 2$, which means that inception is most likely to occur in the cores of vortex tubes subjected to a rotation rate $4\times$ stronger than the stretching rate. Additionally, a decreasing pressure and consequently the likelihood of cavitation is found to be correlated to an increasing κ.

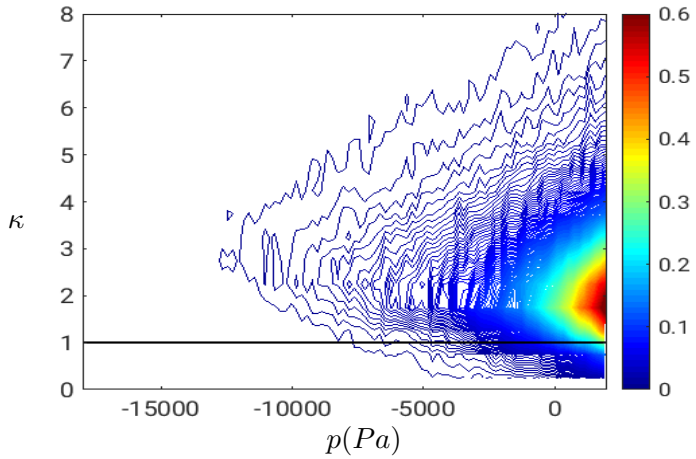

Figure 4.17: Joint–PDF between pressure and κ for $\sigma = 0.55$. The line of $\kappa = 1$ signals the boundary between stretching to rotation dominated.

Chapter 5

Towards a polydisperse model for the inception regime

The objective of this chapter is to present the development of a polydisperse model for the inception regime, and to use it to study inception in the tip vortex of an elliptic hydrofoil.

This chapter is organized as follows. The physical model is presented in section 5.1, and a validation/verification study is shown in section 5.2. The geometry of the hydrofoil and boundary conditions for the problem are given in section 5.3. A detailed analysis of the results is provided in section 5.4.

5.1 Physical model

As previously mentioned, cavitation inception is usually detected by visual observations when bubbles grow larger than a certain size. One limitation from the model presented in section 2.2 is that the volume fraction is the only variable that quantifies the amount of vapor. However, large volume fractions do not necessarily translate into large bubbles. An obvious approach would be to apply an Euler–Lagrange method where millions of bubbles are injected and tracked individually, however the computational cost would

be prohibitively expensive for large scale problems. An alternative more computationally attractive is to use polydisperse models (also called population balance models). Historically, these models have been applied in many applications used in the chemical process industry such as bubble columns, fluidized beds and flame reactors [128, 129]. More recently, they started been employed into marine application [130, 131], but still with a very limited focus on cavitation [132, 133].

The population balance equation is a balance equation based that accounts for the spatial and temporal evolution of the number density function in a single control volume. The general form of the equation is given as

$$\frac{\partial f(m, \overrightarrow{x}, t)}{\partial t} + \frac{\partial}{\partial x_j} \left(f(m, \overrightarrow{x}, t) u_j \right) = RHS(m, \overrightarrow{x}, t), \tag{5.1}$$

where $f(m, \overrightarrow{x}, t)$ is the bubble size distribution function and represents the probable number of bubbles with mass in the range $(m, m + dm)$. The right–hand side of the equation accounts for breakage, coalescence and evaporation/condensation. The population balance equation is often solved with the discrete method or with the method of moments. In the discrete method (also called the multi–group method), the disperse population is discretized into a finite number of size intervals or bins, that can share the same velocity or not. An example is given in figure 5.1 where the bins account for different bubbles radii. For the method of moments, the population balance equation is transformed into a set of transport equations for moments of the distribution. Typically, the zeroth moment represents the total number density, the second moment represents the total surface area per unit volume, and the third moment represents the total mass density. Since we are interested in the inception regime, the multi–group approach is used here with the same passive scalar framework as the one given in section 2.2. Integrating equation (5.1) in the range $(m_{k-1/2}, m_{k+1/2})$ and ignoring the bubble coalescence and breakup terms, a transport equation for the bubble number density N_k for each group k is given as [130]

$$\frac{\partial N_k}{\partial t} + \frac{\partial N_k u_j}{\partial x_j} = \frac{\dot{m}_{k-1/2}}{m_k - m_{k-1}} N_{k-1/2} - \frac{\dot{m}_{k+1/2}}{m_{k+1} - m_k} N_{k+1/2}, \tag{5.2}$$

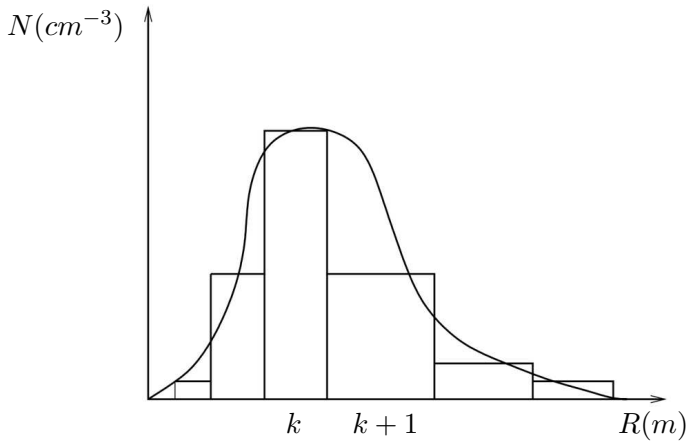

Figure 5.1: Example of a distribution of bubbles of different sizes.

where $\dot{m}_{k\pm1/2}$ is the mass transfer term between adjacent bins. The volume fraction of each bin can be written as $\alpha_k = N_k \frac{4\pi {R_k}^3}{3}$, where R_k is the radius of the bubbles in bin k, thus equation (5.2) can be rewritten as

$$\frac{\partial \rho_v \alpha_k}{\partial t} + \frac{\partial \rho_v \alpha_k u_j}{\partial x_j} = \frac{\dot{m}_{k-1/2}}{m_k - m_{k-1}} N_{k-1/2} \rho_v V_{bk} - \frac{\dot{m}_{k+1/2}}{m_{k+1} - m_k} N_{k+1/2} \rho_v V_{bk}. \tag{5.3}$$

Here, ρ_v is the vapor density, which is assumed constant, and $V_{bk} = \frac{4\pi {R_k}^3}{3}$. The mass transfer term is based on the asymptotic solution of the Rayleigh–Plesset equation and is given by

$$\dot{m}_{k\pm1/2} = 4\pi \rho_v {R^2}_{k\pm1/2} sign(p_v - p) \sqrt{\frac{2}{3} \frac{|p_v - p|}{\rho_l}}, \tag{5.4}$$

where the vapor pressure is also given in equation (2.10). $N_{k\pm1/2}$ is the bubble number density at the edge between bins, which here is taken as the average between N_k and $N_{k\pm1}$, although high order methods are recommended [130], and $R_{k\pm1/2}$ is the limiting radius between adjacent bins. It is evident from equation (5.3) that the amount of vapor in a bin is determined by the mass transfer between its adjacent bins and that the mass transfer between bins cancel each other out such that mass is conserved. Thus for the

last bin, $\dot{m}_{k+1/2} = 0$.

Given that the present model is a extension of the one presented in section 2.2, the numerical algorithm is taken from subsection 2.2.2. The source terms, however, are treated explicitly. A brief validation is given next in section 5.2. The model is then used in a study of inception in the tip vortex of a elliptic hydrofoil in section 5.3.

5.2 Validation

The method described here is a extension of the work presented in section 2.2 where vapor is treated as a passive scalar. The extension consists in replacing the overall continuous amount of vapor by its distribution into bins of different sizes. Therefore, the total amount of vapor void fraction predicted by the polydisperse method should approximate the vapor void fraction predicted by the approach of section 2.2. The source term given in equations (5.3) and (5.4), however, can not be employed in this comparison since it needs information about the bubble radius and the bubble number density. Therefore, for this verification, we employ a source term that depends only on the void fraction and pressure difference, and was developed by Saito et al. [41]. The source term is then written as

$$... = \dot{m}_{k-1/2} - \dot{m}_{k+1/2} + \dot{m}_k, \tag{5.5}$$

where

$$\begin{aligned}
\dot{m}_{k-1/2} &= C_e {\alpha_{k-1}}^2 {\alpha_k}^2 \frac{\rho_l}{\rho_v} \frac{max(p_v - p, 0)}{\sqrt{2\pi R_v T}} - C_c {\alpha_{k-1}}^2 {\alpha_k}^2 \frac{max(p - p_v, 0)}{\sqrt{2\pi R_v T}}, \\
\dot{m}_{k+1/2} &= C_e {\alpha_{k+1}}^2 {\alpha_k}^2 \frac{\rho_l}{\rho_v} \frac{max(p_v - p, 0)}{\sqrt{2\pi R_v T}} - C_c {\alpha_{k+1}}^2 {\alpha_k}^2 \frac{max(p - p_v, 0)}{\sqrt{2\pi R_v T}}, \\
\dot{m}_k &= C_e {\alpha_l}^2 {\alpha_k}^2 \frac{\rho_l}{\rho_v} \frac{max(p_v - p, 0)}{\sqrt{2\pi R_v T}} - C_c {\alpha_l}^2 {\alpha_k}^2 \frac{max(p - p_v, 0)}{\sqrt{2\pi R_v T}}.
\end{aligned} \tag{5.6}$$

Here, the term $\dot{m}_k$ is added such that the sum of the source term over all the bins is equal to the expression used in section 2.2. The term α_l is the liquid volume fraction

$(\alpha_l = 1 - \sum_{k=1}^{M} \alpha_k)$.

The problem used for the validation here is different from the main problem investigated in the next section to lower computational costs. This simple problem is taken to be a flow over a circular cylinder under incipient conditions at low Reynolds number ($Re = 200$ based on cylinder diameter) and at $\sigma = 1.5$. This canonical problem has been investigated before in large–scale cavitation regimes [44]. The cylinder is placed at the center of a $40 \times 20 \times 1$ rectangular computational domain, as given in figure 5.3(a). The mesh spacing considered near the cylinder surface is $0.02D$ in both radial and azimuthal directions, which stretches further away. No–slip boundary conditions are applied to the bottom and top walls of the domain, while the spanwise walls have periodic boundary conditions. The very low Re used in this comparison results in a two–dimensional flow, thus 3 points are used in the spanwise direction. Here we compare the solutions obtained when the polydisperse model is used (equation (5.3)) and when it is not used (equation (2.37)). A total of 8 bins are used to represent bubbles of sizes ranging from $0.5\mu m$ to $5mm$. The vapor distribution at the inflow is given in figure 5.2, which adds up to a total vapor volume fraction of 1.85×10^{-4}. Figures 5.3(b) and 5.3(c) show mean total void fraction contours when the polydisperse model is used and when it is not used, respectively, and figure 5.4 shows mean and fluctuation values of volume fraction across the wake centerline. It can be seen that, overall, the solution obtained with the polydisperse model has a good agreement with the solution obtained with the other model (equation (2.37)). However, it predicts a slightly smaller amount of total vapor.

5.3 Large–eddy simulation of a elliptic hydrofoil tip vortex cavitation at incipient condition

5.3.1 Introduction

The goals of this section are: (i) to demonstrate the capability of LES to simulate the complex flow field, and (ii) to study the tip vortex cavitation under different conditions.

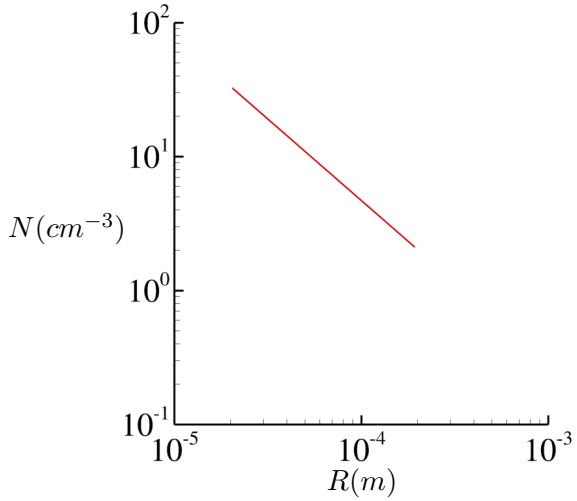

Figure 5.2: Bubble distribution at inflow for the validation problem.

5.3.2 Problem Setup

The problem setup closely resembles the reference experiments of Boulon et al. [70]. The hydrofoil has a NACA 16–020 cross-section and an elliptical planform of span $S = 0.18\ m$, a root chord length $c = 0.12\ m$ and the aspect ratio is 3.8. The hydrofoil is mounted such that the mid point of the root chord of the hydrofoil is the origin of the Cartesian coordinate system and the tip is located at $(0, -S, 0)$. The hydrofoil span aligns with the y axis and x is the downstream streamwise direction. The two side walls are located at $z = \pm L_z/2$, where $L_z = 0.175$. Note that one grid unit is equivalent to $1m$ length in the reference experiment. Hence, the tip–gap $e = 0.06$ which corresponds to the experimental setup of $e = 60\ mm$, is generally chosen as the reference case corresponding to no confinement due to the bottom wall. As stated in the reference paper, the two side walls cause confinement resulting in a 27% increase of lift. The Re based on c and U_∞ are 9×10^5 and 1.4×10^6, and the hydrofoil is rotated about y to make an angle of attack of 12 degrees. The inflow and outflow planes are located at $L_{up} = 2.58c$ upstream and $L_{dn} = 4.92c$ downstream of the tip respectively. The schematic of the computational domain is shown in figure 5.5.

Free–stream velocity is prescribed at the inflow and convective boundary conditions

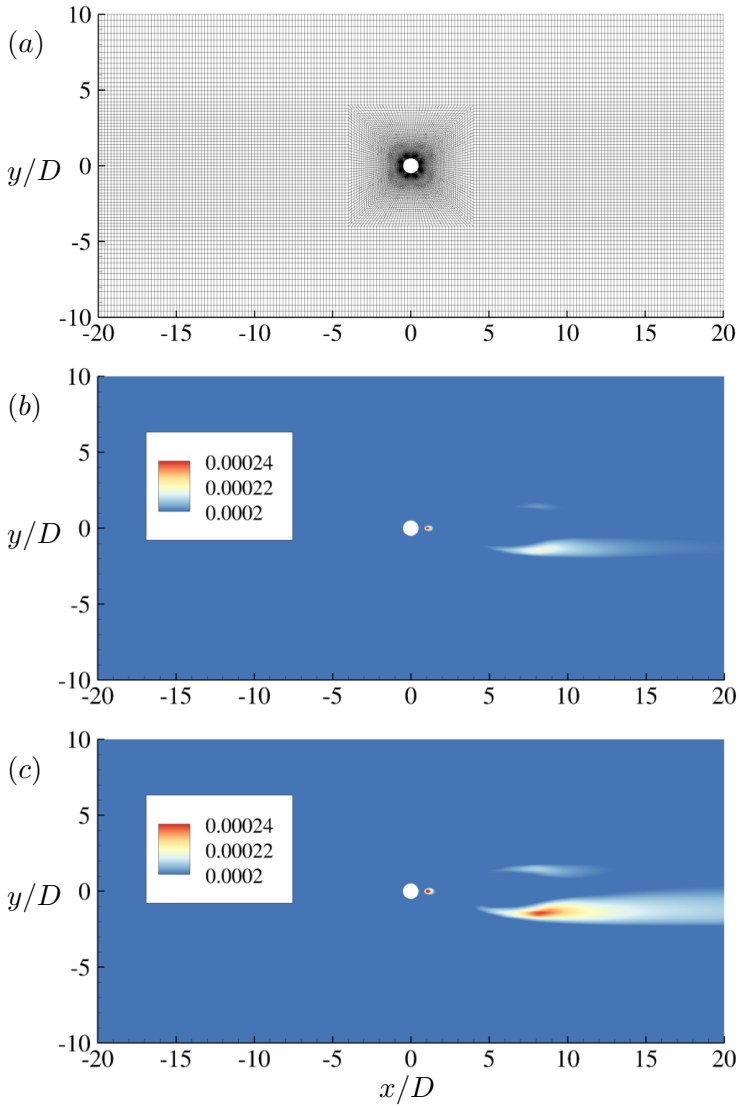

Figure 5.3: Computational domains (a). Mean values of total vapor volume fraction when the polydisperse model is employed (b) and when it is not (c).

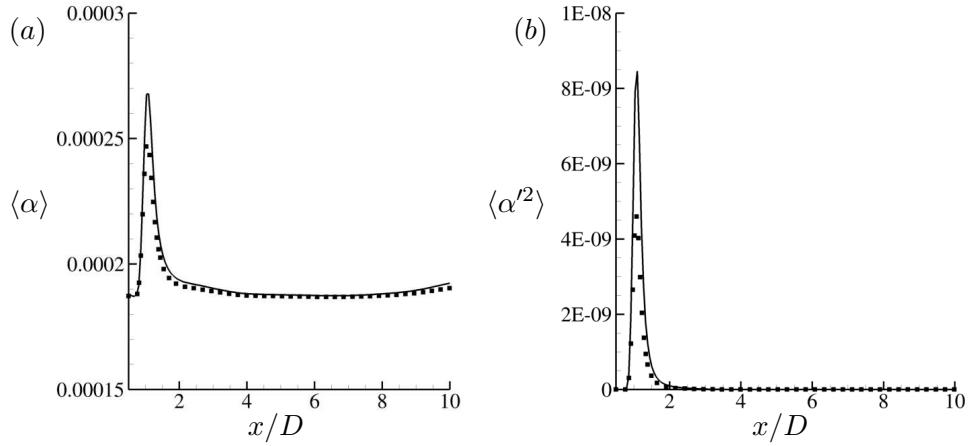

Figure 5.4: Profiles of $\langle\alpha\rangle$ (a) and $\langle\alpha'^2\rangle$ (b) when the polydisperse model is used (symbols) and when it is not used (lines).

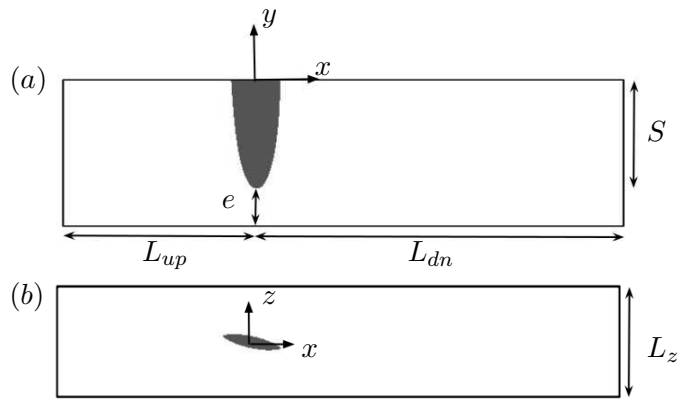

Figure 5.5: Schematic of the computational domain shown in $z = 0$ (a) and $y = 0.1$ (b) planes.

are applied at the outflow. All other domain boundaries have no–slip boundary conditions. A coarse grid (not shown here) of 14 million hexahedral control volumes is first used to access grid resolution and obtain a solution which is used to initialize a fine grid simulation containing 44 million hexahedral control volumes, which is nominally two times finer in each direction compared to the coarse grid in the near field everywhere except near wall (no–slip) boundaries. The span of the hydrofoil has more than 260 cells and there are more than 400 cells in z direction for the fine grid. The gap between tip of the hydrofoil and the bottom wall contains more than 80 cells. The tip vortex is resolved over more than 20 cells, which is in line with the simulations of hydrofoil tip vortex by Hsiao and Pauley [134]. The grid is clustered near all the wall boundaries with a nominal wall–normal first cell size of $8.3 \times 10^{-4}c$ and $1.67 \times 10^{-3}c$ at hydrofoil surface and other walls respectively with a growth rate of one percent. All the results presented in this paper are normalized appropriately using U_∞ and c, except when the units are explicitly mentioned. The flow is taken to be at room temperature, which yields $p_v \approx 2kPa$.

We assume the bubble distribution ranges from $0.5\mu m$ to $5mm$ and it is divided into 8 bins. The amount of vapor prescribed at the inflow follows the conditions from the water tunnel at the Australian Maritime College investigated in the work of Khoo et al. [57]. Two distributions are studied, named as "natural" and "seeded", corresponding to conditions where the water is poor and rich in nuclei respectively. They are shown in figure 5.6. It is important to mention that the water can also be called as "strong" or "weak", depending whether the flow is poor or rich in nuclei, respectively. Those distributions yield an overall inflow vapor void fraction of $\alpha \approx 6.1 \times 10^{-15}$ and 1.85×10^{-4} for the natural and seeded cases respectively. The cavitation number is chosen to be $\sigma = 2.1$, which is the critical value reported by Boulon et al. [70] for the angle of attack and confinement value used in the present work. It is important to mention that the critical cavitation number is defined in Boulon et al. [70] as the value at which the vapor core attaches to the tip. Thus, the critical σ is lower than the inception σ, which is the value at which the first instance of cavitation is observed.

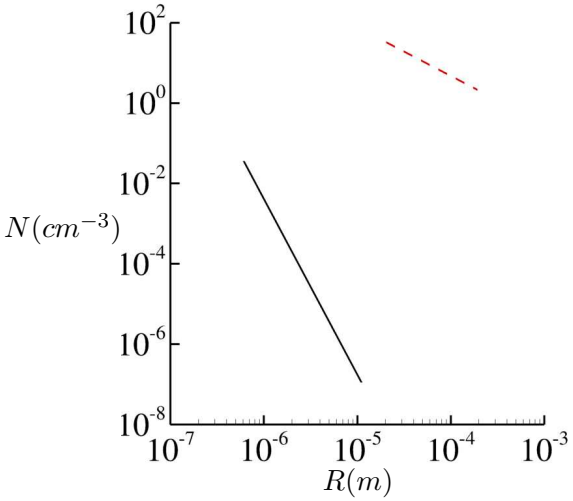

Figure 5.6: Bubble distribution at inflow for natural (——) and seeded cases (----).

5.3.3 Comparison to experiments

Before comparing the results with the experimental data, a discussion on the experimental setup is necessary. Boulon et al. [70] performed the reference experiments. They could vary Re from 3.6×10^5 to 1.4×10^6 in their hydrodynamic tunnel by varying U_∞ from 3 to 12 m/s. Their tunnel had a free–stream turbulence of 1.5 % with empty test section. Most of their experiments were conducted at $U_\infty = 7\ m/s$, which corresponds to $Re = 9 \times 10^5$. For example, they showed images (their figure 4) visualizing tip vortex cavitation at different tip gaps at the same U_∞ and an angle of attack $\alpha = 12°$. Hence, $\alpha = 12°$ was chosen as the angle of attack for the simulations. However, the measurements of the velocity profiles in the wake at a range of tip gaps were only reported at the same α but a lower $U_\infty = 5\ m/s$. Assuming the other quantities remained unchanged, this U_∞ in the tunnel would make $Re \approx 6.4 \times 10^5$ for the experiments where the profile measurements were taken.

The strength of the tip vortex depends on the overall lift generated by the hydrofoil whereas its core size correlates with the boundary–layer thickness [67]. Billet and Holl [135] showed that for a variety of wing shapes and cross sections at Re greater than that corresponding to flat plate boundary–layer laminar–turbulent transition ($Re \approx 5 \times 10^5$),

the minimum pressure coefficient $C_{p,min}$ on the axis of the tip vortex (modeled as a Rankine vortex) scales as

$$C_{p,min} = kC_l^2 Re^{0.4}, \tag{5.7}$$

where k is a constant which depends on the foil and C_l is the lift coefficient. The present hydrofoil however, deviates from this behaviour [68]. Moreover, $C_{p,min}$ drops further below at lower Re due to a large change in C_l. This peculiar behaviour of the present hydrofoil makes it different than other hydrofoils and wings.

Pichon et al. [69] studied the effect of tripping the boundary–layer over the present hydrofoil on the tip vortex behaviour and showed that the tip vortex in the tripped boundary–layer case at $Re < 5.6 \times 10^5$ not only behaved like that generated by untripped hydrofoil at higher Re but also followed equation (5.7). This behaviour suggests complex dependence of the tip vortex on the hydrofoil boundary–layer which depends on both Re and α. Note that the transition $Re = 5.6 \times 10^5$ was for unconfined tip vortex. The presence of side and bottom walls can alter the transition Re by modifying the hydrofoil boundary–layer on either sides, thereby making the overall flow field highly sensitive to Re close to the transition value. Note that Boulon et al. [70] did not trip the hydrofoil boundary–layer and the reported profiles were measured at Re close to the transition Re. Due to these reasons, it is suspected that the hydrofoil boundary–layer in the reference experiments were not turbulent. In fact, we will see in section 5.4 that bulk of the flow on the hydrofoil appears laminar.

Ensuring grid independent behaviour of the present case is challenging. A coarse resolution on the hydrofoil can cause transition and separation of the hydrofoil boundary–layer, which will change both the strength and core thickness of the tip vortex. A coarse resolution in the wake can alter the streamwise evolution of tip vortex. The trailing edge vortex sheet comes close to the side–wall close to the pressure side of the hydrofoil. Therefore, the tip vortex–wall interactions mandates adequate resolution in that region as well. Moreover, lack of measurements on the hydrofoil surface in the experiments make it nearly impossible to determine the exact cause of mismatch, if at all present, between the simulation and the experiment. Therefore, the grid employed in the present

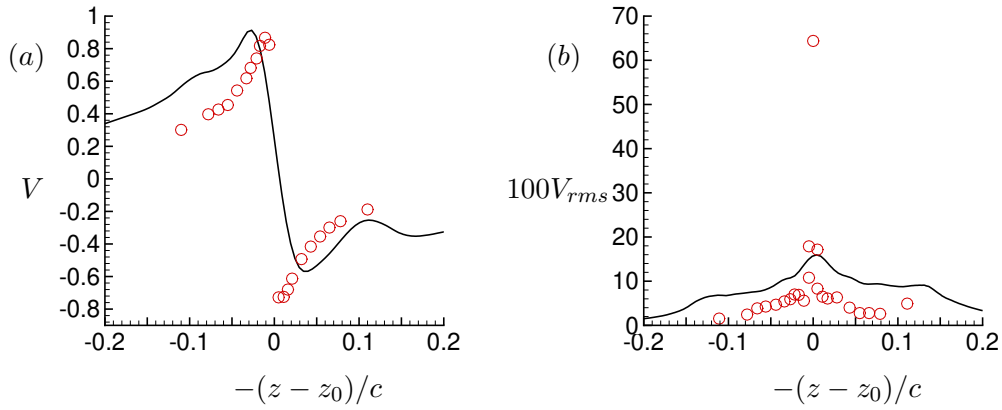

Figure 5.7: The LES results are compared to the experiments [70] for mean (V) (a) and r.m.s. (V_{rms}) (b) of vertical velocity at $x/c = 1$. Note that z_0 is the location of the tip vortex core on the horizontal line passing through it.

simulation has been carefully designed after gaining insights from numerous preliminary simulations, some of which are reported in Kumar and Mahesh [136]. Refining the grid further may make the hydrofoil wake match closer to the reference experiment, but is not pursued due to lack of hydrofoil boundary–layer data from the experiment.

The results are compared to the mean profiles of mean and root–mean–square (r.m.s) of vertical velocity at $x/c = 1$ available from the experiments in figure 5.7. Note that the results are plotted similar to that in the experiment. The results show good agreement with the experiment in light of the earlier discussion. Unfortunately, no other profile measurements were reported at these conditions.

5.4 Results

5.4.1 Overview of the flow field

The results presented in this subsection are obtained at $Re = 9\times10^5$. The instantaneous coherent vortical structures in the flow field are visualized using the isocontour of λ_2 [137] colored with pressure as shown in figure 5.8. Note that the bottom and side walls are removed for clear visualization. The incoming flow accelerates on the pressure side

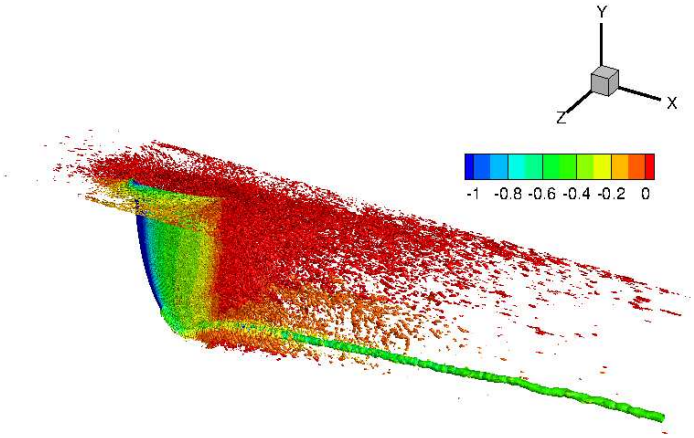

Figure 5.8: Isocontour of λ_2 coloured with pressure showing the trailing edge wake and the tip vortex. The bottom and side walls are removed for visualization.

and decelerates on the suction side of the hydrofoil. The pressure difference across the hydrofoil creates lift. The variation of local lift along the span causes vortex shedding at the trailing edge of the hydrofoil, forming a vortex sheet which terminates into a coherent tip vortex. The tip vortex can be seen as a coherent vortex originating near tip on the suction side, whose axis is aligned with the freestream (x) direction. The tip vortex appears coherent throughout the simulated domain. The vortical structures in the top wall boundary–layer and the junction flow near the root of the hydrofoil are also visible.

The instantaneous pressure, axial velocity and vorticity magnitude in $z = 0$ plane are shown in figure 5.9. The tip vortex is visible clearly as the region of low pressure and high vorticity. The pressure minimum at a given downstream location occurs in the tip vortex core and its magnitude decreases moving downstream. The streamwise velocity field shows shear layers in the wake, with a small region of flow separation near the trailing edge. Figure 5.9(c) shows that there are three main regions of high vorticity: the tip vortex, the trailing edge and the boundary layers on the no–slip boundaries. In order to have a closer look at the flow, a slice is extracted $y/c = -0.83$ and shown in

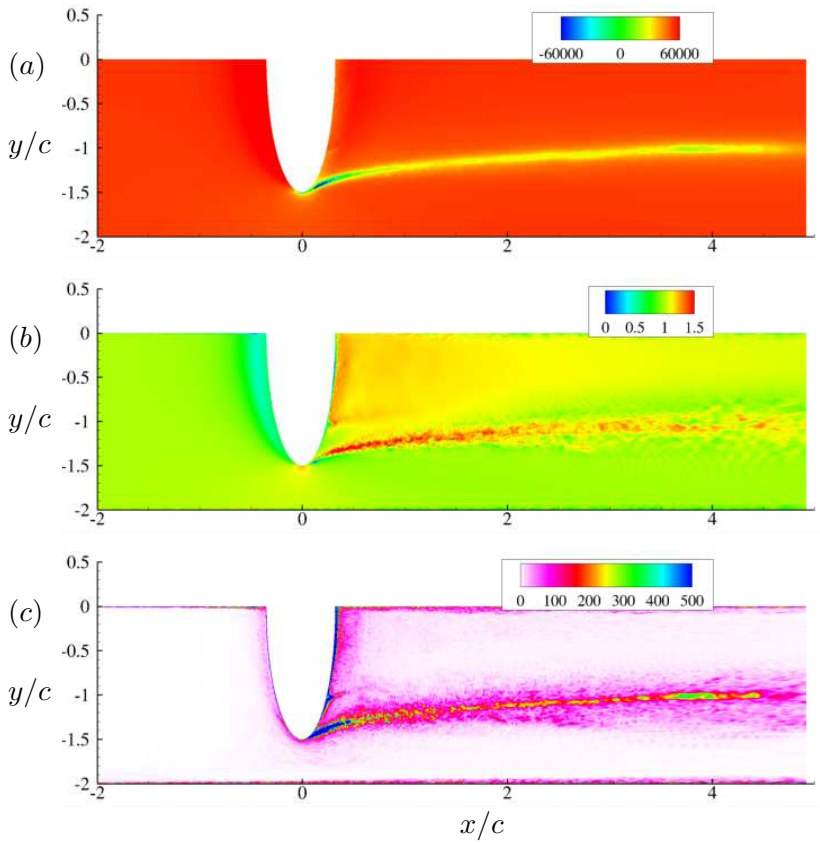

Figure 5.9: Instantaneous flow field showing pressure in Pa (a), streamwise velocity (b) and vorticity magnitude (c) in $z = 0$ plane.

figure 5.10. The flow appear attached everywhere except very close to trailing edge. The vorticity shed from the trailing edge forms a shear layer, which evolves downstream under the influence of side–walls. The velocity defect and vorticity magnitude in the wake decays moving downstream.

The instantaneous pressure and vorticity fields in the wake are shown at $x/c = 1$ in figure 5.11. The pressure variation from the ambient can be observed in the trailing vortex sheet and the tip vortex, with the tip vortex being the local pressure minimum. The overall wake appears as a line vortex terminating into a tip vortex, which undergoes the process of spiral roll–up in counterclockwise sense in the figure shown. The boundary–layers can be observed on all wall boundaries. The streamwise, vertical and horizontal components of instantaneous velocity are shown in figure 5.12. The velocity jumps across the shear layer are visible. Note the existence of high streamwise velocity near the axis of symmetry, which distinguishes the trailing edge vortices from other types of line vortices [138].

Figure 5.13 shows the mean velocity components in $z = 0$ plane. The shear layer appears to grow in the y direction in all the components moving downstream. The region in the vicinity of the tip has large magnitude of vertical velocity mainly due to the end effects where the flow tends to move from the pressure side to the suction side. The horizontal component of mean velocity shows the mean swirl of the axial tip vortex. The mean and root–mean–square values of pressure are given in figure 5.14. The mean minimum value of pressure is found to be in the vortex core very close to the hydrofoil tip, which is a region of high water tension (negative pressure). In addition, the entire tip vortex experiences very high levels of pressure fluctuation, which makes it susceptible for inception. Figure 5.15 shows components of turbulent intensity at $x/c = 1$. The axial component dominates the wall boundary–layers whereas all the components are of same order for the wake. The boundary–layer of the bottom wall is far away from the tip vortex core.

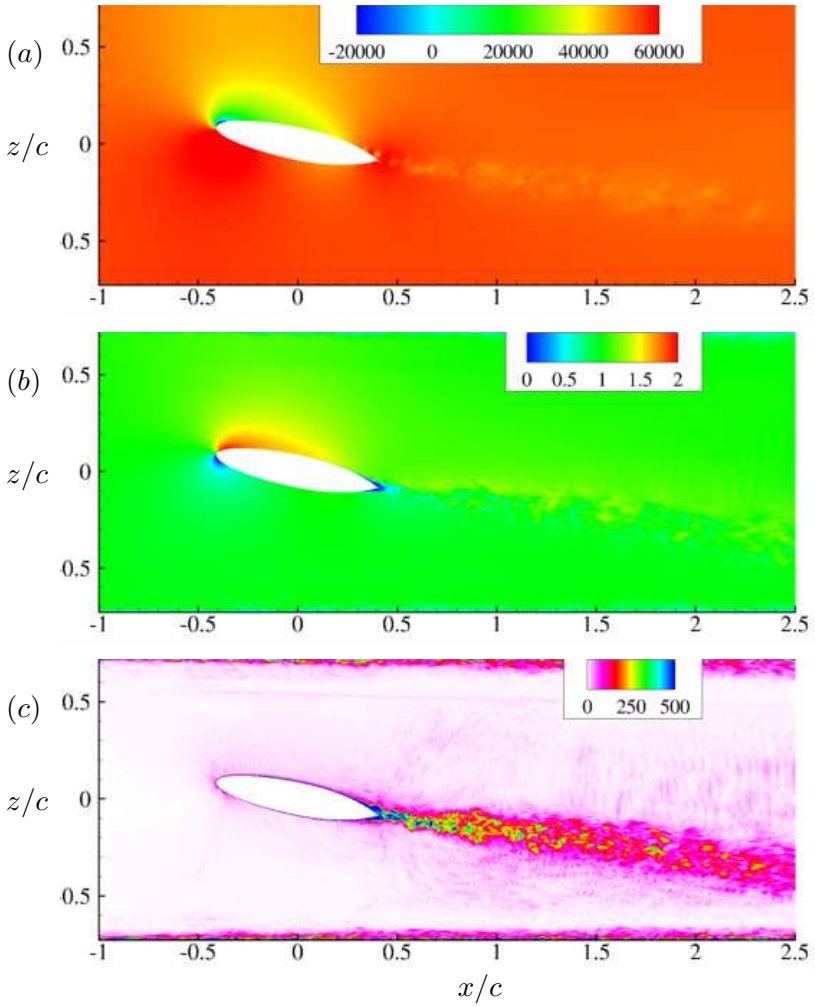

Figure 5.10: Instantaneous flow field showing pressure in Pa (a), streamwise velocity (b) and vorticity magnitude (c) in $y/c = -0.83$ plane.

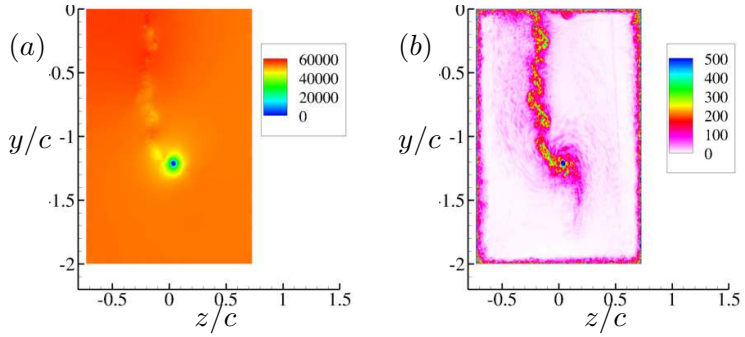

Figure 5.11: Instantaneous flow field showing pressure in Pa (a) and vorticity magnitude (b) at $x/c = 1$.

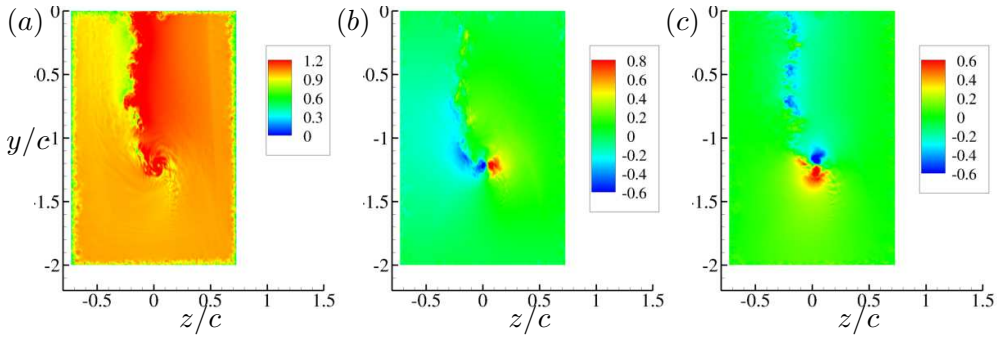

Figure 5.12: Instantaneous velocity components in streamwise (a), vertical (b) and horizontal (c) directions at $x/c = 1$.

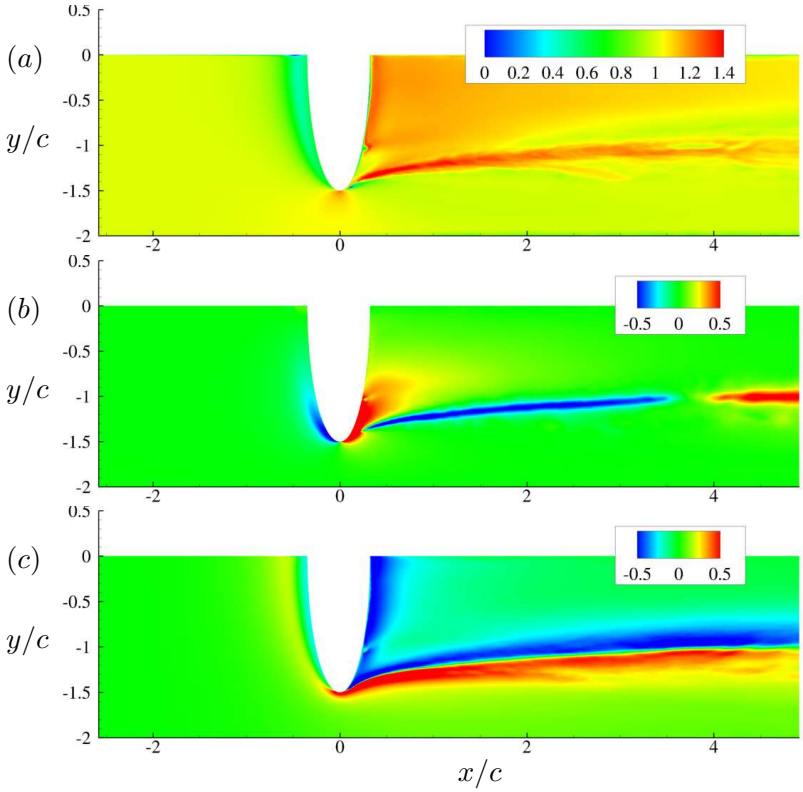

Figure 5.13: Mean velocity components in axial (a), vertical (b) and horizontal (c) directions are shown in $z = 0$ plane.

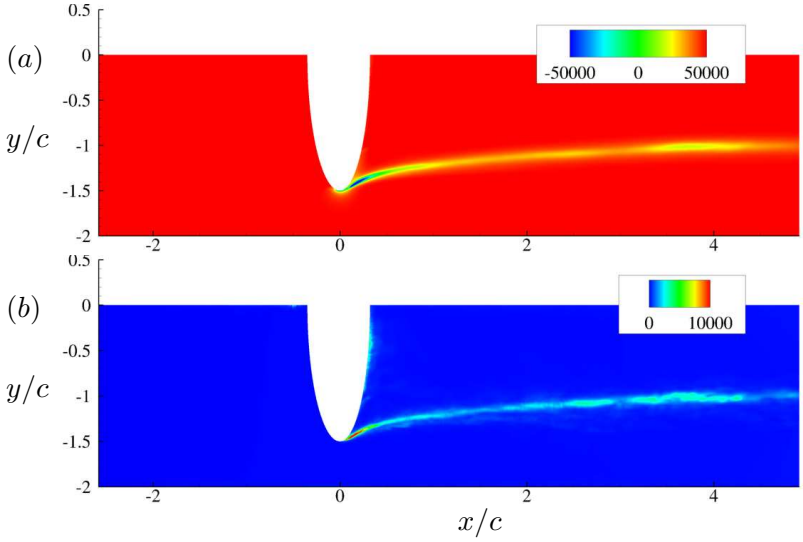

Figure 5.14: Mean (a) and rms (b) values of pressure in Pa.

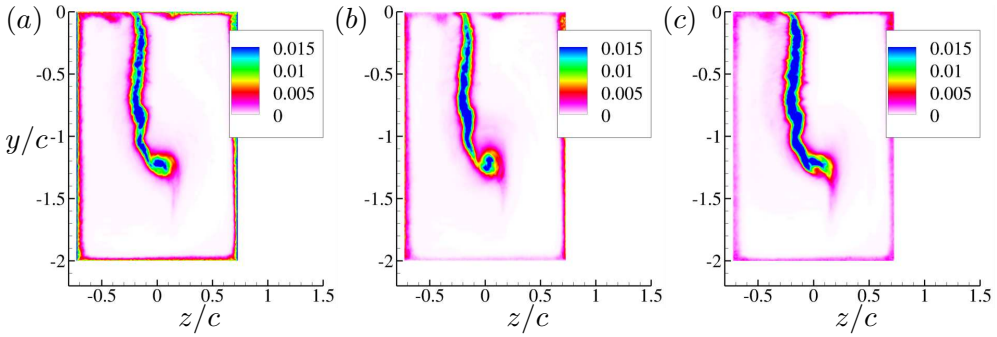

Figure 5.15: Turbulent intensities in streamwise (a), vertical (b) and horizontal (c) directions are shown at $x/c = 1$.

5.4.2 Cavitation characteristics

Prior to a presenting the results it is important to discuss the criteria used to identify inception. Inception is usually identified by visual or acoustic techniques. Visually, inception is detected when cavitating structures larger than a certain size are observed. However, there is no consensus about the threshold. Agarwal et al. [4] in a experimental study of inception at turbulent shear layers, identified inception when a bubble grows larger than $157\mu m$. In numerical simulations using the Euler–Lagrange framework, Bappy et al. [139] assumed that inception had occurred when a bubble became larger than $500\mu m$, while Park et al. [140] used the threshold of $1mm$. When the vapor phase is modeled in a eulerian framework, the volume fraction is commonly employed as the variable that identifies inception. Cheng et al. [85], e.g., visualized incipient structures by iso–surfaces of $\alpha = 0.1$. Here, we assume inception occurs when the volume fraction of the last bin, which contains bubbles larger than $1mm$, is greater than 0.001.

Effects of water quality

The results presented in this subsection are obtained at $Re = 9 \times 10^5$. A comparison between cases at both $Re = 9 \times 10^5$ and $Re = 1.4 \times 10^6$ is given later in this section. Figure 5.16 displays the iso–surfaces of $\alpha = 0.001$ for bubbles larger and smaller than $1mm$ for the natural and seeded cases at a instant of time. We can observe some features from both cases. First, we can see that the maximum total void fraction for both cases

is very small ($O(-3)$). Taking the mixture density as the volumetric average between the phases densities, $\rho = \alpha\rho_v + (1-\alpha)\rho_l$, this maximum void fraction would yield a total change in the mixture density of less than 0.1% if a homogeneous mixture approach was used, confirming that it is the incipient regime and that treating the vapor phase as a passive scalar is appropriate. The cavitation topology is very different between each case. In the natural case, inception is found to be an intermittent event confined to the tip vortex at a position close to the hydrofoil's tip. The region undergoing inception is so tiny that it is hard to visualize it in figure 5.16(a), therefore a zoomed view is provided in figure 5.17. In addition, the concentration of bubbles smaller than $1mm$ does not amount to $\alpha = 0.001$. In the seeded case, cavitation at the tip vortex is fully developed, showing a protuberant structure connected to the hydrofoil's tip. This behavior is consistent with the visual observations from Boulon et al. [70] at the critical cavitation number. These differences between each case are consistent with experimental observations [141] and highlight that the inception cavitation number for the seeded case is much higher than for the natural case. The seeded case also provide some unique features. Given the continuous supply of large nuclei in the freestream, part of the suction side very close to the leading edge of the hydrofoil also experience cavitation. Furthermore, the entire suction side is covered with a layer of bubbles smaller than $1mm$.

The probability density functions (PDF) of $\alpha \geq 0.001$ for bubbles larger than $1mm$ for both cases are given in figure 5.18(a) (indicating regions of cavitation), while the PDFs of a region experiencing a pressure lower than vapor pressure and experiencing the minimum pressure of the entire domain is displayed in figure 5.18(b). We can observe that the likelihood of cavitation is well aligned with the likelihood of a region experiencing values of pressure lower than the vapor pressure for the seeded case. For the natural case however, inception only happens in the regions most likely to experience extreme low values of pressure. In addition, for the natural case, inception is confined to a region around $x/c = 0.1$, which is within the range observed in the literature for strong water [141, 142]. The maximum value of the concentration per unit volume for bubbles larger than $1mm$ in each case is presented in figure 5.19(a) and (b). The corresponding power spectra densities (PSD) showing the dominant frequencies are given in figures

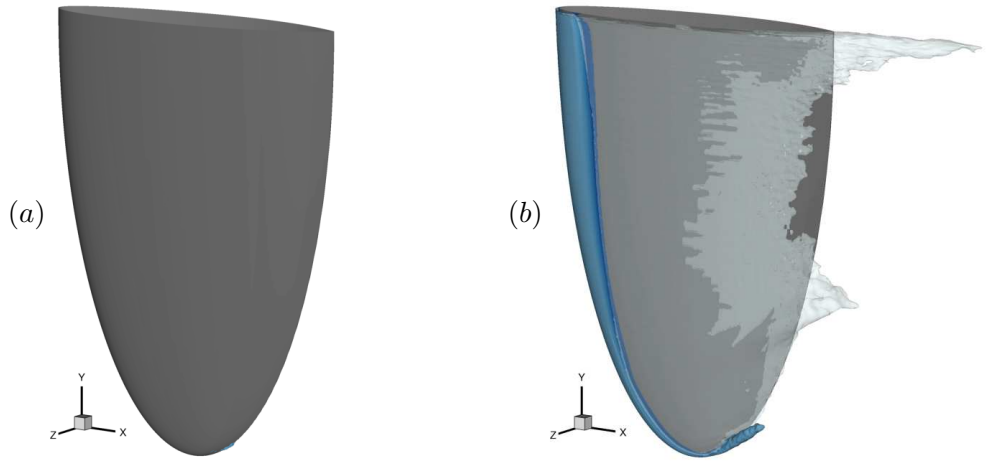

Figure 5.16: Iso–surfaces of $\alpha = 0.001$ for bubbles larger (blue) and smaller (transparent light gray) than $1mm$ for the natural (a) and seeded (b) cases.

5.19(c) and (d). It can be observed that the flow experiences a highly intermittent and chaotic explosive growth in number of bubbles for the natural case. This behavior is a direct consequence of the extreme and random pressure fluctuations of flows with high Re. When the flow is rich in nuclei, this behavior becomes less chaotic and a dominant frequency for the explosive increase in bubbles is visible. Here it is important to remind that our model is one–way coupled, meaning that the amount of vapor in each case is not affecting the pressure field. Thus, this result indicates that inception in a flow rich in nuclei is less affected by the pressure fluctuations than in a flow deplete in nuclei.

The vapor volume fraction for some bubble bins ($0.5\mu m$ - $1\mu m$, $5\mu m$ - $10\mu m$ and $1mm$ - $5mm$) are displayed in figure 5.21 and show their evolution across the wake. We can observe that the amount of void fraction for the small bubble groups ($0.5\mu m$ - $1\mu m$ and $5\mu m$ - $10\mu m$) very close to the hydrofoil is larger for the seeded case than it is for the natural one, despite these groups not being present at the inflow for the former. Furthermore, the evolution of these group along the wake differs considerably between each case. At close distances from the hydrofoil, these small bubbles are concentrated in the trailing vortex sheet for both cases. However for the natural case, this behavior persists beyond $x/c = 4$, while for the seeded case they are homogeneously distributed

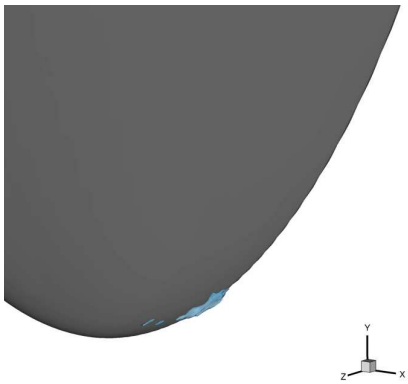

Figure 5.17: Zoomed view of an iso–surfaces of $\alpha = 0.001$ for bubbles larger than $1mm$ for the natural case.

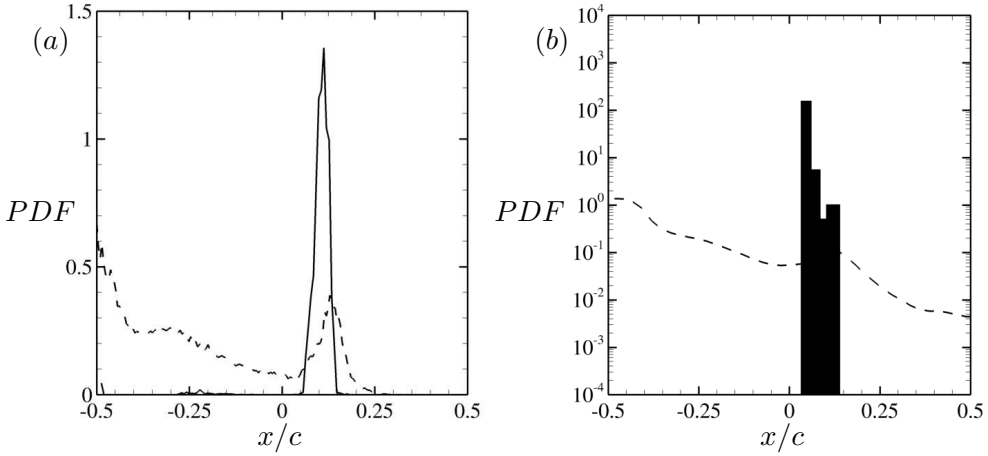

Figure 5.18: PDFs of $\alpha \geq 0.001$ for bubbles larger than $1mm$ are given in (a) for the natural (solid line) and seeded (dashed line). PDFs of $p < p_v$ (dashed line) and minimum pressure (bar) are given in (b)

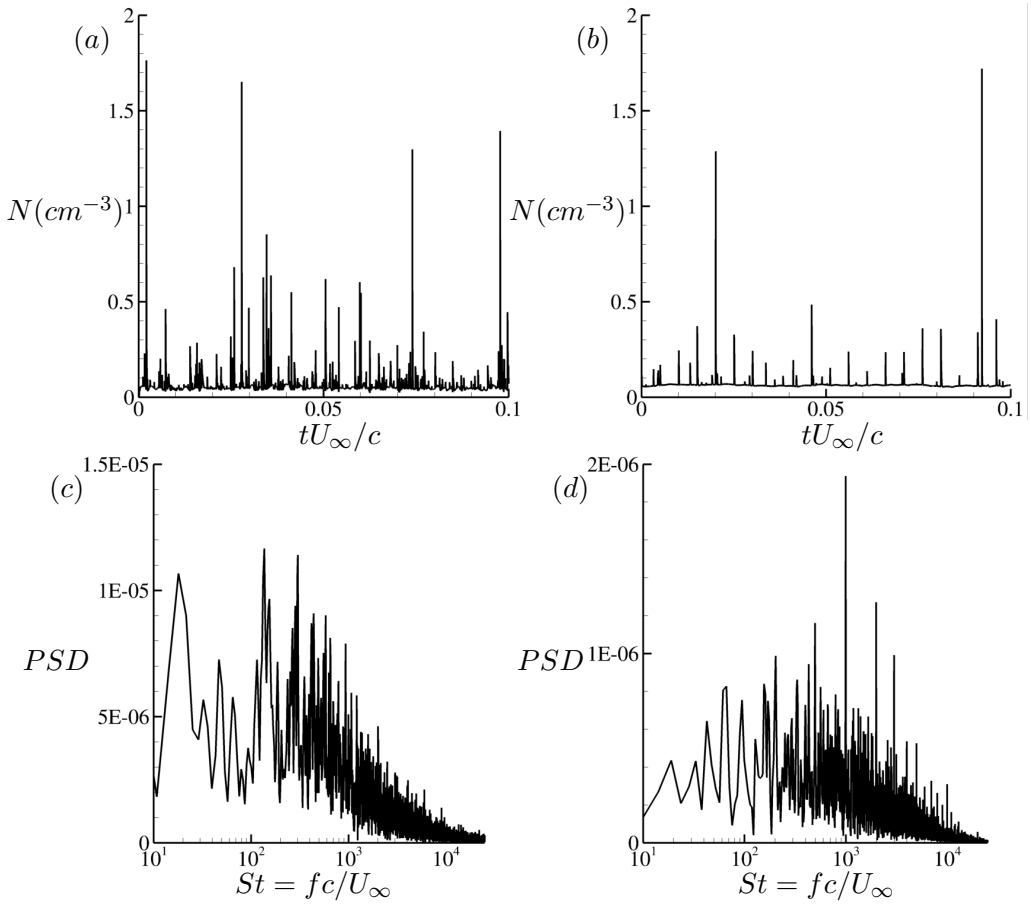

Figure 5.19: Time history of maximum concentration per unit volume for bubbles larger than $1mm$ for the natural (a) and seeded (b) cases at $Re = 9{\times}10^5$. Power spectra density of the signals are also given for the natural (c) and seeded (d) cases.

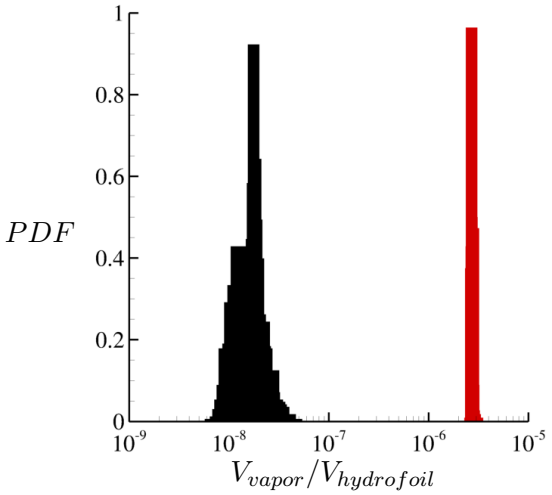

Figure 5.20: Volume of vapor produced in the natural (black) and seeded case (red) scaled with the volume of the hydrofoil.

across the section area already at $x/c = 3$. This occurs because the condensation process is proportional to the bubble number density (see equation (5.3)), which is proportional to the void fraction. Thus the larger values of volume fractions closes to the hydrofoil yields faster condensation rates as pressure is recovered downstream of the hydrofoil. Figures 5.22(a) and (b) show mean bubbles distributions at the hydrofoil tip ($x/c = 0$, $y/c = -1.5$) and at the center of the tip vortex ($x/c = 0.225$, $y/c = -1.4$) for both natural and seeded cases. At the foil tip, the concentration of bubbles for the seeded case are in general orders of magnitude larger than for the natural case, although they quickly become comparable at the tip vortex. In addition, a contrasting behavior can be observed after the flow travels from the foil tip to the tip vortex. The overall concentration of bubbles of different sizes increases when the flow is poor in nuclei, but drop when it is rich in nuclei, consistent with the predictions from figure 5.21.

Flow topology

We examine the incipient structures by studying their flow topology based on the invariants of the velocity gradient tensor, strain rate tensor and rotation rate tensor. These invariants are given in section 4.2.2. The invariants of the regions where and when

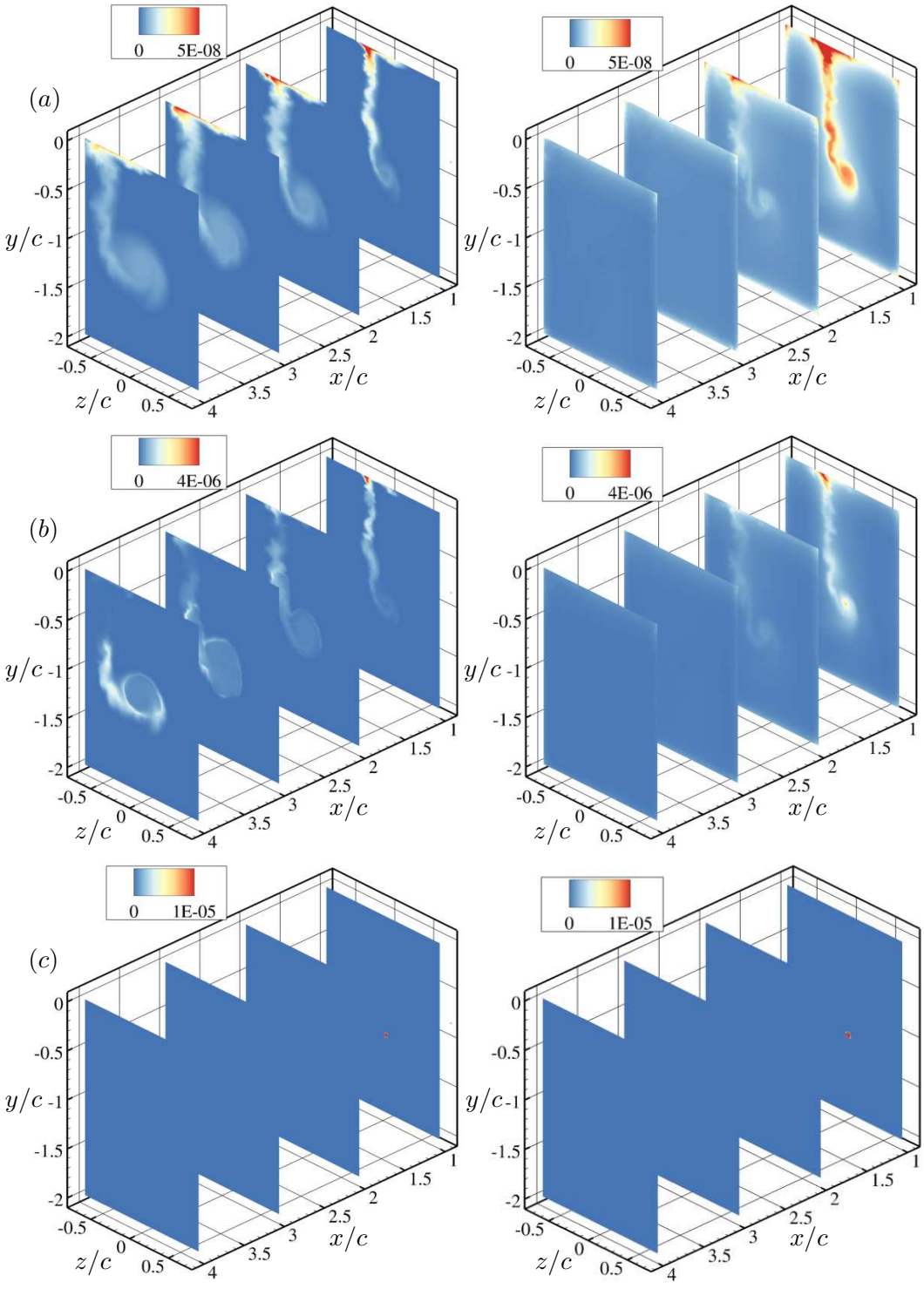

Figure 5.21: Vapor volume fraction of different bubble bins: $0.5\mu m$ - $1\mu m$ (a), $5\mu m$ - $10\mu m$ (b) and $1mm$ - $5mm$ (c) for the natural (left) and seeded (right) cases at $Re = 9 \times 10^5$.

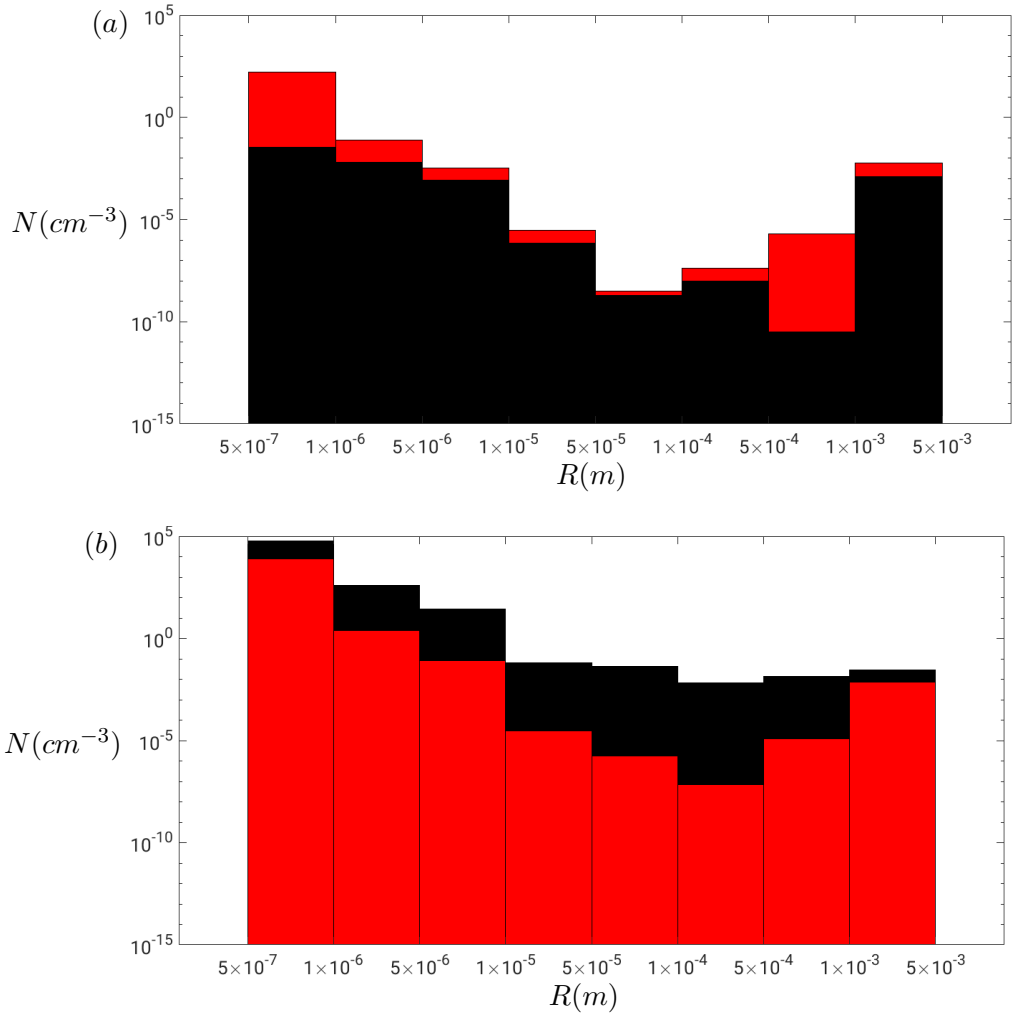

Figure 5.22: Mean bubble distribution at the hydrofoil tip (black) and at tip vortex (red) for the natural (a) and seeded (b) cases at $Re = 9 \times 10^5$.

$\alpha \geq 0.001$ for bubbles larger than $1mm$ are computed, and their joint–PDF are given in figure 5.23 showing the topology of the incipient structures for the natural case.

The joint–PDF of Q–R in figure 5.23(a) shows that inception more likely occurs in the stretched focal regions. The joint–PDF of Q_s–Q_w in figure 5.23(b) reveals that regions dominated by irrotational strain are favorable places of inception. In other words, the periphery of stretched vortices have higher likelihood of inception. The joint–PDF between pressure and κ is displayed in figure 5.24 and reveals a predominance of $\kappa \approx 0.75$, which means that inception is most likely to occur when the vortex has a stretching rate around $1.8\times$ larger than its rotation rate. This result is in contrast with the one obtained for inception in a shear layer given in section 4.2.2, where inception was found to occur primarily in regions dominated by rotation. It can also be observed that, although inception occurs primarily when the stretching rate dominates, a wide range of κ can lead to inception at vapor pressure, including values that indicate that the flow is dominated by rotation. However, this range narrows down as pressure drops. The lowest values of pressure leading to inception occurs exclusively when that flow region is dominated by stretching. Another quantity of interest is defined by Ooi et al. [125] as

$$\Sigma = \frac{R_s - R}{Q_w}, \tag{5.8}$$

that represents the rate at which the vorticity is stretched ($\Sigma > 0$) or contracted ($\Sigma < 0$). Figure 5.25 shows the joint–PDF between κ and Σ of the incipient structures. The plot reveals a preference for positive straining rate (indicating vorticity stretching), consistent with figure 5.23(a). Interestingly, the plot also reveals that the larger vorticity stretching rates of the inception structures are associated with $\kappa \approx 1$. Figure 5.26 displays isocontours of λ_2, showing the tip vortex surrounded by smaller secondary vortices, colored by α, κ and Σ. We can see that vapor is found in the initial part of the tip vortex, surrounded by the smaller secondary vortices, and that this is a region dominated by the irrotational straining with high stretching rates. As the tip vortex moves further downstream and ceases to be surrounded by the seconday vortices, it

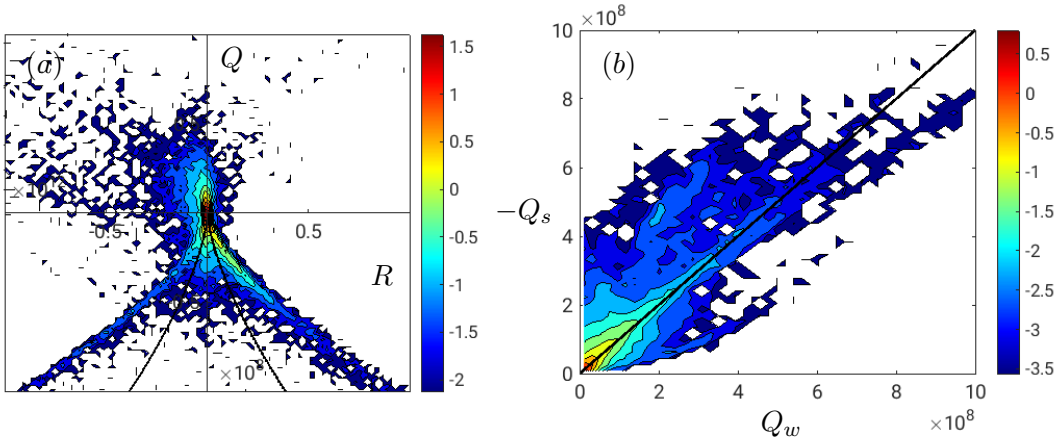

Figure 5.23: Joint–PDFs of Q–R (a) and Q_s–Q_w (b) of the incipient regions for the natural case. Levels in both plots are in logarithmic scale and the invariants are in non–dimensional units (using the appropriate combination of the root chord length, c, and the freestream velocity, U_∞).

starts to become dominated by rotation ($\kappa > 1$) and presents larger contraction rates ($\Sigma < 0$).

Effects of Reynolds number

Inception was also investigated at a higher Reynolds number ($Re = 1.4 \times 10^6$ with $U_\infty = 12\ m/s$) at the same cavitation number ($\sigma = 2.1$). The time history of the maximum concentration per unit volume of bubbles larger than $1mm$ and the PSD of its respective signal are given in figure 5.27 for the natural and seeded cases. Differently from the conditions at $Re = 9 \times 10^5$, both cases experience a chaotic pattern of growth in number of large bubbles without any clear dominant frequency. The probability density function of $\alpha \geq 0.001$ for bubbles larger than $1mm$ at the two values of Re is displayed in figure 5.28 for the natural case. Although the two values of Re are relatively close to each other, it can be seen that the inception location moves slightly downstream with increasing Re. Figure 5.29 (a) and (b) shows the PDF of total volume of vapor produced (for bubbles larger than $1mm$) for the natural and seeded cases, respectively. It can be seen that increasing Re but keeping σ the same, in this case,

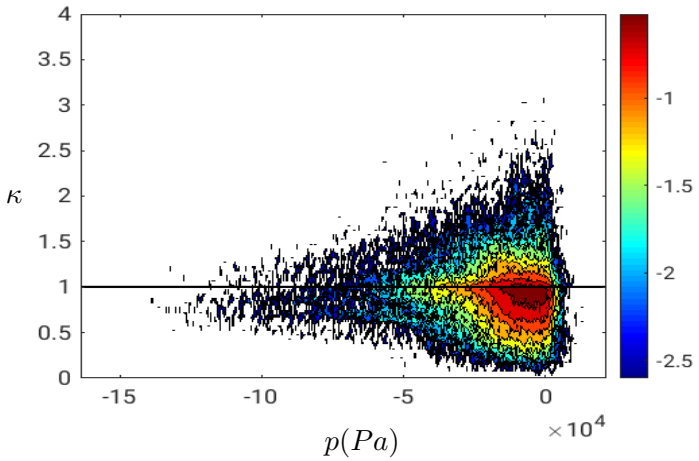

Figure 5.24: Joint–PDF between pressure and κ. The line of $\kappa = 1$ signals the boundary between stretching to rotation dominated.

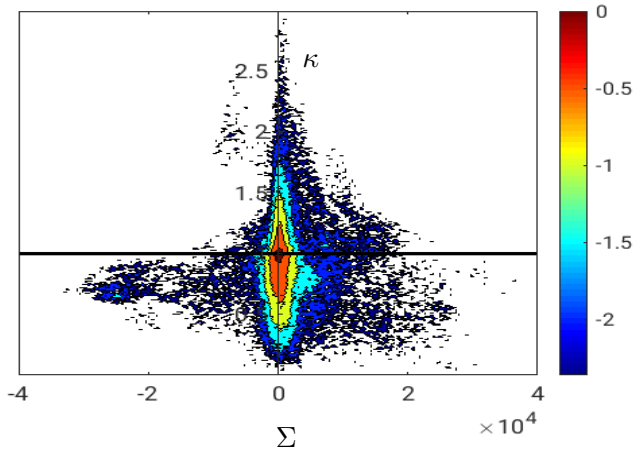

Figure 5.25: Joint–PDF between Σ and κ. Levels are in logarithmic scale and the black line indicates $\kappa = 1$

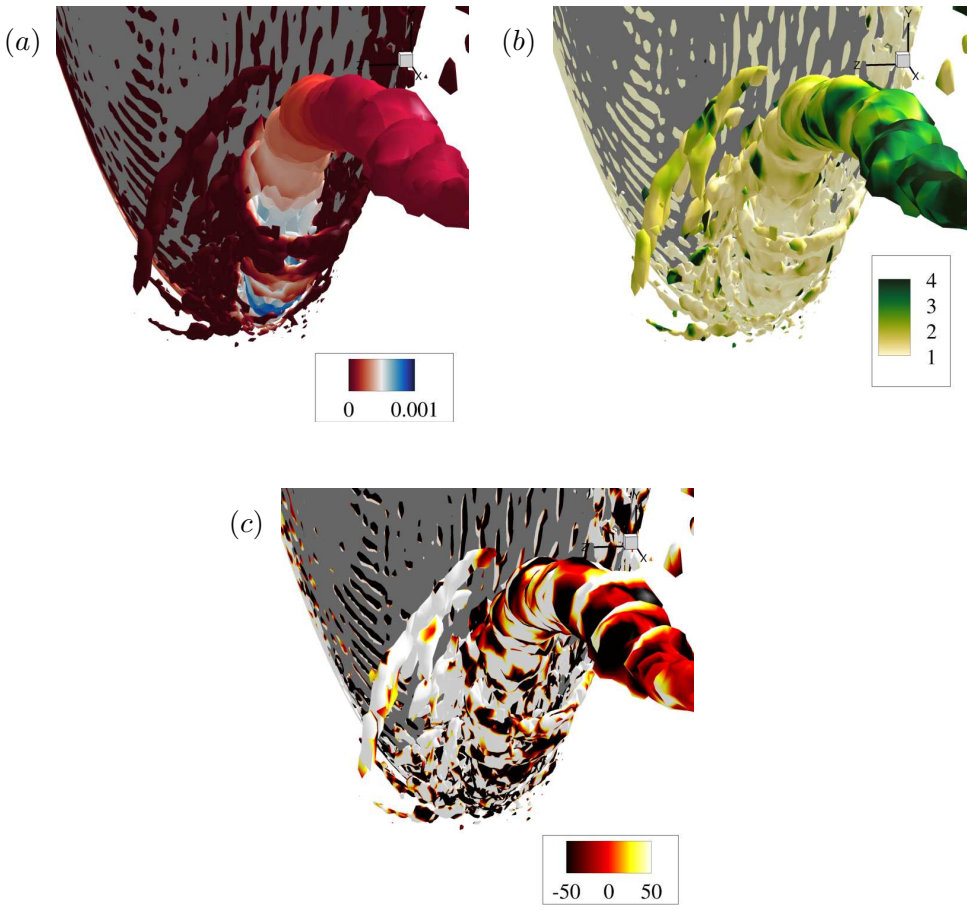

Figure 5.26: Frontal view of the tip vortex and secondary vortices colored with the vapor volume fraction (a), κ (b) and Σ (c).

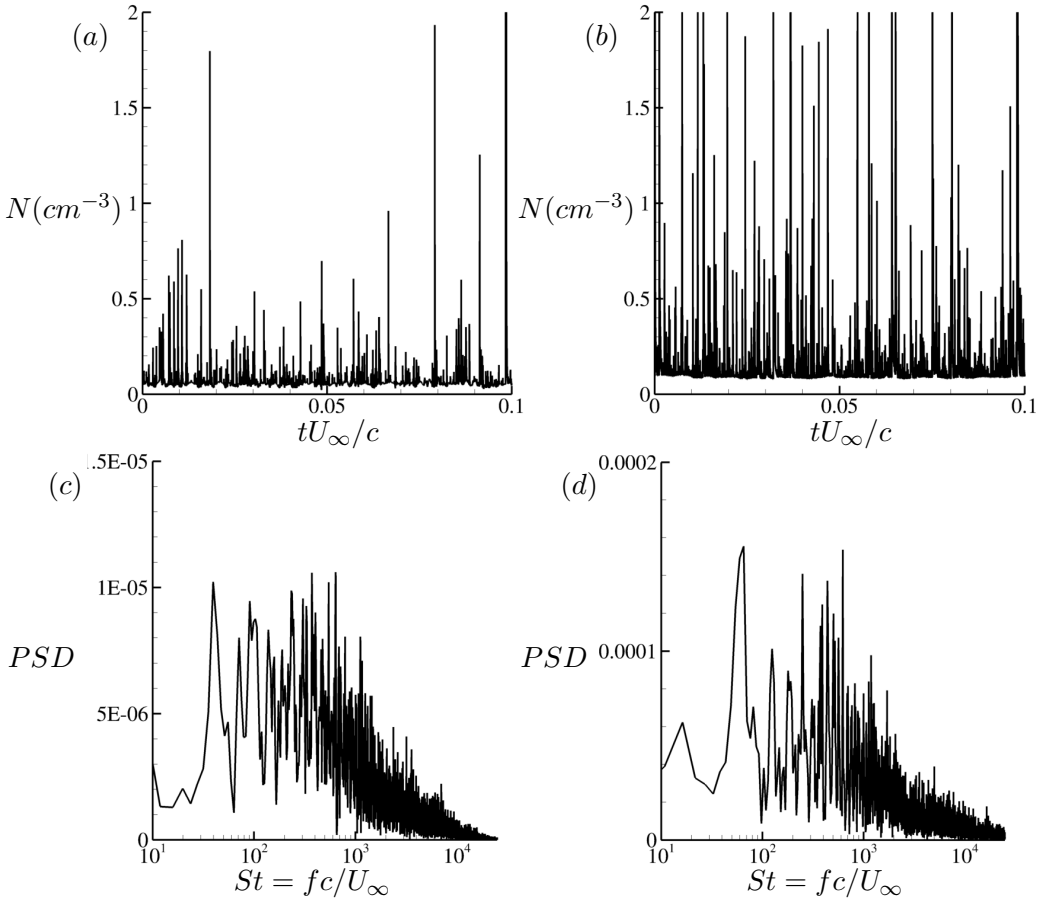

Figure 5.27: Time history of maximum concentration per unit volume for bubbles larger than $1mm$ for the natural (a) and seeded (b) cases at $Re = 1.4 \times 10^6$. Power spectra density of the signals are also given for the natural (c) and seeded (d) cases.

does not significantly change the volumes of vapor produced, although there is a modest increase for the seeded case. It becomes evident when comparing figure 5.20 with figure 5.29, that water quality has a much larger effect on the amounts of vapor produced than the Re, for the incipient regime.

The effect of Re on inception is explained here by tracking particles injected from the hydrofoil's tip and investigating their pressure history at both Re. These particles

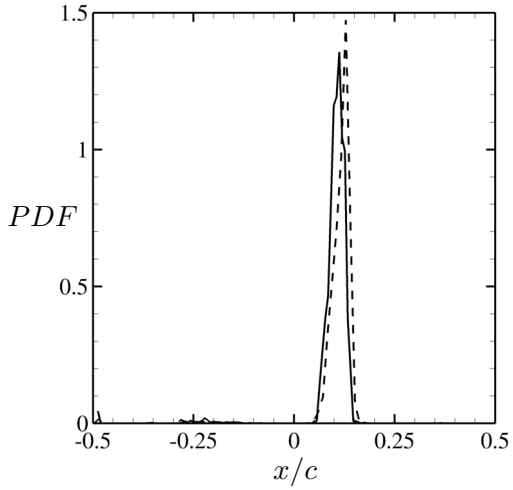

Figure 5.28: PDFs of $\alpha \geq 0.001$ for bubbles larger than $1mm$ for $Re = 9 \times 10^5$ (solid) and $Re = 1.4 \times 10^6$ (dashed).

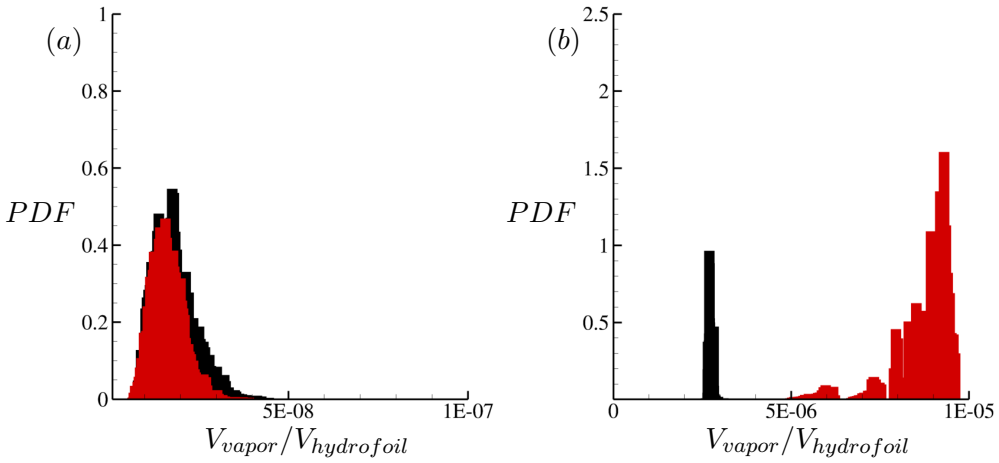

Figure 5.29: Volume of vapor produced in the natural (a) and seeded (b) cases at $Re = 9 \times 10^5$ (black) and $Re = 1.4 \times 10^6$ (red) scaled with the volume of the hydrofoil.

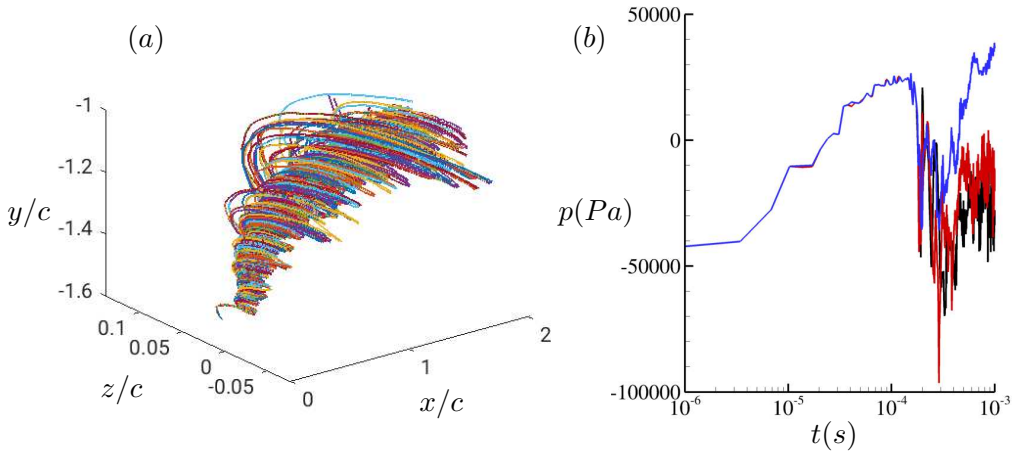

Figure 5.30: Particles trajectories are given in (a), where each line corresponds to the path of one of the 1000 particles. Pressure history of only three particles are given in (b) for better visualization. Both plots are obtained for $Re = 9 \times 10^5$.

are assumed to follow the liquid velocity, hence their positions are obtained as

$$\frac{d\vec{x}}{dt} = \vec{u}. \tag{5.9}$$

We inject 1000 particles from the hydrofoils's tip for both Re studied in subsection 5.4.2. Figure 5.30 shows example of the particles trajectories and the pressure history that some of them experience. From figure 5.30(a), we can see that the particles move in a spiral course following the tip vortex direction.

The PDFs for the lagrangian pressure histories of the particles at both Re are presented in figure 5.31. As expected, higher Re yields a broader spectrum of pressure values. It is important to remind that both Re cases were simulated at the same inflow cavitation number of 2.1, which means that the inflow pressure at $Re = 1.4 \times 10^6$ is much larger than at $Re = 9 \times 10^5$. Despite that, the plot shows that even if increasing Re is accompanied by an increase in ambient pressure, the particles still have a higher likelihood of experiencing extreme low values of pressure. It also shows that the particles have a much larger likelihood of experiencing higher values of pressure with increasing Re. Figure 5.32 shows the cumulative distribution functions of the total time that the particles experience pressure lower than vapor pressure. It can be seen that the

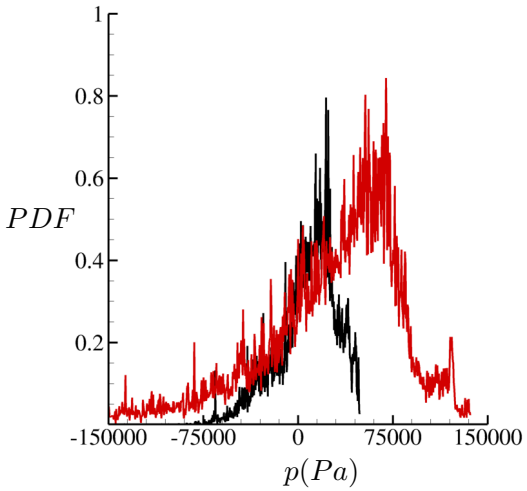

Figure 5.31: PDFs of lagrangian pressure history for the 1000 particles injected at $Re = 9 \times 10^5$ (black) and $Re = 1.4 \times 10^6$ (red).

probability of particles spending shorter periods of time at a pressure lower than vapor pressure increases with increasing Re. This reinforces and help to explain the trend observed in figure 5.29 where Re did not have an impact on the amounts of vapor produced. The reason behind this is that inception requires that the low pressure acting on small vapor structures to be sustained for some time. Therefore, the volume of vapor produced at inception with an increase in Re at the same σ is mostly unchanged.

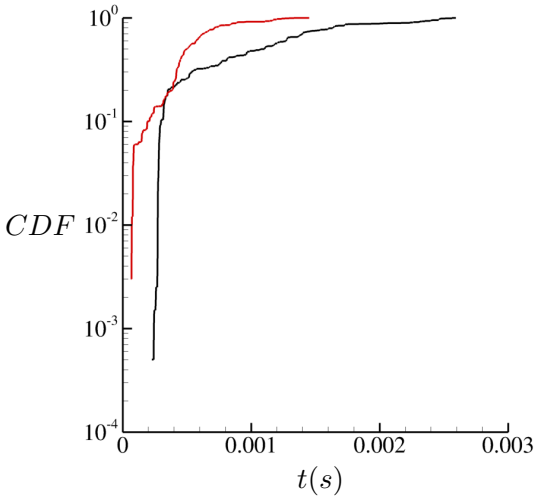

Figure 5.32: CDFs of the total time bubbles experience pressure lower than vapor pressure at $Re = 9 \times 10^5$ (black) and $Re = 1.4 \times 10^6$ (red).

Chapter 6

Summary

The development of a numerical method to study cavitating flows in the developed regime based on the homogeneous mixture approach was presented. The method treats the mixture of water–vapor–gas as a single compressible medium, and is an extension of the method presented in the work of Gnanaskandan and Mahesh [1]. The algorithm uses a predictor–corrector approach. A symmetric non–dissipative scheme is employed in the predictor step while corrector step uses a characteristic–based filtering method to obtain the final solution. A sensor based on vorticity, divergence and vapor/gas volume fraction is used in the corrector step to prevent excessive dissipation away from the discontinuities. The algorithm is first validated for canonical one dimensional problems and the accuracy of the shock capturing scheme is demonstrated.

Cavitating flow over a circular cylinder is studied for a range of σ showing both cyclic and transitional cavitation regimes at different Reynolds number and with different amounts of free–stream vapor and gas volume fraction. NCG is introduced in the free–stream as a free gas (prescribed in a similar way as vapor nuclei) and its effect on the flow field is discussed. In the cyclic regime, cavitation was observed in periodically shedding Kármán vortices; while in the transitional regime, the cavity shedding was observed due to propagating condensation shocks.

St based on cavity length when plotted with σ shows a peak just before the onset of condensation shock wave induced cavity shedding. Cavity shedding frequency obtained

from the drag history showed similar behavior in the presence of NCG. At $\sigma = 0.85$ (near transition), however, FFT of pressure history did not show a secondary peak due to low frequency detachment in the presence of NCG, suggesting its influence on delaying the transition to low frequency shedding behavior. DMD used to investigate wake characteristics revealed that cavitation delays the first transition of the Kármán vortex street. Reduction in shedding frequency as σ is lowered from non–cavitating to cavitating conditions is used to explain this behavior.

It was observed that vapor and gas uniformly introduced in the free–stream, distribute themselves differently in the wake of cylinder depending upon local flow conditions, particularly at lower cavitation numbers as the pressure in the wake dropped below vapor pressure. This was explained using σ_{local}, to distinguish vapor production due to phase change as compared to expansion of vapor or gas. Vapor and NCG distribution in the boundary–layer suggested that cavitation as a mass transfer process only occurs inside a fine layer in the near wall region, while the remaining of the boundary–layer only undergoes expansion of both vapor and gas. Free–stream void fraction was shown to have a large impact on the mean gas volume fraction observed inside the cavity. However, mean vapor volume fraction seems relatively independent. The boundary–layer separation point for both laminar and turbulent flow was observed to move downstream as the free–stream volume fraction is increased.

Rankine–Hugoniot jump conditions were derived for the complete system. The shock speed obtained using the jump conditions is used to compute the Mach number of propagating condensation front to show that it is indeed supersonic for both Re studied. It is however noted that the condensation shock propagates into a subsonic region of the cavity, based on local Mach numbers. In the presence of NCG, it was shown that the strength of the condensation shock reduces as it approaches the cylinder surface. This results in multiple condensation shocks being necessary for detachment of cavity. Weakening of shock strength in the presence of gas was due to reduction in pressure ratio across the condensation shock as it approaches the cylinder surface. As the shock moves upstream towards the cylinder, it condenses the vapor along the way. However, the fact that it can not condense the NCG resulted in a lower pressure behind the shock,

which was shown using the jump condition. The conditions necessary for the occurrence of a supersonic condensation front is, then, assessed using its pressure ratio.

At $Re = 3900$, it was observed that the location of maximum vapor production in the cyclic regime is shifted from the cylinder surface to the immediate wake, with no major changes to the levels of volume fraction inside the cavity. The mean NCG volume fraction, however, reduces by an order of magnitude inside the cavity when compared to the mean values at $Re = 200$. The growth of a nearly two–dimensional cavity in the transitional regime, significantly reduces vortex stretching and baroclinic torque from the values observed in the cyclic regime. Finally, it is observed that at $Re = 3900$ for the transitional regime, the cavity detaches after the passage of a more vertically oriented condensation shock, different from the horizontally oriented shock at $Re = 200$.

A method was developed to simulate and predict cavitation inception. The method consists of treating vapor as a passive scalar in an incompressible liquid. An advection–diffusion equation with a source term is solved for the concentration of vapor in a dual time step procedure, allowing for higher time steps. Convective and diffusive fluxes are obtained with an approach based on a least–square method that provides accurate results on skewed meshes. The source term is split into terms that are treated explicitly and implicitly, yielding a stable solution as shown in the subsection 2.2.2. The model was validated against results obtained using the compressible homogeneous mixture approach where acoustic stiffness was handled by the preconditioning methodology developed by Bhatt and Mahesh [20].

Inception in the shear layer of a backstep is investigated in the experimental configuration of Agarwal et al. [4] with inflow turbulent boundary–layers at $Re_\tau = 800$ and 1500. The case of $Re_\tau = 800$ does not show cavitation for the range of σ studied in the experiments. Therefore, we simulate this case at a lower ambient pressure as a verification test. For $Re_\tau = 1500$, we study the experimental conditions of $\sigma = 0.55$ and $\sigma = 0.45$. Pressure and void fraction statistics are computed and the likelihood of cavitation exhibits good agreement with experimental data. The inception event rates show an increase by around $O(1)$ when the cavitation number is reduced from $\sigma = 0.55$ to $\sigma = 0.45$ and are more likely to occur around $0.4 < x/L_r < 0.8$. The flow topology is

investigated and the cores of the stretched quasi–streamwise vortices (QSV) are found to be the preferred sites for inception. Additionally, the ratio between rotation and strain rates and its relation with inception was investigated. It was observed that inception most likely occurs when the rotation rate of the vortex tube is $4\times$ stronger than the stretching rate. The pressure inside the QSVs are found to be $-1500Pa$ and $-5500Pa$ for $\sigma = 0.55$ and $\sigma = 0.45$, respectively. Lastly, an analysis reveals a predominance for the ratio between the principal strain rates of $2:1:-3$ and $3:1:-4$ for the cavitating QSVs.

LES is performed to investigate cavitation inception over an elliptical hydrofoil at two different values of Re and at $\sigma = 2.1$. The numerical model presented in section 2.2 is extended to include multiple groups of bubbles of different sizes. This modification allows for the investigation of the effects of water quality on inception. We study two different conditions: one when the flow is poor in nuclei (called "natural" distribution) and the other when the flow is rich in nuclei (called "seeded" distribution). It was found that inception characteristics change drastically depending on the water quality. The volume of vapor produced for the seeded case is orders of magnitude larger than for the natural case, with vapor being formed along the tip vortex and on the leading edge of the foil. This is in contrast with the natural case where vapor formation is an intermittent event confined to a small region close to the foil's tip. The results showed that the explosive growth in number of bubbles at $Re = 9\times10^5$ is chaotic for the natural case, with no dominant frequency. For the seeded case, however, this behavior becomes less chaotic and a dominant frequency appears. With an increase in Re, both flow conditions experience this behavior. It was found that water quality has a bigger impact on inception than the Re, and that inception characteristics are mostly unaffected by the change in Re when the flow is very deplete of nuclei. The inception location remains unchanged with increasing Re when the flow is poor in nuclei. In addition, the increase in the volume of vapor produced with increasing Re was found to be less than $O(1)$ for the seeded case and negligible for the natural case. To help explain that, particles were released from the foil's tip and their lagrangian pressure history were tracked. The results indicated that, although vapor structures would have higher likelihood of

experiencing very low values of pressure with increasing Re, the amount of time they are under these low values of pressure is reduced. The flow topology of the incipient structures were investigated for the natural case, and it was found that inception have a higher likelihood to occur in focal regions dominated by irrotational straining with high stretching rates.

Bibliography

[1] A. Gnanaskandan and K. Mahesh. A numerical method to simulate turbulent cavitating flows. *International Journal of Multiphase Flow*, 70:22–34, 2015.

[2] T. J. O'Hern. An experimental investigation of turbulent shear flow cavitation. *Journal of Fluid Mechanics*, 215:365–391, 1990.

[3] N. A. Chang, J. Choi, R. Yakushuji, and S. L. Ceccio. Cavitation inception during the interaction of a pair of counterrotating vortices. *Physics of Fluids*, 24:1–15, 2012.

[4] K. Agarwal, O. Ram, and J. Katz. Cavitating structures at inception in turbulent shear flow. In *Proceedings of the 10th International Symposium on Cavitation (CAV2018)*, 2018.

[5] M. Callenaere, J-P. Franc, J. Michel, and M. Riondet. The cavitation instability induced by the development of a re-entrant jet. *Journal of Fluid Mechanics*, 444: 223–256, 2001.

[6] H. Ganesh, S. A. Makiharju, and S. L. Ceccio. Bubbly shock propagation as a mechanism for sheet–to–cloud transition of partial cavities. *Journal of Fluid Mechanics*, 802:37–78, 2016.

[7] M. Bhatt and K. Mahesh. Numerical investigation of partial cavitation regimes over a wedge using large eddy simulation. *International Journal of Multiphase Flow*, 122:103155, 2020.

[8] URL http://www.1.k.u-tokyo.ac.jp/yama/fluidlab/Research/CavPictures/index_e.html.

[9] URL http://cav.safl.umn.edu/research-areas/ventilated-supercavitation.

[10] C. E. Brennen. Cavitation in medicine. *Interface focus*, 5(5):20150022, 2015.

[11] R. E. A. Arndt. Cavitation in fluid machinery and hydraulic structures. *Annual Review of Fluid Mechanics*, 13(1):273–326, 1981.

[12] R. E. A. Arndt. Cavitation in vortical flows. *Annual Review of Fluid Mechanics*, 34(1):143–175, 2002.

[13] K. J. Farrel. Eulerian/Lagrangian analysis for the prediction of cavitation inception. *Journal of Fluids Engineering*, 125:46–52, 2003.

[14] C-.T. Hsiao, G. L. Chahine, and H. L. Liu. Scaling effect on prediction of cavitation inception in a line vortex flow. *Journal of Fluids Engineering*, 125(1):53–60, 2003.

[15] C-.T. Hsiao and G. L. Chahine. Scaling of tip vortex cavitation inception noise with a bubble dynamics model accounting for nuclei size distribution. *Journal of Fluids Engineering*, 127(1):55–65, 2005.

[16] E. Shams, J. Finn, and S. V. Apte. A numerical scheme for Euler–Lagrange simulation of bubbly flows in complex systems. *International Journal for Numerical Methods in Fluids*, 67(12):1865–1898, 2011.

[17] C. P. Egerer, S. J. Schmidt, S. Hickel, and N. A. Adams. Efficient implicit LES method for the simulation of turbulent cavitating flows. *Journal of Computational Physics*, 316:453–469, 2016.

[18] B. Budich, S. J. Schmidt, and N. A. Adams. Numerical simulation and analysis of condensation shocks in cavitating flow. *Journal of Fluid Mechanics*, 838:759–813, 2018.

[19] F. L. Brandao, M. Bhatt, and K. Mahesh. Numerical study of cavitation regimes in flow over a circular cylinder. *Journal of Fluid Mechanics*, 885:A19, 2020.

[20] M. Bhatt and K. Mahesh. A numerical approach to address the acoustic stiffness in cavitating flows. *International Journal of Multiphase Flow*, 141:103568, 2021.

[21] A. K. Singhal, M. M. Athavale, H. Li, and Y. Jiang. Mathematical basis and validation of the full cavitation model. *Journal of Fluids Engineering*, 124(3): 617–624, 2002.

[22] J. H. Seo and S. Lele. Numerical investigation of cloud cavitation and cavitation noise on a hydrofoil section. In *Proceedings of the 7th International Symposium on Cavitation*, number 0062, pages 1–15, 2009.

[23] E. Goncalves and R-F. Patella. Numerical simulation of cavitating flows with homogeneous models. *Computers & Fluids*, 38(9):1682–1696, 2009.

[24] O. Coutier-Delgosha, R. Fortes-Patella, and J-L. Reboud. Evaluation of the turbulence model influence on the numerical simulations of unsteady cavitation. *Journal of Fluids Engineering*, 125(1):38–45, 2003.

[25] R. E. Bensow and G. Bark. Implicit LES predictions of the cavitating flow on a propeller. *Journal of Fluids Engineering*, 132(4):1–10, 2010.

[26] Y. Wang, X. Wu, C. Huang, and X. Wu. Unsteady characteristics of cloud cavitating flow near the free surface around an axisymmetric projectile. *International Journal of Multiphase Flow*, 85:48–56, 2016.

[27] Y. Long, X. Long, B. Ji, and T. Xing. Verification and validation of large eddy simulation of attached cavitating flow around a clark–y hydrofoil. *International Journal of Multiphase Flow*, 2019.

[28] S. A. Fry. Investigating cavity/wake dynamics for a circular cylinder by measuring noise spectra. *Journal of Fluid Mechanics*, 142:187–200, 1984.

[29] J.P Franc and J.M Michel. *Fundamentals of Cavitation*. Kluwer Academic Publishers, 2005.

[30] J. K. Jakobsen. On the mechanism of head breakdown in cavitating inducers. *Journal of Basic Engineering*, pages 291–305, 1964.

[31] X. Wu, E. Maheux, and G.L. Chahine. An experimental study on sheet to cloud cavitation. *Experimental Thermal and Fluid Science*, 83:129–140, 2017.

[32] S. Schenke and T.J.C. van Terwisga. Simulating compressibility in cavitating flow using incompressible mass transfer solver. In *Proceedings of the 5th International Symposium of Marine Propulsors*, 2017.

[33] S. Jahangir, W. Hogendoorn, and C. Poelma. Dyanmics of partial cavitation in an axisymmetric converging-diverging nozzle. *International Journal of Multiphase Flow*, 106:34–45, 2018.

[34] K. R. Laberteaux and S. L. Ceccio. Partial cavity flows. Part 1. Cavities forming on models without spanwise variation. *Journal of Fluid Mechanics*, 431:1–41, 2001.

[35] L. Briancon-Marjollet, J. P. Franc, and J. M. Michel. Transient bubbles interacting with an attached cavity and the boundary layer. *Journal of Fluid Mechanics*, 218: 355–376, 1990.

[36] D. T. Kawakami, Q. Gin, and R. Arndt. Water quality and the periodicity of sheet/cloud cavitation. In *Proceedings of FEDSM'05*, 2005.

[37] F. Orley, T. Trummler, S. Hickel, M. S. Mihatsch, S. J. Schmidt, and N. A. Adams. Large–eddy simulation of cavitating nozzle flow and primary jet break-up. *Physics of Fluids*, 27:086101, 2015.

[38] S. A. Makiharju, H. Ganesh, and S. L. Ceccio. The dynamics of partial cavity formation, shedding and the influence of dissolved and injected non–condensable gas. *Journal of Fluid Mechanics*, 829:420–458, 2017.

[39] J. Vennig, S. Smith, P. Brandner, D. Giosio, and B. Pearce. The influence of nuclei content on cloud cavitation about a hydrofoil. In *Proceedings of the International Symposium on Transport Phenomena and Dynamics of Rotating Machinery*, 2017.

[40] T. Trummler, L. Freytag, S. J. Schmidt, and N. A. Adams. Large eddy simulation of a collapsing vapor bubble containing non–condensable gas. In *Proceedings of the 10th International symposium on cavitation*, 2018.

[41] Y. Saito, R. Takami, I. Nakamori, and T. Ikohagi. Numerical analysis of unsteady behavior of cloud cavitation around a NACA0015 foil. *Computational Mechanics*, 40:85–96, 2007.

[42] J. H. Seo, Y. J. Moon, and B. R. Shin. Prediction of cavitation flow noise by direct numerical simulation. *Journal of Computational Physics*, 227:6511–6531, 2008.

[43] A. Gnanaskandan and K. Mahesh. Large eddy simulation of the transition from sheet to cloud cavitation over a wedge. *International Journal of Multiphase Flow*, 83:86–102, 2016.

[44] A. Gnanaskandan and K. Mahesh. Numerical investigation of near–wake characteristics of cavitating flow over a circular cylinder. *Journal of Fluid Mechanics*, 790:453–491, 2016.

[45] B. C. S. Rao and D. V. Chandrasekhara. Some characteristics of cavity flow past cylindrical inducers in venturi. *Journal of Fluids Engineering*, 98(3):461–466, 1976.

[46] A. S. Ramamurthy and P. Bhaskaran. Constrained flow past cavitating bluff bodies. *Journal of Fluids Engineering*, 99(4):717–726, 1977.

[47] P. Kumar, S. Bakshi, and D.Chatterjee. Experimental investigation of cavitation behind a circular cylinder in cross–flow. *Journal of Thermal Science and Engineering Applications*, 9:0310004–1–0310004–6, 2017.

[48] P. Kumar, D. Chatterjee, and S. Bakshi. Experimental investigation of cavitating structures in the near wake of a cylinder. *International Journal of Multiphase Flow*, 89:207–217, 2017.

[49] J. Katz and T. J. O'Hern. Cavitation in large scale shear flows. *Journal of Fluids Engineering*, 108:373–376, 1986.

[50] C.O. Iyer and S.L. Ceccio. The influence of developed cavitation on the flow of a turbulent shear layer. *Physics of Fluids*, 14(10):3414–3431, 2002.

[51] V. Aeschlimann and S. Barre. PIV-LIF determination of mean velocity field and reynolds stress tensor in a cavitating mixing layer. In *Proceedings of the 7th International Symposium on Cavitation (CAV2009)*, 2009.

[52] K. Agarwal, O. Ram, J. Wang, Y. Lu, and J. Katz. Measuring the 3D pressure field and relating it to cavitation inception in a turbulent shear layer. In *Proceedings of the 33rd Symposium on Naval Hydrodynamics*, Osaka, Japan, 2020.

[53] L. Barbaca, J.A. Venning, P.S. Russel, E.S.C Russel, P.W. Pearce, and P.A. Brandner. Dynamics of cavitation inception in high reynolds number shear flow. In *Proceedings of the 33rd Symposium on Naval Hydrodyanmics*, 2020.

[54] E.S.C Allan, L. Barbaca, J.A. Venning, P.S. Russel, P.W. Pearce, and P.A. Brandner. Nucleation and cavitation inception in high reynolds number shear layers. *Physics of Fluids*, 35:013317, 2023.

[55] E. P. Rood. Review – mechanisms of cavitation inception. *Journal of Fluids Engineering*, 113(2):163–175, 1991.

[56] R. E. A. Arndt, V. H. Arakeri, and H. Higuchi. Some observations of tip–vortex cavitation. *Journal of Fluid Mechanics*, 229:269–289, 1991.

[57] M. T. Khoo, J. A. Venning, B. W. Pearce, and P. A. Brandner. Statistical aspects of tip vortex cavitation inception and desinence in a nuclei deplete flow. *Experiments in Fluids*, 61(145), 2020.

[58] R. E. A. Arndt and A. P. Keller. Water quality effects on cavitation inception in a trailing vortex. *Journal of Fluids Engineering*, 114:438–430, 1992.

[59] B. Gindroz and M. L. Billet. Influence of the nuclei on the cavitation inception for different types of cavitation on ship propellers. *Journal of Fluids Engineering*, 120:171–178, 1998.

[60] F. B. Peterson. Hydrodynamic cavitation and some considerations of the influence of free gas content. In *Proceedings of the 9th Symposium on Naval Hydrodynamics*, Paris, France, 1972.

[61] J. Katz. Cavitation phenomena within regions of flow separation. *Journal of Fluid Mechanics*, 140:397–436, 1984.

[62] F. Salvatore, H. Streckwall, and T. van Terwisga. Propeller cavitation modelling by CFD-results from the VIRTUE 2008 Rome workshop. In *Proceedings of the First International Symposium on Marine Propulsors*, 2009.

[63] R. Bensow. Simulation of the unsteady cavitation on the the Delft Twist11 foil using RANS, DES and LES. In *Proceedings of the Second International Symposium on Marine Propulsors*, 2011.

[64] N. X. Lu, U. Svennberg, G. Bark, and R. Bensow. Numerical simulations of the cavitating flow on a marine propeller. In *Proceedings of the 8th International Symposium on Cavitation (CAV2012)*, 2012.

[65] M. Bappy, J. E. Martin, J. Li, G. C. Buscaglia, and P. M. Carrica. A stochastic approach to cavitation inception prediction. In *Proceedings of the Sixth International Symposium on Marine Propulsors*, 2019.

[66] D. W. Moore. A numerical study of the roll–up of a finite vortex sheet. *Journal of Fluid Mechanics*, 63(02):225–235, 1974.

[67] B. W. McCormick Jr. On cavitation produced by a vortex trailing from a lifting surface. *Journal of Basic Engineering*, pages 369–379, 1962.

[68] D. H. Fruman, P. Cerrutti, T. Pichon, and P. Dupont. Effect of hydrofoil planform on tip vortex roll–up and cavitation. *Journal of Fluid Engineering*, 117(1):162–169, 1995.

[69] T. Pichon, A. Pauchet, A. Astolfi, D. H. Fruman, and J. Y Billard. Effect of tripping laminar–to–turbulent boundary layer transition on tip vortex cavitation. *Journal of Ship Research*, 41(1):1–9, 1997.

[70] O. Boulon, M. Callenaere, J.-P. Franc, and J.-M. Michel. An experimental insight into the effect of confinement on tip vortex cavitation of an elliptical hydrofoil. *Journal of Fluid Mechanics*, 390:1–23, 1999.

[71] J. A. Astolfi, D. H. Fruman, and J. Y. Billard. A model for tip vortex roll–up in the near field region of three–dimensional foils and the prediction of cavitation onset. *European Journal of Mechanics-B/Fluids*, 18(4):757–775, 1999.

[72] A. Amini, J. Seo, S. H. Rhee, and M. Farhat. Mitigating tip vortex cavitation by a flexible trailing thread. *Physics of Fluids*, 31(12):127103, 2019.

[73] A. Asnaghi, U. Svennberg, and R. E. Bensow. Large eddy simulations of cavitating tip vortex flows. *Ocean Engineering*, 195:106703, 2020.

[74] C. Xie, J. Liu, J. W. Jiang, and W. X. Huang. Numerical study on wetted and cavitating tip–vortical flows around an elliptical hydrofoil: Interplay of cavitation, vortices, and turbulence. *Physics of Fluids*, 33(9):093316, 2021.

[75] S. Shin, J.W. Hong, D. Nagarathinam, B. K. Ahn, and S. G. Park. Tip vortex cavitation and induced noise characteristics of hydrofoils. *Applied Sciences*, 11(13): 5906, 2021.

[76] K. Mahesh, P. Kumar, A. Gnanaskandan, and Z. Nitzkorski. LES applied to ship research. *Journal of Ship Research*, 59(4):238–245, 2015.

[77] D. You, M. Wang, P. Moin, and R. Mittal. Effects of tip–gap size on the tip–leakage flow in a turbomachinery cascade. *Physics of Fluids*, 18(10):105102, 2006.

[78] K. Mahesh, G. Constantinescu, and P. Moin. A numerical method for large–eddy simulation in complex geometries. *Journal of Computational Physics*, 197(1):215–240, 2004.

[79] P. Kumar and K. Mahesh. Large–eddy simulation of flow over an axisymmetric body of revolution. *Journal of Fluid Mechanics*, 853:537–563, 2018.

[80] A. Verma, H. Jang, and K. Mahesh. The effect of an upstream hull on a propeller in reverse rotation. *Journal of Fluid Mechanics*, 704:61–88, 2012.

[81] H. Jang and K. Mahesh. Large eddy simulation of flow around a reverse rotating propeller. *Journal of Fluid Mechanics*, 729:151–179, 2013.

[82] H. Jang, A. Verma, and K. Mahesh. Predicting unsteady loads in marine propulsor crashback using large eddy simulation. *International Journal of Rotating Machinery*, 2012, 2012.

[83] P. Kumar and K. Mahesh. Large eddy simulation of propeller wake instabilities. *Journal of Fluid Mechanics*, 814:361–396, 2017.

[84] L. Chen, L. Zhang, X. Peng, and X. Shao. Influence of water quality on the tip vortex cavitation inception. *Physics of Fluids*, 31(2):023303, 2019.

[85] H. Cheng, X. Long, B. Ji, X. Peng, and M. Farhat. A new euler–lagrangian cavitation model for tip–vortex cavitation with the effect of non–condensable gas. *International Journal of Multiphase Flow*, 134:103441, 2021.

[86] R. Kunz, F. Boger, D. R. Stinebring, T. S. Chyczewski, J. W. Lindau, H. J. Gibeling, S. Venkateswaran, and T. R. Govindan. A preconditioned navier–stokes method for two–phase flows with application to cavitation. *Computers and Fluids*, 29(8):849–875, 2000.

[87] N.X. Lu, G. Bark, and R. Bensow. Introducing non–condensable gas in unsteady sheet cavitation modelling. In *Proceeding of the 15th Numerical Towing Tank Symposium*, 2012.

[88] M. G. Mithun, P. Koukouvinis, and M. Gavaises. Numerical simulation of cavitation and atomization using a fully compressible three–phase model. *Physical Review Fluids*, 3 (6):064304, 2018.

[89] F. M. White. *Viscous fluid flow*. McGraw-Hill New York, 2006.

[90] D. R. H. Beattie and P. B. Whalley. Simple two–phase fractional pressure drop calculation method. *International Journal of Multiphase Flow*, 8:83–87, 1982.

[91] J. L. Chen, B. Xue, K. Mahesh, and J. I. Siepmann. Molecular simulations probing the thermophysical properties of homogeneously stretched and bubbly water systems. *Journal of Chemical & Engineering Data*, 2019.

[92] R. S. Lagumbay. *Modeling and Simulation of Multiphase/Multicomponent Flows*. PhD thesis, University of Colorado, 2006.

[93] S. W. Kieffer. Sound speed in liquid–gas mixtures: Water–air and water–steam. *Journal of Geophysical Research*, 82:2895–2904, 1977.

[94] H. B. Karplus. Velocity of sound in a liquid containing gas bubbles. *The Journal of Acoustical Society of America*, 29:12–61, 1957.

[95] N. Park and K. Mahesh. Numerical and modeling issues in LES of compressible turbulence on unstructured grids. In *Proceedings of the 45th AIAA Aerospace Sciences Meeting and Exhibit, AIAA Paper*, number 0722, pages 1–18, 2007.

[96] H. C. Yee, N. D. Sandham, and M. J. Djomehri. Low–dissipative high–order shock–capturing methods using characteristic–based filters. *Journal of Computational Physics*, 150(1):199–238, 1999.

[97] F. Ducros, V. Ferrand, F. Nicoud, C. Weber, D. Darracq, C. Gacherieu, and T. Poinsot. Large–eddy simulation of the shock/turbulence interaction. *Journal of Computational Physics*, 152(2):517–549, 1999.

[98] R. Saurel and O. Lemetayer. A multiphase model for compressible flows with interfaces, shocks, detonation waves and cavitation. *Journal of Fluid Mechanics*, 431(6):239–271, 2001.

[99] D. Chargy, R. Abgrall, L. F. Fezoui, and B. Larrouturou. Comparisons of several upwind schemes for multi–component one–dimensional inviscid flows. Technical report, INRIA, 1990.

[100] B. Larrouturou. How to preserve the mass fractions positivity when computing compressible multi–component flows. *Journal of Computational Physics*, 95(1): 59–84, 1991.

[101] S. Karni. Multicomponent flow calculations by a consistent primitive algorithm. *Journal of Computational Physics*, 112(1):31–43, 1994.

[102] M. Germano, U. Piomelli, P. Moin, and W. H. Cabot. A dynamic subgrid–scale eddy viscosity model. *Physics of Fluids A*, 3(7):1760–1765, 1991.

[103] P. Moin, K. Squires, W. Cabot, and S. Lee. A dynamic subgrid–scale model for compressible turbulence and scalar transport. *Physics of Fluids A*, 3(11):2746–2757, 1991.

[104] S. Muppidi and K. Mahesh. Direct numerical simulation of passive scalar transport in transverse jets. *Journal of Fluid Mechanics*, 598:335–360, 2008.

[105] B. Merci, J. Steelant, J. Vierendeels, K. Riemslagh, and E. Dick. Computational treatment of source terms in two–equation turbulence models. *AIAA journal*, 38(11):2085–2093, 2000.

[106] C. Lian, G. Xia, and C. L. Merkle. Impact of source terms on reliability of CFD algorithms. *Computers & Fluids*, 39:1909–1922, 2010.

[107] S. V. Patankar. *Numerical Heat Transfer and Fluid Flow*. Taylor & Francis, 1st edition, 1980.

[108] H. Jiang and L. Cheng. Transition to the secondary vortex street in the wake of a circular cylinder. *Journal of Fluid Mechanics*, 867:691–722, 2019.

[109] W. W. Durgin and S. K. F. Karlsson. On the phenomenon of vortex street breakdown. *Journal of Fluid Mechanics*, 48:507–527, 1971.

[110] T. Karasudani and M. Funakoshi. Evolution of a vortex street in the far wake of a cylinder. *Fluid Dynamics Research*, 14:331–352, 1994.

[111] H. Ganesh, L. Deijlen, A. Bhatt, J. Wu, and S. L. Ceccio. Cavitation dynamics in wakes of bluff bodies. In *Proceedings of the 32nd Symposium on Naval Hydrodyanmics*, 2018.

[112] J. Varga and G. Sebestiyen. Experimental investigation of some properties of cavitating flow. *Periodica Polytechnica Mechanical Engineering*, 9(3):243–254, 1965.

[113] J. O. Young and J. W. Holl. Effects of cavitation on periodic wakes behind symmetric wedges. *Journal of Basic Engineering*, pages 163–176, 1966.

[114] S. Anantharamu and K. Mahesh. A parallel and streaming dynamic mode decomposition algorithm with finite precision error analysis for large data. *Journal of Computational Physics*, 380:355–377, 2019.

[115] V. H. Arakeri. Viscous effects on the position of cavitation separation from smooth bodies. *Journal of Fluid Mechanics*, 68:779–799, 1975.

[116] E. F. Toro. *Riemann Solvers and Numerical Methods for Fluid Dynamics*. Springer, 1999.

[117] T. S. Lund, X. Wu, and K. D. Squires. Generation of turbulent inflow data for spatially-developing boundary layer simulations. *Journal of Computational Physics*, 140(2):233–258, 1998.

[118] P. Kumar and K. Mahesh. Towards large eddy simulation of hull–attached propeller in crashback. In *Proceedings of the 31st Symposium on Naval Hydrodynamics*, California, USA, 2016.

[119] P. Schlatter and R. Örlü. Assessment of direct numerical simulation data of turbulent boundary layers. *Journal of Fluid Mechanics*, 659:116–126, 2010.

[120] G. Eitel-Amor, R. rl, and P. Schlatter. Simulation and validation of a spatially evolving turbulent boundary layer up to $Re_\theta = 8300$. *International Journal of Heat and Fluid Flow*, 47:57–69, 2014.

[121] I. Lee and H. J. Sung. Characteristics of wall pressure fluctuations in separated and reattaching flows over a backward–facing step. *Experiments in Fluids*, 30: 262–272, 2001.

[122] M. S. Chong, A. E. Perry, and B. J. Cantwell. A general classification of three-dimensional flow fields. *Physics of Fluids A: Fluid Dynamics*, 2(5):765–777, 1990.

[123] B. J. Cantwell. Exact solution of a restricted euler equation for the velocity gradient tensor. *Physics of Fluids A: Fluid Dynamics*, 4(4):782–793, 1992.

[124] A. E. Perry and M. S. Chong. Topology of flow patterns in vortex motions and turbulence. *Applied Scientific Research*, 53:357–374, 1994.

[125] A. Ooi, J. Martin, J. Soria, and M.S. Chong. A study of the evolution and characteristics of the invariants of the velocity–gradient tensor in isotropic turbulence. *Journal of Fluid Mechanics*, 381:141–174, 1999.

[126] C.B. da Silva and C.F. Pereira. Invariants of the velocity–gradient, rate–of–strain and rate–of–rotation tensors across the turbulent/nonturbulent interface in jets. *Physics of Fluids*, 20(5):055101, 2008.

[127] C. Truesdell. *The Kinematics of Vorticity*. Indiana University Press, 1st edition, 1954.

[128] E. Gavi, L. Rivautella, D.L. Marchisio, M. Vanni, A.A. Barresi, and G. Baldi. CFD modelling of nano-particle precipitation in confined impinging jet reactors. *Chemical Engineering Research and Design*, 85(5):735–744, 2007.

[129] M. Petitti, A. Nasuti, D. L. Marchisio, M. Vanni, G. Baldi, N. Mancini, and F. Podenzani. Bubble size distribution modeling in stirred gasliquid reactors with QMOM augmented by a new correction algorithm. *AIChE Journal*, 56(1):36–53, 2010.

[130] P.M. Carrica, D. Drew, F. Bonetto, and R.T. Lahey Jr. A polydisperse model for bubbly two-phase flow around a surface ship. *International Journal of Multiphase Flow*, 25(2):257–305, 1999.

[131] A.M. Castro and P.M. Carrica. Bubble size distribution prediction for large-scale ship flows: Model evaluation and numerical issues. *International Journal of Multiphase Flow*, 57:131–150, 2013.

[132] J. Li and P.M. Carrica. A population balance cavitation model. *International Journal of Multiphase Flow*, 138:103617, 2021.

[133] S.H. Bryngelson, R.O. Fox, and T. Colonius. Conditional moment methods for polydisperse cavitating flows. *Journal of Computational Physics*, 477:111917, 2023.

[134] C. T. Hsiao and L. L. Pauley. Numerical study of the steady–state tip vortex flow over a finite–span hydrofoil. *Journal of Fluids Engineering, Transactions of the ASME*, 120(2):345–353, 1998.

[135] M. L. Billet and J. W. Holl. Scale effects on various types of limited cavitation. *Journal of Fluids Engineering*, 103(3):405–414, 1981.

[136] P. Kumar and K. Mahesh. Large eddy simulation of flow over a confined elliptic hydrofoil. In *Proceedings of the Sixth International Symposium on Marine Propulsors, Rome, Italy*, 2019.

[137] J. Jeong and F. Hussain. On the identification of a vortex. *Journal of Fluid Mechanics*, 285:69–94, 1995.

[138] G. K. Batchelor. Axial flow in trailing line vortices. *Journal of Fluid Mechanics*, 20(4):645–658, 1964.

[139] M. H. Bappy, P. M. Carrica, J. Li, E. Martin, A. Vela-Martin, L. S. Freire, and G. C. Buscaglia. A sub–grid scale cavitation inception model. *Physics of Fluids*, 34:033308, 2022.

[140] K. Park, H. Seol, W. Choi, and S. Lee. Numerical prediction of tip vortex cavitation behavior and noise considering nuclei size and distribution. *Applied Acoustics*, 70:674680, 2009.

[141] R. E. A. Arndt and B. H. Maines. Nucleation and bubble dynamics in vortical flows. *Journal of Fluids Engineering*, 122:488–493, 2000.

[142] M. T. Khoo, J. A. Venning, B. W. Pearce, and P. A. Brandner. Nucleation effects on tip vortex cavitation inception location. In *Proceeding of the 22nd Australasian Fluid Mechanics Conference (AFMC2020)*, 2020.

[143] I.J. Campbell and A. S. Pitcher. Shock waves in liquid containing gas bubbles. *Procedings of the Royal Society A*, 243, 1958.

[144] J. W. Holl, M. L. Billet, and D. S. Weir. Thermodynamic effects on developed cavitation. *Journal of Fluids Engineering*, 97(4), 1975.

Appendix A

Flux Jacobian and Eigenvectors

A.1 Flux Jacobian

The non-zero elements of the Jacobian matrix A_{ij} are listed below.

$A_{12} = \hat{n}_x$

$A_{13} = \hat{n}_y$

$A_{14} = \hat{n}_z$

$A_{21} = (\gamma^* - 1)e_k^* \hat{n}_x - uV_N$

$A_{22} = V_N - (\gamma^* - 2)u\hat{n}_x$

$A_{23} = u\hat{n}_y - (\gamma^* - 1)v\hat{n}_x$

$A_{24} = u\hat{n}_z - (\gamma^* - 1)w\hat{n}_x$

$A_{25} = (\gamma^* - 1)\hat{n}_x$

$A_{26} = (\gamma^* - 1)e_1^* \hat{n}_x$

$A_{27} = (\gamma^* - 1)e_2^* \hat{n}_x$

$A_{31} = (\gamma^* - 1)e_k^* \hat{n}_y - vV_N$

$A_{32} = v\hat{n}_x - (\gamma^* - 1)u\hat{n}_y$

$A_{33} = V_N - (\gamma^* - 2)v\hat{n}_y$

$A_{34} = v\hat{n}_z - (\gamma^* - 1)w\hat{n}_y$

$A_{35} = (\gamma^* - 1)\hat{n}_y$

$A_{36} = (\gamma^* - 1)e_1^* \hat{n}_y$

$$A_{37} = (\gamma^* - 1)e_2^*\hat{n}_y$$
$$A_{41} = (\gamma^* - 1)e_k^*\hat{n}_z - wV_N$$
$$A_{42} = w\hat{n}_x - (\gamma^* - 1)u\hat{n}_z$$
$$A_{43} = w\hat{n}_y - (\gamma^* - 1)v\hat{n}_z$$
$$A_{44} = V_N - (\gamma^* - 2)w\hat{n}_z$$
$$A_{45} = (\gamma^* - 1)\hat{n}_z$$
$$A_{46} = (\gamma^* - 1)e_1^*\hat{n}_z$$
$$A_{47} = (\gamma^* - 1)e_2^*\hat{n}_z$$
$$A_{51} = [(\gamma^* - 1)e_k^* - h_t]V_N$$
$$A_{52} = h_t\hat{n}_x - (\gamma^* - 1)uV_N$$
$$A_{53} = h_t\hat{n}_y - (\gamma^* - 1)vV_N$$
$$A_{54} = h_t\hat{n}_z - (\gamma^* - 1)wV_N$$
$$A_{55} = \gamma^* V_N$$
$$A_{56} = (\gamma^* - 1)e_1^* V_N$$
$$A_{57} = (\gamma^* - 1)e_2^* V_N$$
$$A_{61} = -Y_v V_N$$
$$A_{62} = Y_v\hat{n}_x$$
$$A_{63} = Y_v\hat{n}_y$$
$$A_{64} = Y_v\hat{n}_z$$
$$A_{66} = V_N$$
$$A_{71} = -Y_g V_N$$
$$A_{72} = Y_g\hat{n}_x$$
$$A_{73} = Y_g\hat{n}_y$$
$$A_{74} = Y_g\hat{n}_z$$
$$A_{77} = V_N$$

where

$$\gamma^* = 1 + \frac{\rho(1-Y_v-Y_g)K_l p + \rho(Y_v R_v + Y_g R_g)(p+P_c)}{den1 - den2},$$

$$den1 = 2p\rho C_{vm} + \rho P_c((1-Y_v-Y_g)C_{pl} + Y_v C_{vv} + Y_g C_{vg}),$$

$$den2 = \rho e_s(\rho(1-Y_v-Y_g)K_l + \rho Y_v R_v + \rho Y_g R_g),$$

$$e_k^* = \frac{1}{2}u_i u_i + \frac{p\rho e_s K_l - p^2 C_{vl} - pP_c C_{pl}}{p\rho(1-Y_v-Y_g)K_l + \rho(Y_v R_v + Y_g R_g)(p+P_c)},$$

$$e_1^* = \frac{\rho e_s R_v(p+P_c) - pC_{vv}(p+P_c) - p\rho e_s K_l - p^2 C_{vl} - pP_c C_{pl}}{p\rho(1-Y_v-Y_g)K_l + \rho(Y_v R_v + Y_g R_g)(p+P_c)},$$

$$e_2^* = \frac{\rho e_s R_g(p+P_c) - pC_{vg}(p+P_c) - p\rho e_s K_l - p^2 C_{vl} - pP_c C_{pl}}{p\rho(1-Y_v-Y_g)K_l + \rho(Y_v R_v + Y_g R_g)(p+P_c)}$$

$$h_t = \frac{E_T}{\rho} + \frac{p}{\rho}$$

A.2 Eigenvectors

$$R_{ij} = \begin{pmatrix} 1 & 1 & 1 & 0 & 0 & 0 & 0 \\ u - a\hat{n}_x & u & u + a\hat{n}_x & \hat{n}_y & -\hat{n}_z & 0 & 0 \\ v - a\hat{n}_y & v & v + a\hat{n}_y & -\hat{n}_x & 0 & \hat{n}_z & -\hat{n}_z \\ w - a\hat{n}_z & w & w + a\hat{n}_z & 0 & \hat{n}_x & -\hat{n}_y & \hat{n}_y \\ h_t - aV_N & e_k & h_t + aV_N & u\hat{n}_y - v\hat{n}_x & w\hat{n}_x - u\hat{n}_z & v\hat{n}_z - w\hat{n}_y - e_1^* & -v\hat{n}_z + w\hat{n}_y - e_2^* \\ Y_v & Y_v & Y_v & 0 & 0 & 1 & 0 \\ Y_g & Y_g & Y_g & 0 & 0 & 0 & 1 \end{pmatrix}$$

$$R_{ij}^{-1} = \begin{pmatrix} \frac{aV_N + (\gamma^*-1)e_k^*}{2a^2} & \frac{-a\hat{n}_x - (\gamma^*-1)u}{2a^2} & \frac{-a\hat{n}_y - (\gamma^*-1)v}{2a^2} & \frac{-a\hat{n}_z - (\gamma^*-1)w}{2a^2} & \frac{\gamma-1}{2a^2} & \frac{(\gamma-1)e_1^*}{2a^2} & \frac{(\gamma-1)e_2^*}{2a^2} \\ \frac{a^2 - (\gamma^*-1)e_k^*}{a^2} & \frac{(\gamma^*-1)u}{a^2} & \frac{(\gamma^*-1)v}{a^2} & \frac{(\gamma^*-1)w}{a^2} & \frac{1-\gamma}{a^2} & \frac{(1-\gamma)e_1^*}{a^2} & \frac{(1-\gamma)e_2^*}{a^2} \\ \frac{-aV_N + (\gamma^*-1)e_k^*}{2a^2} & \frac{a\hat{n}_x - (\gamma^*-1)u}{2a^2} & \frac{a\hat{n}_y - (\gamma^*-1)v}{2a^2} & \frac{a\hat{n}_z - (\gamma^*-1)w}{2a^2} & \frac{\gamma-1}{2a^2} & \frac{(\gamma-1)e_1^*}{2a^2} & \frac{(\gamma-1)e_2^*}{2a^2} \\ \frac{v - V_N\hat{n}_y + (Y_g - Y_v)\hat{n}_z}{\hat{n}_x} & \hat{n}_y & \frac{\hat{n}_y^2 - 1}{\hat{n}_x} & \frac{\hat{n}_y\hat{n}_z}{\hat{n}_x} & 0 & \frac{\hat{n}_z}{\hat{n}_x} & -\frac{\hat{n}_z}{\hat{n}_x} \\ \frac{V_N\hat{n}_z - w + (Y_g - Y_v)\hat{n}_y}{\hat{n}_x} & -\hat{n}_z & -\frac{\hat{n}_y\hat{n}_z}{\hat{n}_x} & \frac{1-\hat{n}_z^2}{\hat{n}_x} & 0 & \frac{\hat{n}_y}{\hat{n}_x} & -\frac{\hat{n}_y}{\hat{n}_x} \\ -Y_v & 0 & 0 & 0 & 0 & 1 & 0 \\ -Y_g & 0 & 0 & 0 & 0 & 0 & 1 \end{pmatrix}$$

The above matrix becomes singular when $n_x = 0$. In order to avoid this, the above

matrix is used only when $n_x > n_y$ and $n_x > n_z$. In other cases the following matrices are used. If $n_y > n_x$ and $n_y > n_z$, then

$$R_{ij} = \begin{pmatrix} 1 & 1 & 1 & 0 & 0 & 0 & 0 \\ u - a\hat{n}_x & u & u + a\hat{n}_x & \hat{n}_y & -\hat{n}_z & 0 & 0 \\ v - a\hat{n}_y & v & v + a\hat{n}_y & -\hat{n}_x & 0 & \hat{n}_z & -\hat{n}_z \\ w - a\hat{n}_z & w & w + a\hat{n}_z & 0 & \hat{n}_x & -\hat{n}_y & \hat{n}_y \\ h_t - aV_N & e_k & h_t + aV_N & u\hat{n}_y - v\hat{n}_x & w\hat{n}_x - u\hat{n}_z - e_1^* & v\hat{n}_z - w\hat{n}_y & -v\hat{n}_z + w\hat{n}_y - e_2^* \\ Y_v & Y_v & Y_v & 0 & 1 & 0 & 0 \\ Y_g & Y_g & Y_g & 0 & 0 & 0 & 1 \end{pmatrix}$$

$$R_{ij}^{-1} = \begin{pmatrix} \frac{aV_N + (\gamma^* - 1)e_k^*}{2a^2} & \frac{-a\hat{n}_x - (\gamma^* - 1)u}{2a^2} & \frac{-a\hat{n}_y - (\gamma^* - 1)v}{2a^2} & \frac{-a\hat{n}_z - (\gamma^* - 1)w}{2a^2} & \frac{\gamma - 1}{2a^2} & \frac{(\gamma - 1)e_1^*}{2a^2} & \frac{(\gamma - 1)e_2^*}{2a^2} \\ \frac{a^2 - (\gamma^* - 1)e_k^*}{a^2} & \frac{(\gamma^* - 1)u}{a^2} & \frac{(\gamma^* - 1)v}{a^2} & \frac{(\gamma^* - 1)w}{a^2} & \frac{1 - \gamma}{a^2} & \frac{(1 - \gamma)e_1^*}{a^2} & \frac{(1 - \gamma)e_2^*}{a^2} \\ \frac{-aV_N + (\gamma^* - 1)e_k^*}{2a^2} & \frac{a\hat{n}_x - (\gamma^* - 1)u}{2a^2} & \frac{a\hat{n}_y - (\gamma^* - 1)v}{2a^2} & \frac{a\hat{n}_z - (\gamma^* - 1)w}{2a^2} & \frac{\gamma - 1}{2a^2} & \frac{(\gamma - 1)e_1^*}{2a^2} & \frac{(\gamma - 1)e_2^*}{2a^2} \\ \frac{-u + V_N\hat{n}_x - Y_v\hat{n}_z}{\hat{n}_y} & \frac{1 - \hat{n}_x^2}{\hat{n}_y} & -\hat{n}_x & -\frac{\hat{n}_x\hat{n}_z}{\hat{n}_y} & 0 & \frac{\hat{n}_z}{\hat{n}_y} & 0 \\ -Y_v & 0 & 0 & 0 & 1 & 0 & \\ \frac{-V_N\hat{n}_z + w - Y_g\hat{n}_y - Y_v\hat{n}_x}{\hat{n}_y} & \frac{\hat{n}_x\hat{n}_z}{\hat{n}_y} & \hat{n}_z & -\frac{1 - \hat{n}_z^2}{\hat{n}_y} & 0 & \frac{\hat{n}_x}{\hat{n}_y} & 1 \\ -Y_g & 0 & 0 & 0 & 0 & 0 & 1 \end{pmatrix}$$

If $n_z > n_x$ and $n_z > n_y$, then

$$R_{ij} = \begin{pmatrix} 1 & 1 & 1 & 0 & 0 & 0 & 0 \\ u - a\hat{n}_x & u & u + a\hat{n}_x & \hat{n}_y & -\hat{n}_z & 0 & 0 \\ v - a\hat{n}_y & v & v + a\hat{n}_y & -\hat{n}_x & 0 & \hat{n}_z & -\hat{n}_z \\ w - a\hat{n}_z & w & w + a\hat{n}_z & 0 & \hat{n}_x & -\hat{n}_y & \hat{n}_y \\ h_t - aV_N & e_k & h_t + aV_N & u\hat{n}_y - v\hat{n}_x - e_1^* & w\hat{n}_x - u\hat{n}_z & v\hat{n}_z - w\hat{n}_y & -v\hat{n}_z + w\hat{n}_y - e_2^* \\ Y_v & Y_v & Y_v & 1 & 0 & 0 & 0 \\ Y_g & Y_g & Y_g & 0 & 0 & 0 & 1 \end{pmatrix}$$

$$R_{ij}^{-1} = \begin{pmatrix} \frac{aV_N + (\gamma^* - 1)e_k^*}{2a^2} & \frac{-a\hat{n}_x - (\gamma^* - 1)u}{2a^2} & \frac{-a\hat{n}_y - (\gamma^* - 1)v}{2a^2} & \frac{-a\hat{n}_z - (\gamma^* - 1)w}{2a^2} & \frac{\gamma - 1}{2a^2} & \frac{(\gamma - 1)e_1^*}{2a^2} & \frac{(\gamma - 1)e_2^*}{2a^2} \\ \frac{a^2 - (\gamma^* - 1)e_k^*}{a^2} & \frac{(\gamma^* - 1)u}{a^2} & \frac{(\gamma^* - 1)v}{a^2} & \frac{(\gamma^* - 1)w}{a^2} & \frac{1 - \gamma}{a^2} & \frac{(1 - \gamma)e_1^*}{a^2} & \frac{(1 - \gamma)e_2^*}{a^2} \\ \frac{-aV_N + (\gamma^* - 1)e_k^*}{2a^2} & \frac{a\hat{n}_x - (\gamma^* - 1)u}{2a^2} & \frac{a\hat{n}_y - (\gamma^* - 1)v}{2a^2} & \frac{a\hat{n}_z - (\gamma^* - 1)w}{2a^2} & \frac{\gamma - 1}{2a^2} & \frac{(\gamma - 1)e_1^*}{2a^2} & \frac{(\gamma - 1)e_2^*}{2a^2} \\ -Y_v & 0 & 0 & 0 & 1 & 0 & \\ \frac{u - V_N\hat{n}_x - Y_v\hat{n}_y}{\hat{n}_z} & -\frac{1 - \hat{n}_x^2}{\hat{n}_z} & \frac{\hat{n}_x\hat{n}_y}{\hat{n}_z} & \hat{n}_x & 0 & \frac{\hat{n}_y}{\hat{n}_z} & 0 \\ \frac{V_N\hat{n}_y - v - Y_g\hat{n}_z - Y_v\hat{n}_x}{\hat{n}_z} & -\frac{\hat{n}_x\hat{n}_y}{\hat{n}_z} & \frac{1 - hatn_y^2}{\hat{n}_z} & -\hat{n}_y & 0 & \frac{\hat{n}_x}{\hat{n}_z} & 1 \\ -Y_g & 0 & 0 & 0 & 0 & 0 & 1 \end{pmatrix}$$

Appendix B

Analysis of condensation shock using Rankine–Hugoniot jump conditions

Analysis of shock waves in bubbly flows of liquid–gas mixture was considered by Campbell and Pitcher [143], who related shock propagation speed to the pressure in the high–pressure side of the shock, the density of the liquid, and relative proportions of gas and liquid. They also showed negligible temperature rise across steady condensation shock waves. Here, we consider the current system of homogeneous mixture with both vapor and gas mass transport closed with the mixture equation of state and consider a left–moving shock (moving upstream of the flow direction) in a frame of reference moving with the shock as described in figure B.1. The velocities in the moving reference frame are

$$\hat{u}_L = u_L - S \quad \text{and} \quad \hat{u}_R = u_R - S. \tag{B.1}$$

Here, S is the shock speed. "ˆ" is used to indicate quantities in moving reference frame. "L" and "R" subscripts are used respectively for the quantities at the left and at the right of the shock. Since we are considering a left–moving shock, left and right sides of the shock become ahead and behind the shock respectively.

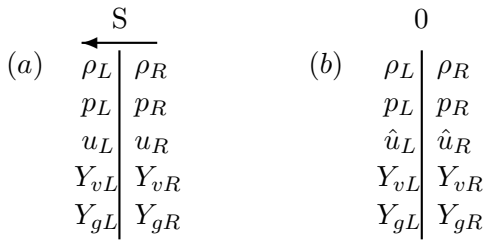

Figure B.1: Left moving shock in a stationary frame of reference (a) and in a frame of reference moving with the shock (b).

The Rankine–Hugoniot jump conditions in a frame of reference moving with the shock are:

$$\rho_R \hat{u}_R = \rho_L \hat{u}_L, \tag{B.2}$$

$$\rho_R \hat{u}_R^2 + p_R = \rho_L \hat{u}_L^2 + p_L, \tag{B.3}$$

$$\rho_R \hat{u}_R (e_R + p_R/\rho_R + \hat{u}_R^2/2) = \rho_L \hat{u}_L (e_L + p_L/\rho_L + \hat{u}_L^2/2), \tag{B.4}$$

$$\rho_R Y v_R \hat{u}_R = \rho_L Y v_L \hat{u}_L \quad \text{and} \tag{B.5}$$

$$\rho_R Y g_R \hat{u}_R = \rho_L Y g_L \hat{u}_L. \tag{B.6}$$

Here, subscripts v and g in equations (B.5) and (B.6) denote vapor and NCG respectively. Note that phase change between vapor and water is not explicitly modeled, however, its effects are implicitly calculated since vapor mass fraction will have different values across the shock.

Applying equation (B.2) to equations (B.3) and (B.4) we have

$$\hat{u}_R^2 = \frac{\rho_L}{\rho_R} \frac{(p_R - p_L)}{(\rho_R - \rho_L)}, \tag{B.7}$$

$$\hat{u}_L^2 = \frac{\rho_R}{\rho_L}\frac{(p_R - p_L)}{(\rho_R - \rho_L)} \quad \text{and} \tag{B.8}$$

$$e_R + p_R/\rho_R + \hat{u}_R^2/2 = e_L + p_L/\rho_L + \hat{u}_L^2/2. \tag{B.9}$$

Substituting equation (B.7) and (B.8) into equation (B.9) we have an equation for the energy difference across the shock,

$$e_R - e_L = \frac{1}{2}\frac{(p_R + p_L)(\rho_R - \rho_L)}{\rho_R \rho_L}. \tag{B.10}$$

From equations (2.5) and (2.4), the mixture internal energy can be written as

$$e = \frac{C_{vm}p^2 + [C_{vm} + (1 - Y_v - Y_g)K_l]P_c p}{[\rho(Y_v R_v + Y_g R_g)(p + P_c) + \rho(1 - Y_v - Y_g)K_l p]}, \tag{B.11}$$

and can be simplified as

$$e = \frac{p}{\rho(\overline{\gamma} - 1)}, \quad \text{where} \tag{B.12}$$

$$\frac{1}{\overline{\gamma} - 1} = \frac{C_{vm}p + [C_{vm} + (1 - Y_v - Y_g)K_l]P_c}{[(Y_v R_v + Y_g R_g)(p + P_c) + (1 - Y_v - Y_g)K_l p]}. \tag{B.13}$$

Using equation (B.12) in equation (B.10) followed by algebraic simplification we obtain an equation for the density ratio across the shock as

$$\frac{\rho_R}{\rho_L} = \frac{\frac{p_R}{p_L}\frac{\overline{\gamma}_R + 1}{\overline{\gamma}_R - 1} + 1}{\frac{p_R}{p_L} + \frac{\overline{\gamma}_L + 1}{\overline{\gamma}_L - 1}}. \tag{B.14}$$

With equations (B.1), (B.2), (B.8) and (B.14) an equation for the shock speed can be derived:

$$S = u_L - \sqrt{\frac{(p_R - p_L)[\frac{p_R}{p_L}\frac{\overline{\gamma}_R + 1}{\overline{\gamma}_R - 1} + 1]}{(\rho_R - \rho_L)[\frac{p_R}{p_L} + \frac{\overline{\gamma}_L + 1}{\overline{\gamma}_L - 1}]}}. \tag{B.15}$$

Note that in the single–phase limit with $Y_g = 1$, $Y_v = 0$ and $1 - Y_v - Y_g = 0$, equation (B.15) simplifies into the classical gasdynamics equation [116].

Appendix C

Temperature jump relation across condensation shock

Is is known that temperature variations in hydrodynamic cavitation are mostly negligible due to the high specific heat capacity of liquid. However, temperature variations are observed to increase in developed cavitation involving mass transfer in large cavities [144]. Therefore, the propagation of a condensation shock might be expected to lead to larger temperature fluctuations. Here, we use results from the simulations of chapter 3 at $Re = 200$ and $\sigma = 0.7$ along with an equation for the temperature ratio across the condensation shock, to show that temperature variation in this process is also negligible.

Temperature ratio across the condensation shock can be derived from the density relation given by equation (B.14) and the mixture equation of state (equation (2.5)). It is given by

$$\begin{aligned} \frac{T_L}{T_R} &= \frac{[\frac{2b_R}{a_R} + 1 + \frac{p_L}{p_r}](p_L + P_c)a_R}{[\frac{p_R}{p_L} + \frac{2b_L}{a_L} + 1](p_R + P_c)a_L}, \quad \text{where} \\ a &= (Y_v R_v + Y_g R_g)(p + P_c) + (1 - Y_v - Y_g)K_l p \quad \text{and} \\ b &= C_{vm} p + [C_{vm} + (1 - Y_v - Y_g)K_l]P_c. \end{aligned} \tag{C.1}$$

Note from equation (C.1) that considering different values of vapor and gas mass fraction for left and right implies that, although the temperature jump is of comparable

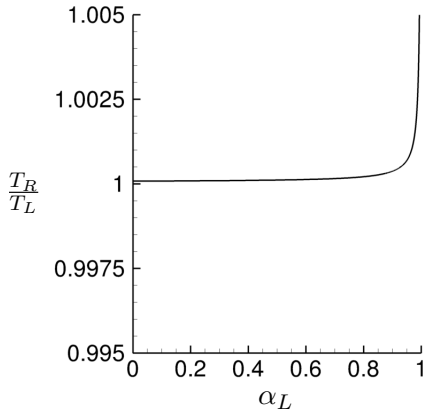

Figure C.1: Temperature ratio across a condensation shock for different amounts of gaseous phase ahead of shock.

magnitude to pressure ratio when having completely gaseous phases on both sides, the ratio is nearly unity in the presence of liquid. We investigate this by considering a scenario where shock is moving from water to a mixture of water–vapor–gas with increasing amount of gaseous phase void fraction. Pressure in the liquid is considered 1 atm and pressure inside the mixture is chosen to be vapor pressure. This mimics the scenario of condensation shock propagating through the cavity. Temperature jump obtained from the equation (C.1) for increasing amount of gaseous phase void fraction is plotted in figure C.1. The figure shows that temperature ratio for any amount of gaseous void fraction ahead of the shock is negligible. The maximum ratio in the plot is $T_R/T_L = 1.005$ for $\alpha_L = 0.994$ (which is much higher than the maximum void fractions reached in practical applications). The same conclusions would hold even in the presence of some amount of gaseous void fraction mixed with the liquid behind the shock (not shown here).

The isothermal behavior of the condensation shock is confirmed in our simulations. Here, we obtain the temperature jump across the condensation shock observed for $\sigma = 0.7$ at time instances mentioned in figure 3.16. Figure C.2 shows the temperature ratio both in presence and absence of gas. It is evident that the condensation shock in the current calculation is nearly isothermal.

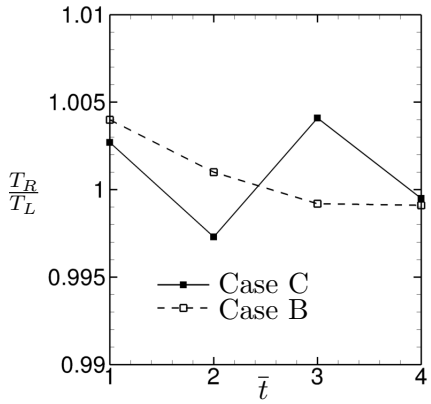

Figure C.2: Temperature ratio across a condensation shock for $\sigma = 0.7$.